National Library of Canada

Bibliothèque nationale du Canada

Canadian Theses Service

Services des thèses canadiennes

Ottawa, Canada
K1A 0N4

CANADIAN THESES

THÈSES CANADIENNES

NOTICE

The quality of this microfiche is heavily dependent upon the quality of the original thesis submitted for microfilming. Every effort has been made to ensure the highest quality of reproduction possible.

If pages are missing, contact the university which granted the degree.

Some pages may have indistinct print especially if the original pages were typed with a poor typewriter ribbon or if the university sent us an inferior photocopy.

Previously copyrighted materials (journal articles, published tests, etc.) are not filmed.

Reproduction in full or in part of this film is governed by the Canadian Copyright Act, R.S.C. 1970, c. C-30.

AVIS

La qualité de cette microfiche dépend grandement de la qualité de la thèse soumise au microfilmage. Nous avons tout fait pour assurer une qualité supérieure de reproduction.

S'il manque des pages, veuillez communiquer avec l'université qui a conféré le grade.

La qualité d'impression de certaines pages peut laisser à désirer, surtout si les pages originales ont été dactylographiées à l'aide d'un ruban usé ou si l'université nous a fait parvenir une photocopie de qualité inférieure.

Les documents qui font déjà l'objet d'un droit d'auteur (articles de revue, examens publiés, etc.) ne sont pas microfilmés.

La reproduction, même partielle, de ce microfilm est soumise à la Loi canadienne sur le droit d'auteur, SRC 1970, c. C-30.

THIS DISSERTATION HAS BEEN MICROFILMED EXACTLY AS RECEIVED

LA THÈSE A ÉTÉ MICROFILMÉE TELLE QUE NOUS L'AVONS REÇUE

NL-339 (r.86/06)

Canada

TIME-RESOLVED PHOTOLUMINESCENCE STUDIES OF EXCITON PHENOMENA IN Si, CdSe, ZnSe AND GaAs ON A SUB-NANOSECOND TIME SCALE

by

Thomas W. Steiner

B.Sc. University of Waterloo 1981

THESIS SUBMITTED IN PARTIAL FULFILLMENT OF

THE REQUIREMENTS FOR THE DEGREE OF

DOCTOR OF PHILOSOPHY

in the Department

of

Physics

© Thomas W. Steiner 1986

SIMON FRASER UNIVERSITY

January 1986

All rights reserved. This work may not be
reproduced in whole or in part, by photocopy
or other means, without permission of the author

Permission has been granted to the National Library of Canada to microfilm this thesis and to lend or sell copies of the film.

The author (copyright owner) has reserved other publication rights, and neither the thesis nor extensive extracts from it may be printed or otherwise reproduced without his/her written permission.

L'autorisation a été accordée à la Bibliothèque nationale du Canada de microfilmer cette thèse et de prêter ou de vendre des exemplaires du film.

L'auteur (titulaire du droit d'auteur) se réserve les autres droits de publication; ni la thèse ni de longs extraits de celle-ci ne doivent être imprimés ou autrement reproduits sans son autorisation écrite.

ISBN 0-315-30755-2

APPROVAL

Name: Thomas W. Steiner

Degree: Ph.D. Physics

Title of Thesis: Time-Resolved Photoluminescence Studies of Exciton Phenomena in Si, CdSe, ZnSe and GaAs on a Sub-Nanosecond Time Scale

Examining Committee:

Chairman: Dr. R.H. Enns

Dr. M.L.W. Thewalt
Senior Supervisor

Dr. G. Kirczenow

Dr. R. Morrison

Dr. J.C. Irwin

Dr. P.Y. Yu
External Examiner
Dept. of Physics
UC Berkeley

Date Approved: January 24, 1986

PARTIAL COPYRIGHT LICENSE

I hereby grant to Simon Fraser University the right to lend my thesis, project or extended essay (the title of which is shown below) to users of the Simon Fraser University Library, and to make partial or single copies only for such users or in response to a request from the library of any other university, or other educational institution, on its own behalf or for one of its users. I further agree that permission for multiple copying of this work for scholarly purposes may be granted by me or the Dean of Graduate Studies. It is understood that copying or publication of this work for financial gain shall not be allowed without my written permission.

Title of Thesis/Project/Extended Essay

TIME-RESOLVED PHOTOLUMINESCENCE STUDIES OF

EXCITON PHENOMENA IN Si, CdSe, ZnSe AND GaAs ON A

SUB-NANOSECOND TIME SCALE

Author: [signature]

(signature)

TOM WALTER STEINER

(name)

30 Jan 86

(date)

ABSTRACT

The advent of synchronously pumped, modelocked, cavity dumped dye lasers and fast photomultipliers has allowed time-resolved photoluminescence spectroscopy to be pushed into the sub-nanosecond and picosecond regime. This enables the transient study of exciton phenomena in semiconductors whose interactions, particularly in direct gap materials, take place on this time scale. Time-resolved spectroscopy allows the direct measurement of transition oscillator strengths, a quantity which is sensitive to theoretical exciton models, thus allowing experimental tests of theory. Time-resolved photoluminescence is also useful for identifying third particle replicas of principle transitions thus enabling estimates of the exciton binding energies to be made. In Si, the lifetimes of the deepest simple acceptors In and Tl, as well as the deepest simple donor Bi, bound excitons were measured and in the case of the acceptors found to agree with predictions based on the simplest theory. In CdSe it was determined that bound excitons are formed from the trapping of free excitons, contrary to other published results, by observing the time domain behaviour of the free and bound exciton luminescence. Selective excitation of the bound exciton transition allowed identification of satellite lines and in the case of the acceptor, gave a binding energy substantially less than the common known acceptors. For ZnSe the lifetimes of bound excitons were

measured and the results compared with theoretical predictions. In the case of GaAs time-resolved photoluminescence allowed the testing of two models put forward to explain the 'damage lines' characteristic of sample growth by molecular beam epitaxy. Neither model was found to be consistent with experiment for the whole set of lines. Selective excitation of the highest energy 'damage' line showed it to be acceptor like although with a smaller binding energy than previously thought. These same samples also showed a time-dependent dip, under selected excitation conditions, in the polariton region of the spectrum. This behaviour was modeled with reasonable success using the Boltzmann equation for the transport of polaritons to the surface.

ACKNOWLEDGMENTS

I would like to thank my supervisor, Dr. M. Thewalt, for his continual encouragement and guidance during the course of this research. These experiments could not have been conducted without the benefit of his experimental skill and insight.

I would like to thank Drs. D.C. Reynolds, R.N. Bhargava and E.S. Koteles for providing me with the various samples used in this work. The collaboration with Dr. E.S. Koteles on the GaAs work proved to be especially fruitful.

I am also indebted to Simon Watkins for proof reading this thesis and to my wife, Claire Driedger, for her unflagging support throughout this endeavour.

The generous financial support of the Natural Sciences and Engineering Research Council, Simon Fraser University and Dr. M. Thewalt is also gratefully acknowledged

Finally, I would like to thank my fellow students and all members of the Physics Department for making my tenure at SFU a thoroughly enjoyable and valuable experience.

TABLE OF CONTENTS

Title ....page i

Approval ....page ii

Abstract ....page iii

Acknowledgments ....page v

Table of Contents ....page vi

List of Figures ....page ix

1 Introduction to Exciton Phenomena ....page 1

1.1 Free Excitons ....page 1

1.2 Bound Excitons ....page 8

1.3 Radiative Decay of BE ....page 11

1.4 Non-Radiative Decay of BE ....page 24

1.5 BE Decay with Third Particle Participation ....page 29

1.6 Polaritons ....page 31

1.7 Other Near-Gap Luminescence Lines ....page 35

2 Introduction to Time-Resolved Spectroscopy ....page 41

2.1 Time-Resolved Spectroscopy ....page 31

2.2 Modelocking ....page 43

2.3 Methods of Modelocking ....page 48

2.4 Synchronous Dye Laser Pumping ....page 52

2.5 Cavity Dumping ....page 54

2.6 Delayed Coincidence Photon Counting ....page 59

2.7 Data Acquisition ....page 63

2.8 Determining the Laser Pulse Width ....page 65

3 Decay of BE in Si ....page 70

3.1 Introduction ....page 70

3.2 Exciton Kinetics ....page 72

3.3 Experimental Results for the Tl,In and Bi BE in Si.page 77

4 Transient Studies of Exciton Luminescence in CdSe ....page 83

4.1 Introduction ....page 83

4.2 Experimental Apparatus ....page 86

4.3 CW Photoluminescence Spectra of CdSe ....page 87

4.4 Transient CdSe Photoluminescence Results ....page 92

4.5 Resonant Excitation of Donor and Acceptor BE ....page 99

5 Photoluminescence Lifetimes of BE in ZnSe ....page 106

5.1 Introduction ....page 106

5.2 Experimental results ....page 108

5.3 Comparison with Theory ....page 111

5.4 Time-Resolved Spectra ....page 116

6 Transient Photoluminescence Study of Defect Lines in MBE GaAs ....page 118

6.1 Introduction ....page 118

6.2 Proposed Microscopic Models ....page 120

6.3 Time-Resolved Spectra.................................page 121

6.4 Resonant Excitation of the g Line ....page 127

7 The Effect of Neutral Donor Scattering on the Time Dependent Polariton Photoluminescence in GaAs ....page 130

7.1 Introduction ....page 130

7.2 Experimental Apparatus ....page 132

7.3 Experimental Results ....page 133

7.4 Polariton Elastic Scattering Theory ....page 139

7.5 Boltzmann Equation Model of Polariton Luminescence.page 147

7.6 Surface Transmission Function ....page 152

7.7 Details of the Numerical Solution of the Boltzmann Equation ....page 157

7.8 Discussion of the Experimental and Model Results ..page 159

Appendix 1 Active Stabilization of the Modelocker ....page 163

Appendix 2 Trailing Pulse Suppressor ....page 167

Appendix 3 Deconvolution Using the Simplex Algorithm ....page 173

References ....page 176

LIST OF FIGURES

1.1	Polariton dispersion curve and group velocity	page 34
2.1	Performance of the trailing pulse suppressor	page 57
2.2	Block diagram of modelocked dye laser system	page 58
2.3	Photon counting experimental apparatus	page 62
2.4	Data collection system	page 64
2.5	Scanning autocorrelator	page 68
2.6	Examples of autocorrelation traces	page 69
3.1	Photoluminescence decay of Tl BE	page 80
3.2	Photoluminescence decay of In BE	page 81
3.3	Photoluminescence decay of Bi BE	page 82
4.1	CW spectrum of CdSe	page 90
4.2	Comparison of 25K and 1.5K CdSe spectra	page 91
4.3	Low power luminescence decay of exciton lines	page 96
4.4	High power luminescence decay of exciton lines	page 97
4.5	Pump power dependence of donor BE lifetime	page 98
4.6	CdSe time-resolved spectra	page 104
4.7	Resonant excitation of BE in CdSe	page 105
5.1	Luminescence decay of BE in ZnSe	page 110
5.2	Comparison of measured BE decay rates with theoretical predictions	page 115
5.3	ZnSe time-resolved spectra	page 117
6.1	Spectrum of MBE GaAs showing KP lines	page 119
6.2	Time-Resolved spectra of GaAs KP lines	page 125
6.3	Luminescence decay of selected KP lines	page 126
6.4	Resonant excitation of the g line	page 129

7.1	Luminescence Spectra of a set of MBE GaAs samples with diminishing donor concentrations	page 135
7.2	Series of time-resolved GaAs polariton spectra	page 136
7.3	The effect of excitation density and wavelength on the time-dependent GaAs polariton spectrum	page 137
7.4	Time-dependent luminescence curves from three different regions within the polariton line	page 138
7.5	Calculated polariton scattering rates	page 146
7.6	Calculated generalized reflection coefficients	page 156
7.7	Time-resolved spectra generated by Boltzmann equation model	page 162
A1.1	Modelocker stabilization circuit	page 166
A2.1	Pockels cell driver circuit	page 171
A2.2	Pockels cell modulator performance	page 172

1 INTRODUCTION TO EXCITON PHENOMENA

1.1 FREE EXCITONS

A free hole and electron in a semiconductor experience a Coulomb attraction which favors the formation of a bound state with a consequent reduction in total energy. This bound electron-hole state is called a free exciton (FE) [1.1]. The two-particle interaction potential is

$$H_{int} = \frac{-e^2}{\epsilon r} \qquad 1.1$$

where ϵ is the dielectric constant which takes into account the screening of the bare Coulomb potential by the polarizability of the host lattice. By analogy to the hydrogen atom the energy spectrum can then be written as

$$E_n = \frac{-e^4 m}{2\hbar^2 \epsilon^2 n^2} \qquad 1.2$$

where m is the reduced mass, $m^{-1} = m_E^{-1} + m_H^{-1}$. These electron and hole masses are effective masses thus crudely taking into account the effect of the lattice on the single, quasi particle excitations. The dielectric constant for semiconductors is of the order 10 and the reduced mass is usually far less than one, leading

to binding energies of the order of meV rather than eV. FE wavefunctions are thus very extended, of order 100 A. Due to the small binding energies FE in most semiconductors are stable only at cryogenic temperatures. These excitons are not localized and are thus free to move around in the crystal hence adding to the energy levels of equation 1.2 a kinetic energy term leading to FE bands

$$E_{nK} = \frac{-e^4 m}{2\hbar^2 \epsilon^2 n^2} + \frac{\hbar k^2}{2M} \qquad 1.3$$

Here $M=m_E+m_H$ is the total effective exciton mass.

The above discussion can be put on a more formal footing. A single particle excitation wavefunction for an electron can be written as

$$\Psi_{\underline{k}}(\underline{r}_E) = u_{\underline{k}}(\underline{r}_E)\exp(i\underline{k}\cdot\underline{r}_E) \qquad 1.4$$

where $u_{\underline{k}}(\underline{r}_E)$ is the periodic part of a Bloch function. This wavefunction is not localized in real space and hence there is no Coulomb attraction between such a state and a corresponding hole state. At the expense of a bit of energy a wavepacket can be formed by expanding around the band extremum wavevector $\underline{k}_O$, in terms of the wavefunctions in equation 1.4, to form a localized excitation. The wavefunction for a localized electron can then be written as a Fourier sum with expansion coefficients $A_{\underline{k}}$

$$\Psi(\underline{r}_E) = \sum_{\underline{k}} A_k u_k(\underline{r}_E)\exp(i\underline{k}\cdot\underline{r}_E) \qquad 1.5a$$

and the corresponding localized hole wavefunction expanded around the valence band extremum $\underline{q}_o$ is

$$\Psi(\underline{r}_H) = \sum_{\underline{q}} B_q u_q(\underline{r}_H)\exp(i\underline{q}\cdot\underline{r}_H) \qquad 1.5b$$

If the particle is not too localized, meaning that the wavefunction is spread out over several lattice constants, the sum over $\underline{k}$ can be restricted to $\underline{k}$ near $\underline{k}_o$. The Bloch functions can then be approximated by the band extremum values and taken out of the sum. This is the essence of the so called effective mass approximation [1.2]. Equations 1.5 now become

$$\Psi(\underline{r}_E) = u_{\underline{k}_o}(\underline{r}_E)\left(\sum_{\underline{k}} A_k\exp(i\underline{k}\cdot\underline{r}_E)\right) \qquad 1.6a$$

$$\Psi(\underline{r}_H) = u_{\underline{q}_o}(\underline{r}_H)\left(\sum_{\underline{q}} B_q\exp(i\underline{q}\cdot\underline{r}_H)\right) \qquad 1.6b$$

The quantities in brackets are slowly varying envelope functions extending over many lattice sites. A localized quasi-particle wavefunction is thus approximated by the band extremum Bloch function modulated by an envelope function.

A two particle exciton wavefunction can be formed from the

product of equations 1.6a and 1.6b where the expansion coefficients A and B have been amalgamated into C

$$\Phi(\underline{r}_E,\underline{r}_H) = u_{\underline{k}_o}(\underline{r}_E)u_{\underline{g}_o}(\underline{r}_H)\left(\sum_{\underline{k},\underline{g}} C(\underline{k},\underline{g})\exp(i\underline{k}\cdot\underline{r}_E+i\underline{g}\cdot\underline{r}_H)\right) \qquad 1.7$$

This again consists of a slowly varying envelope function modulated by Bloch functions. The total symmetry of the FE is given by the direct product of the symmetry of the band edges and the envelope function. This must be kept in mind when deriving selection rules. The wavefunction in equation 1.7 represents a FE located at a specific place in the crystal. This is too restrictive since we expect a FE to be free to move in the crystal, because the interaction potential on a scale of many lattice sites is just the Coulomb potential which depends only on the relative separation. A delocalized FE wavefunction of well defined total wavevector $\underline{K}$ can be constructed by restricting the sum in equation 1.7 so that $\underline{g}+\underline{k}=\underline{K}$, only pairs adding to the right momentum can contribute. The envelope function in equation 1.7 thus becomes

$$\Phi_{\underline{K}}(\underline{r}_E,\underline{r}_H) = u_{\underline{k}_o}(\underline{r}_E)u_{\underline{g}_o}(\underline{r}_H)\left(\sum_{\underline{g}} C(\underline{K}-\underline{g},\underline{g})\exp[i(\underline{K}-\underline{g})\cdot\underline{r}_E+i\underline{g}\cdot\underline{r}_H]\right) \qquad 1.8$$

This effectively removes one of the sums and in essence introduces some delocalization. What is left is delocalized center of mass motion of well defined momentum $\underline{K}$ and an internal wavefunction depending only

on the relative motion of the electron and hole. This can be seen by transforming to center of mass coordinates

$$\underline{R} = \frac{m_E \underline{r}_E + m_H \underline{r}_H}{M} \qquad \& \qquad \underline{r} = \underline{r}_E - \underline{r}_H \qquad 1.9$$

The FE envelope wavefunction part of equation 1.8 can be rewritten as a product of an internal wavefunction and one of center of mass motion

$$\Phi_{\underline{K}}(\underline{R},\underline{r}) = \left(\sum_{\underline{q}} C(\underline{q})\exp(-i\underline{q}\cdot\underline{r})\right)\exp(i\underline{K}\cdot\underline{R}) = \Phi_{int}(\underline{r})\exp(i\underline{K}\cdot\underline{R}) \qquad 1.10$$

The FE wavefunction will then satisfy a Hamiltonian of the form

$$H = \frac{P^2}{2M} + \frac{p^2}{2m} - \frac{e^2}{\epsilon r} \qquad 1.11$$

By analogy to the hydrogen atom problem $\Phi_{int}(\underline{r})$ is given by

$$\Phi_{int}(\underline{r}) = \sum_{\underline{q}} C(\underline{q})\exp(-\underline{q}\cdot\underline{r}) = F_{nlm}(\underline{r}) \qquad 1.12$$

where the $C(\underline{q})$ is the Fourier transform of the hydrogenic functions $F_{nlm}(\underline{r})$.

For the lowest energy state this reduces to

$$\Psi_{int} = \frac{1}{\sqrt{\pi}} \left(\frac{1}{a_x}\right)^{3/2} \exp(-r/a_x) \qquad 1.13$$

where a_x is the FE Bohr radius given by

$$a_x^2 = \frac{\hbar^2}{2mE} \qquad 1.14$$

The energy above the minimum of the band needed to form the localized states is more than recovered by the resulting binding of the localized electron and hole due to the Coulomb potential. Free electrons and holes in a semiconductor at low temperatures are thus unstable to formation of FE which are the lowest energy, intrinsic excitations of the crystal.

Ultimately the electron recombines with the hole and the FE annihilates giving up its energy to create a slightly below band-gap photon which can be detected outside the crystal. A FE has a characteristic luminescence lineshape consisting of a sharp low energy edge corresponding to a FE with zero center of mass motion and a Boltzmann tail to higher energy. Since wavevector must be conserved upon FE annihilation this characteristic line shape is generally seen only in phonon replicas of the FE transition since a phonon is then available to absorb the excess momentum. In the no-phonon region of the spectrum only essentially stationary FE with center of mass

momentum $\underline{K}$~0 can contribute, resulting in a sharp spike for the FE no-phonon lineshape. The radiative decay rate of the FE is determined by the overlap of electron and hole wavefunctions but the observed decay time of the FE rarely corresponds to the radiative rate. The reason for this is that FE are readily trapped on impurities to form bound excitons (BE). The observed decay rate is thus usually the trapping rate.

1.2 BOUND EXCITONS

Lampert [1.3] first suggested that FE could get trapped on donor and acceptor impurities to form BE further reducing their energy by the exciton localization energy of the binding center. He made analogies between an exciton bound to a neutral impurity and the hydrogen molecule as well as an exciton bound to an ionized impurity and the H_2 ion. Hopfield [1.4] discussed the stability criterion in terms of the electron to hole effective mass ratio and determined that excitons bound to neutral impurities are stable for all mass ratios whereas excitons bound to ionized impurities are stable only for restricted values of the mass ratio. Specifically in Si where $m_E \sim m_H$, neither ionized impurity center can bind an exciton, whereas in GaAs where $m_E << m_H$ an exciton bound to an ionized donor is stable while an exciton bound to an ionized acceptor is not. A BE, upon annihilation, gives off a photon of energy less than that of a FE. In fact the exciton localization energy is directly determined optically by measuring the energy difference between the BE and FE lines. There exists an empirical relationship between the exciton localization energy E_{BX} and the impurity binding energy E_i

$$E_{BX} = aE_i + b \qquad 1.15$$

known as Haynes' rule [1.5], where a and b are constants for a given

material. It has been found to hold in many circumstances. In Si a=0.1 and b=0. If effective mass theory were entirely applicable all impurities of the same type i.e. donors or acceptors would have the the same ionization and exciton binding energy. Experimentally the actual energies are often found to vary considerably from the effective mass values and this is attributed to lattice strains or differences in the core potentials of the different impurities. A short range potential, called a central cell potential, is added to the Coulomb potential to account for these differences in binding energy.

A BE line is distinguished optically from a FE line by its extremely narrow line width, since unlike a FE, a BE does not have a Boltzmann tail due to thermal motion. BE were first detected in Si by Haynes [1.5] who, by selective doping, identified lines corresponding to excitons bound to several common impurities in silicon. The neutral impurity wavefunction, as well as the FE wavefunction, are very extended covering up to hundreds of lattice sites, hence the FE trapping cross section to form BE is large. This cross section can be determined optically by measuring the decay rates of the FE and BE, if the density of trapping centers is known. Provided the density of impurities is not so high that BE wavefunctions overlap appreciably the lifetime of a BE is characteristic of the binding center and is the inverse of the sum of the radiative and non radiative decay rates.

A large distinction must be made here between direct and indirect-gap semiconductors. In direct-gap semiconductors BE recombination can proceed without the participation of a momentum

conserving phonon and the radiative rate is large, leading to BE lifetimes of the order of 1 ns. In the case of BE in indirect-gap semiconductors the radiative rate is much reduced due to the needed participation of a momentum conserving phonon. In this case the total decay rate is usually dominated by the non-radiative Auger decay, where the BE energy is given off to the remaining particle of the neutral BE complex. For shallow BE in Si the lifetime of the BE is of the order of μs whereas for deeper BE the lifetime is reduced to less than a ns. The BE decay rate in these different circumstances is the topic of the next sections.

The whole field of BE in various semiconductors, including the effects of external perturbations of the sample, has been extensively reviewed by Dean and Herbert [1.6]. The next sections will discuss only those aspects relevant to time resolved spectroscopy of BE in semiconductors.

1.3 RADIATIVE DECAY OF BE

The BE oscillator strength determined from the strength of the absorption in direct-gap semiconductors is suprisingly large compared to to intrinsic FE absorption, considering the relatively low density of impurity centers. This was first explained by Rashba and Gurgenishvili [1.7,1.8] who showed that a shallow BE possesses a giant oscillator strength proportional to the volume of space covered by the BE wavefunction. The shallowest BE thus have the largest oscillator strengths and conversely the shortest lifetimes. Before deriving this result some background quantities need to be discussed.

A set of classical oscillators with resonance frequency ω_0 driven by a field of frequency ω contributes a polarization per unit volume of [1.9]

$$P_{CL}(\omega) = \frac{Ne^2}{m} \frac{f}{\omega_0^2 - \omega^2} \qquad 1.16$$

where N is the number of oscillators per unit volume, m is the mass of the oscillator and f is the oscillator strength. With a suitable quantum mechanical definition of f the interaction of light with matter can be adequately treated. In the low frequency limit equation 1.16 becomes

$$P_{CL}(\omega \to 0) = \frac{Ne^2}{m} \frac{f}{\omega_0^2} \qquad 1.17$$

From semiclassical radiation theory in the dipole approximation [1.10] we have the following results

$$B_{if} = \frac{4\pi^2 e^2}{3\hbar^2} |\langle \lambda_f | \underline{r} | \lambda_i \rangle|^2 \qquad 1.18$$

Here B_{if} is the Einstein B coefficient [1.11], the induced transition probability per unit time when multiplied by the incident spectral energy density, and the squared term is the dipole matrix element between the initial and final states squared. Furthermore, the quantum mechanical polarization per unit volume in the low frequency limit is [1.12]

$$P_{QM} = \frac{2e^2}{3\hbar\omega_0} |\langle \lambda_f | \underline{r} | \lambda_i \rangle|^2 \qquad 1.19$$

Comparing the classical polarization (equation 1.17) with the quantum mechanical polarization (equation 1.19), a suitable quantum mechanical definition of the oscillator strength f is

$$f = \frac{2m\omega_0}{3\hbar} |\langle \lambda_f | \underline{r} | \lambda_i \rangle|^2 \qquad 1.20$$

The oscillator strength was determined from the dielectric response to an incident electric field in one direction, so on average only 1/3 of the randomly oriented oscillators participated. For the purposes of calculating the radiative lifetime the direction is unimportant and the oscillator strength is therefore a factor of 3 too small. It should be

$$f = \frac{2m\omega_0}{\hbar} |\langle \lambda_f | \underline{r} | \lambda_i \rangle|^2 \qquad 1.21a$$

Using the identity $im\omega\langle m|\underline{r}|n\rangle = \langle m|\underline{p}|n\rangle$ [1.10], this equation can also be written in terms of the momentum matrix element as

$$f = \frac{2}{\hbar m\omega_0} |\langle \lambda_f | \underline{p} | \lambda_i \rangle|^2 \qquad 1.21b$$

In terms of this oscillator strength the equation 1.18 can be rewritten as

$$B_{if} = \frac{2\pi^2 e^2}{3\hbar m\omega_0} f_{if} \qquad 1.22$$

The Einstein A coefficient, or the spontaneous transition rate per unit time, is related to the induced transition rate by [1.11]

$$\frac{A_{if}}{B_{if}} = \frac{\hbar\omega_0^3}{\pi^2 c^3} \qquad 1.23$$

In terms of the oscillator strength, the A coefficient, using equations 1.22 and 1.23 can be written as

$$A_{if} = \frac{2\omega_0^2 e^2}{3mc^3} f_{if} \qquad 1.24$$

We are interested in the radiative lifetime of an excited state. The excited state population is decreased by spontaneous emission of photons, a process which occurs with a probability given by A. In a dielectric medium of refractive index n the induced emission rate is increased by a factor n^3 due to the increased photon density of final states but decreased by n^2 due to the division by the increased incident energy density, yielding a net increase of the coefficient B by a factor of n [1.12]. Since the spontaneous and induced emission rates are related by equation 1.23 the coefficient A is similarly increased by a factor n. The radiative lifetime $\tau=1/A$ in a dielectric medium of refractive index n is thus given by

$$\tau_{RAD} = \frac{3mc^3}{2\omega_0^2 e^2 n} f^{-1} \qquad 1.25$$

This can be written in more convenient units as [1.13]

$$\tau_{RAD} = \frac{4.50\lambda^2}{nf} \tag{1.26}$$

where λ is the transition wavelength in vacuum in cm.

The oscillator strength can conveniently be determined experimentally from the integrated absorption of a transition [1.14]. In terms of the absorption coefficient α which represents the fractional change in intensity dI/I with unit length, the absorbed power W is given by

$$\frac{dW}{dt} = \int \alpha_{i\,f}(\omega) I(\omega) d\omega \tag{1.27}$$

where $I(\omega)$ is the incident light intensity of frequency ω. If the intensity is approximately independent of frequency in the small range where α is non zero, then $I(\omega)$ can be taken out of the integral leaving

$$\frac{dW}{dt} = I(\omega) \int \alpha_{i\,f}(\omega) d\omega \tag{1.28}$$

The absorbed power is also equal to

$$\frac{dW}{dt} = N_i \left(B_{i\,f} \frac{I(\omega)}{c} \right) \left(\hbar\omega_o \right) \tag{1.29}$$

where N_i is the number of absorbing centers in the initial state. The first bracket is the transition probability, per center and unit time, and the second bracket is the energy absorbed per transition. Equating 1.28 and 1.29 and substituting in for the Einstein B coefficient from equation 1.22 gives for the oscillator strength

$$f_{if} = \frac{mc}{2N_i \pi^2 e^2} \int \alpha_{if}(\omega)d\omega \qquad 1.30$$

For an absorption measurement, the appropriate expression for the oscillator strength is equation 1.20 rather than 1.21a, consequently the factor of 3 does not appear in this result.

The momentum matrix element connecting a FE or BE to the crystal ground state can be written as [1.8]

$$M = D\sum_{\underline{k}_E} C(\underline{k}_E, -\underline{k}_E) \qquad 1.31$$

where the C are the expansion coefficients in k-space of the exciton envelope function. The band-to-band matrix element for an allowed transition does not depend strongly on k, and hence can be taken to be constant over the range of k needed in the expansion. It can therefore be taken out of the sum and included in the constant D. Each

electron-hole pair connected by an optical transition thus contributes to the total optical matrix element of the exciton with a weight determined by the expansion coefficient C. Since light has essentially zero momentum compared to electrons, holes, or excitons, only pairs having the hole wavevector opposite to the electron wavevector ($\underline{q}_H = -\underline{k}_E$) are connected via an optical transition. All other pairs are not connected and do not contribute to the total optical matrix element.

The allowed k values are closely spaced and equation 1.31 can be written in the continuum limit as

$$M = \frac{D}{(2\pi)^3} \int \Psi(\underline{k}_E, -\underline{k}_E) d^3k_E \qquad 1.32$$

Ψ is the k-space envelope wavefunction of the exciton. Ψ can be written as a Fourier sum of real space components yielding

$$\Psi(\underline{k}_E, -\underline{k}_E) = \frac{1}{(2\pi)^3} \iint \Psi(\underline{r}_E, \underline{r}_H) \exp[i\underline{k}_E \cdot (\underline{r}_E - \underline{r}_H)] d^3r_E d^3r_H \qquad 1.33$$

Substituting this into equation 1.32 and integrating over k gives

$$M = \frac{1}{(2\pi)^3} \iint \Psi(\underline{r}_E, \underline{r}_H) (2\pi)^3 \delta(\underline{r}_E - \underline{r}_H)] d^3r_E d^3r_H \qquad 1.34$$

Integrating over one of the spatial variables is now trivial due to

the delta function. One has, after integrating over $\underline{r}_H$

$$M = D\int\Psi(\underline{r}_E,\underline{r}_E)d^3r_E \tag{1.35}$$

This is an intuitively pleasing result since it is reasonable that the electron and hole must be at the same place in space in order to recombine. This could have been used as a starting point except that its meaning is not so clear for non-localized Bloch states. Substituting the momentum matrix element from equation 1.35 into equation 1.21b for the oscillator strength gives

$$f = \frac{2M^2}{\hbar m\omega_0} = \frac{D'^2}{\omega_0}\left|\int\Psi(\underline{r}_E,\underline{r}_E)d^3r_E\right|^2 \tag{1.36}$$

where the constants D^2 and $2/\hbar m$ have been amalgamated into the new constant D'^2. If the pair envelope wavefunction consists of the product of a normalized free hole and free electron wavefunctions the integral is identically unity. Hence the constant can be written as

$$D'^2 = f_0\omega_0 \tag{1.37}$$

where f_0 and ω_0 are the band-to-band oscillator strength and frequency respectively. For a, FE with $\underline{K}=0$ and $\underline{r}_H=\underline{r}_E$, the

wavefunction normalized in a volume V, is from equation 1.10,

$$\Psi_{K=0}(r_E, r_H) = \frac{1}{\sqrt{V}} \Phi_{int}(0) \qquad 1.38$$

The FE oscillator strength is thus

$$f_x = f_o V \frac{\omega_o}{\omega_x} |\Phi_{int}(0)|^2 \qquad 1.39$$

The total FE oscillator strength is proportional to the sample volume. A quantity independent of sample size, is the FE oscillator strength per molecular volume Ω_o

$$f_x = f_o \Omega_o \frac{\omega_o}{\omega_x} |\Phi_{int}(0)|^2 \qquad 1.40$$

The ratio of the impurity BE to the FE oscillator strength per unit volume is thus from equation 1.36

$$\frac{f_i}{f_x} = \frac{\left|\int \Psi_i(r_E, r_E) d^3 r_E\right|^2}{|\Phi_{int}(0)|^2 \Omega_o} \qquad 1.41$$

The difference between the frequencies ω_i and ω_x is usually very

small and hence the frequency ratio can be taken as unity. This is the salient result of the work of Rashba and Gurgenishvilli [1.7,1.8]. The numerator is of order unity whereas the denominator is of order Ω_0/a_x^3. a_x is the Bohr radius of the FE. The value of the denominator follows approximately from the normalization condition. The ratio of the impurity to FE wavefunction is thus approximately given by

$$\frac{f_i}{f_x} = \frac{a_x^3}{\Omega_0} \qquad 1.42$$

Since $a_x^3 \gg \Omega_0$, $f_i \gg f_x$ and we have the so called giant oscillator strength effect for impurity BE in direct-gap materials. To evaluate the right hand side of equation 1.41 more accurately one must evaluate the integral over the impurity BE wavefunction approximately. We can proceed as follows. For a weakly bound exciton the BE wavefunction can be expanded in terms non-localized FE wavefunctions in close anlogy to the development of the FE itself in section 1.1

$$\Psi_i(\underline{r}_E,\underline{r}_H) = \sum_{\underline{K}} F(\underline{K})\Psi_{\underline{K}}(\underline{r}_E,\underline{r}_H) \qquad 1.43$$

Substituting in for the FE wavefunction from equation 1.10 this becomes

$$\Psi_i(\underline{r}_E,\underline{r}_H) = \sum_{\underline{K}} F(\underline{K})\Omega_{int}(\underline{r})\exp(i\underline{K}\cdot\underline{R}) = \Omega_{int}(\underline{r})F(\underline{R}) \qquad 1.44$$

where the sum over the expansion coefficients has been written as F(R), another envelope function. In terms of this envelope function equation 1.41 can be written as

$$\frac{f_i}{f_x} = \frac{|\Phi_{int}(0)|^2 \left|\int F(\underline{R})d^3\underline{R}\right|^2}{|\Phi_{int}(0)|^2\Omega_o} \qquad 1.45$$

From this result we see that the ratio of the oscillator strengths is given by the number of molecules contained within the BE wavefunction volume. An F(R) can be found by putting into a Schroedinger equation for F(R) a physically reasonable potential. A simple choice, that adequately describes an exciton weakly bound to a neutral impurity, is a delta function potential with the depth of the potential adjusted to equal the exciton localization energy. The Schroedinger equation for F(R) is thus

$$(\nabla^2-\kappa^2)F(\underline{R}) = \frac{2M}{\hbar^2} E_B\delta(\underline{R}) \qquad 1.46$$

where E_B is the localization energy of the exciton. F(R) is essentially the Green's function for the Helmholtz equation [1.15] with the well known normalized solution

$$F(\underline{R}) = \left(\frac{\varkappa}{2\pi}\right)^{\frac{1}{2}} \frac{\exp(-\varkappa R)}{R} \qquad \& \ \varkappa = \left|\frac{2mE_b}{\hbar^2}\right| \qquad 1.47$$

The value of the numerator in equation 1.45 can now be evaluated using the above expression for F(R).

$$\left|\int F(R)d^3R\right|^2 = \frac{\varkappa}{2\pi}\left|\int \exp(-\varkappa R)4\pi R dR\right|^2 = \frac{8\pi}{\varkappa^3} \qquad 1.48$$

Defining the effective range of the potential as

$$\ell = 1/\varkappa = \frac{\hbar}{\surd(2mE_B)} \qquad 1.49$$

and using equation 1.48 the expression for the impurity oscillator strength, equation 1.45, becomes

$$f_i = f_x \frac{8\pi \ell^3}{\Omega_o} \qquad 1.50$$

The impurity BE oscillator strength should then decrease with increasing BE localization energy E_B as

$$f_l \propto E_B^{-3/2} \quad 1.51$$

The corresponding radiative lifetimes, given by equation 1.26, thus increases with increasing localization energy. For typical BE and FE parameters in a direct-gap semiconductor the BE oscillator strength is of order unity and the radiative lifetime of order 1 ns. The results of this theory will be compared to the experimental results for ZnSe in chapter 5.

In an indirect-gap semiconductor the band edge to band edge matrix element is zero, due to the need to conserve wavevector in an optical transition. The above analysis is thus inappropriate since any no-phonon oscillator strength for an indirect BE is due to the small amplitude large wavevector components of the BE wavefunction. It depends precisely on those small components, for which the Bloch function can not be approximated by the band extremum function. Very shallow BE which consequently have a small spread in k-space thus have exceedingly small no-phonon oscillator strengths. Deeper BE with correspondingly greater k-space spreads have larger no-phonon oscillator strengths. In the case of shallow indirect BE, radiative transitions proceed much more readily with phonon participation. The total radiative oscillator strength is however much smaller than in the direct-gap case, and consequently radiative lifetimes are of the order of us or even ms.

1.4 NON-RADIATIVE DECAY OF BE

A BE can also decay non-radiatively, in which case the observed lifetime is less than the radiative lifetime.

$$1/\tau = 1/\tau_{NONRAD} + 1/\tau_{RAD} \qquad 1.52$$

If the binding center concentration is known, the non-radiative decay rate can be determined by experimentally measuring the integrated absorption, thereby determining $1/\tau_{RAD}$ with help of equation 1.30, and measuring the total lifetime τ thereby determining the non-radiative rate through equation 1.52. Usually one works in the limit of either one of the rates being dominant, in which case the measured decay time will essentially be equal to the inverse of the dominant decay rate. The importance of non-radiative decay in indirect-gap semiconductors was first realized by Nelson et. al. [1.16], who noted that for the P site donor BE in GaP:S, the measured lifetime of 21 ns was 500 times less than the radiative lifetime of 11 us, calculated from the integrated absorption cross section. This fast decay was attributed to Auger decay, in which the annihilation energy of the BE is taken up as kinetic energy by the remaining particle of the neutral impurity BE complex. The remaining particle is injected deep into the conduction band (for electrons) or valence band (for holes), whereafter this hot carrier quickly relaxes by giving off a cascade of phonons. The Auger rate should increase rapidly with

increasing binding energy, since the spread of the bound particle wavefunction in k-space, and hence the overlap with the large wavevector free particle final states, is inversely proportional to the localization in real space. Dean et. al. [1.17] have given qualitative arguments for the dependence of the Auger rate on the exciton localization energy. The argument proceeds as follows. The Auger rate depends on the overlap of the like particles in the BE complex. In a model BE where one of the like particles, a hole say, is tightly bound and the other is weakly bound in a hydrogenic 1S state with effective Bohr radius a, the hole-hole overlap is given by the square of the hydrogenic wavefunction at r=0.

$$|\Psi(0)|^2 = \frac{1}{\pi a^3} \qquad 1.54$$

But a is related to the exciton localization energy through equation 1.14, consequently the interparticle overlap is proportional to

$$|\Psi(0)|^2 \propto E_{Bx}^{3/2} \qquad 1.55$$

The second factor influencing the Auger rate is the spread in k-space of the more tightly bound particle. A greater spread means larger overlap with the free particle final states. Assuming that the tightly bound particle is in a hydrogenic state with effective Bohr radius a, the spread in k-space is given by the Fourier transform of the

hydrogenic 1s wavefunction.

$$\Psi(\underline{k}) = \frac{1}{\sqrt{2\pi}} \int \Psi(\underline{r}) \exp(i\underline{k}\cdot\underline{r}) d^3r$$

$$= \frac{\sqrt{8}}{a^{3/2}} \int \exp(-r/a) r^2 \left(\int \exp(ikr\cos\theta) d(\cos\theta) \right) dr \qquad 1.56$$

$$= \frac{\sqrt{8}}{a^{3/2}} \frac{1}{ik} \int \left(\exp[(ik-1/a)r] - \exp[(-ik-1/a)r] \right) r dr$$

Straight forward integration and algebra gives the result

$$|\Psi(k)|^2 \propto \frac{1}{a^5} \left(\frac{1}{(1/a^2+k^2)^4} \right) \qquad 1.57$$

for the square of the k-space wavefuction, ignoring the constant factors. The effective Bohr radius and free particle wavevector are given by

$$\frac{1}{a^2} = \frac{2m_H E_A}{\hbar^2} \qquad \& \qquad k_f^2 = \frac{2m_H E_f}{\hbar^2} \qquad 1.58$$

where m_H is the effective mass of the ejected hole, E_A is the acceptor binding energy and E_f is the final state energy of the ejected hole assuming a spherical band. In terms of these values, the

square of the wavefunction for $k=k_f$ is proportional to

$$|\Psi(k)|^2_{k=k_f} \propto \frac{E_A^{5/2}}{(E_A+E_K)} \qquad 1.59$$

E_K is almost equal to the band-gap energy which is very much greater than the acceptor binding energy E_A. Hence equation 1.59 becomes

$$|\Psi(k)|^2_{k=k_f} \propto E_A^{5/2} \propto E_{Bx}^{5/2} \qquad 1.60$$

where the last step follows from Haynes' rule equation 1.15. The combined effects of these two factors is that the non-radiative Auger lifetime τ_A is expected to vary as

$$\tau_A \propto E_{Bx}^{-4} \qquad 1.61$$

Experimentally [1.18], for acceptors and donors in Si, the Auger lifetime has been found to obey a power law relationship similar to equation 1.61 with an exponent of −3.9 for acceptors and −4.6 for donors. This is remarkably close agreement considering the crudeness of the model. More quantitative calculations of the Auger rate have been made by various groups [1.19-1.21] with reasonably good results.

In Si, for both neutral donor and acceptor BE the experimentally

determined lifetime is invariably dominated by the Auger decay rate. In the direct-gap materials studied here however the huge radiative rate was found to dominate for the shallow BE.

1.5 BE DECAY WITH THIRD PARTICLE PARTICIPATION

Partially non-radiative decays of BE are also possible. In this case some of the BE energy is taken up by a third particle, either a phonon or the remaining electron or hole of the neutral binding center. Such phonon-assisted transitions have already been mentioned as important decay channels for shallow BE in indirect-gap semiconductors. Spectroscopically this leads to replicas of the main, or no-phonon line shifted to lower energies. The primary importance of this to time-resolved spectroscopy is that all replicas of a given transition must have identical transient behaviour since they originate from the same initial population. This often helps in identifying luminescence lines and in separating spectrally overlapping luminescence features.

In the compound direct-gap semiconductors, the predominant phonon interaction is with small wavevector LO phonons, since these phonons have macroscopic electric fields associated with them and hence couple strongly to electrons and holes. In the case of Si the predominant phonon interaction of the FE and shallow BE is with momentum conserving acoustic and optic phonons.

The other kind of third particle replica is purely electronic in origin. It is in essence a partial Auger decay in which the remaining electronic particle of the neutral BE complex is left in an excited state of the impurity center. In the case of neutral donor (acceptor) centers this is called a two-electron (hole) transition. The electronic excited states of the impurity can thus be mapped out if

these transitions can be observed.If p-type orbital or large quantum number electronic excited states can be observed then the ionization energy of the impurity can be accurately determined from the hydrogenic limit, since the p-type or large quantum number wavefunctions do not sample the central cell region very much. If, as is often the case, one sees only the two-particle transition corresponding to the 1S-2S transition, then the ionization energy can be approximately determined to be 4/3 of the energy splitting between the principal and 2 particle satellite line. These partial Auger transitions were first observed and identified by Dean et. al. [1.22] for P site donors in GaP, although Thomas and Hopfield had postulated their existence earlier [1.23].

1.6 POLARITONS

In direct-gap semiconductors with electric dipole active exciton transitions, there exists a strong coupling of the FE with light of the same wavevector. This coupling, as pointed out by Hopfield [1.24], results in a mixed mode excitation called a polariton. The polariton dispersion curve is presented in figure 1.1a. The coupling opens up a gap at the crossing point resulting in a two branch polariton dispersion curve given by

$$\left(\frac{\hbar ck}{E}\right)^2 = \epsilon_o + \frac{2\epsilon_o E_{LT} E}{E_o^2(k) - E^2} \qquad 1.62$$

where ϵ_o is the dielectric constant in the absence of polaritons, E_{LT} is the splitting between the longitudinal uncoupled FE and the coupled transverse polaritons (and is thus a measure of the coupling strength), E is the polariton energy and $E_o(k)$ is the energy of the uncoupled FE of wavevector k which is equal to the transverse exciton energy E_T plus the kinetic energy term. In the near resonance region $E_o(k)-E \ll E$ the dispersion relation can be approximately written as

$$\left(\frac{\hbar ck}{E}\right)^2 = \epsilon_o + \frac{\epsilon_o E_{LT}}{E_o(k) - E} \qquad 1.63$$

On the lower branch, at large wavevectors the polaritons are predominantly exciton-like whereas at small wavevectors they are

photon-like. On the upper branch the polaritons start out exciton-like but rapidly become photon-like with increasing wavevector.

The nature of the polariton dispersion relation has a profound effect on the luminescence mechanism in this energy region [1.25,1.26]. Note that the lower polariton branch does not have a minimum energy. Exciton-like polaritons can be inelastically scattered to the lower energy photon-like region of the dispersion curve. These photon-like polaritons interact only weakly with the lattice and rapidly leave the crystal. Toyozawa [1.25] predicted that in the "knee" region of the lower dispersion curve a "bottleneck" to further inelastic scattering to lower energy would result due to a lack of suitable phonons and the small density of final states in the photon-like region of the dispersion curve. The existence of this bottleneck has been experimentally verified with time resolved photoluminescence [1.26,1.27]. Due to this bottleneck, a quasi-thermal equilibrium of polaritons can be established above the knee of the dispersion curve. The group velocity of the polaritons, $v=(1/\hbar)dE/dk$, varies very rapidly with energy [1.28] and has a minimum just above the knee of the lower polariton branch (figure 1.1b). Velocity dependent scattering processes are greatly enhanced in this energy region. This enhancement in scattering, together with the low group velocity, results in much slower diffusion of these polaritons.

For uncoupled FE in a direct-gap semiconductor, no-phonon luminescence can only result if an almost stationary exciton of the same wavevector as light of the exciton energy annihilates giving up its energy to a photon which then travels unhindered to the surface to

emerge as luminescence. In the case of polaritons the distinction between exciton and photon cannot be made, since excitations in this energy region are inherently mixtures. No-phonon polariton luminescence results from those polaritons, which upon reaching the surface, are transmitted as light. This means that a theoretical description of polariton luminescence becomes a transport problem [1.29]. This introduces considerable complexity to the luminescence problem with the net result that the experimentally observed no-phonon polariton luminescence line shape does not necessarily reflect the population distribution of polaritons in the interior of the semiconductor.

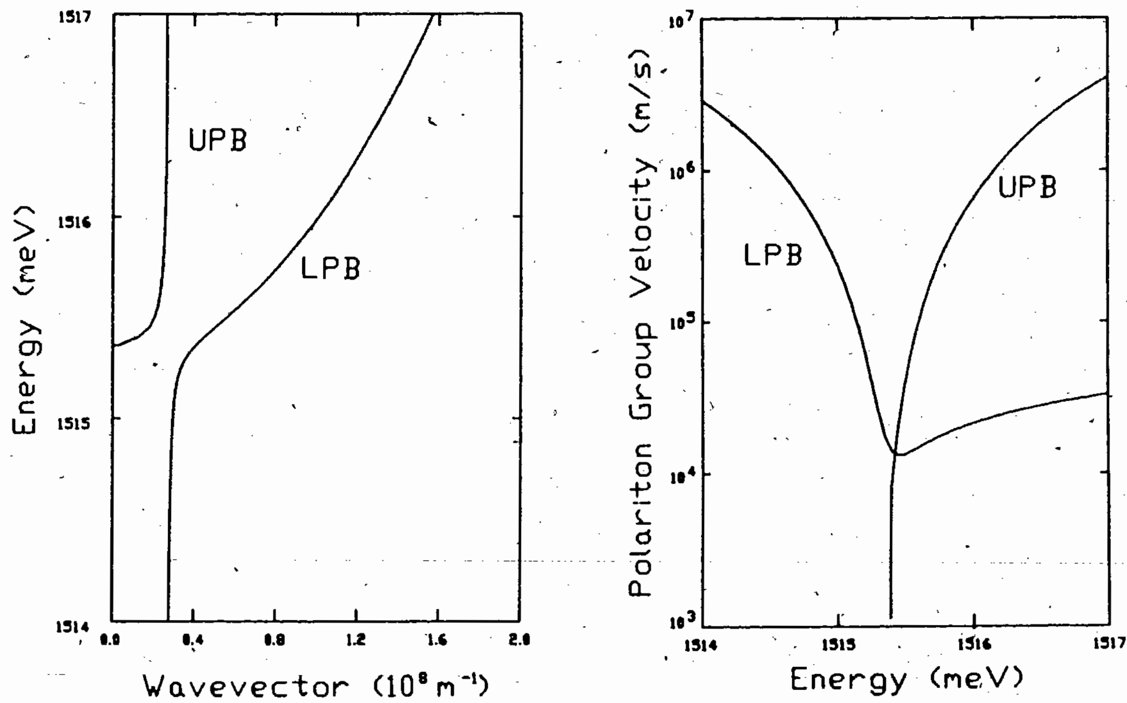

Figure 1.1

A) This is the calculated polariton dispersion curves for GaAs using the parameters suitable for GaAs (chapter 7) and equation 1.63. The upper (UPB) and lower (LPB) polariton branches are labelled.

B) These are the LPB and UPB group velocities calculated from equation 1.63

1.7 OTHER NEAR-GAP LUMINESCENCE LINES

Non-excitonic luminescence lines are also sometimes seen in the near band-gap energy region. These transitions are either neutral donor to neutral acceptor pair (DAP) recombination, or free carrier to neutral impurity transitions. The energy of a luminescence photon resulting from a DAP recombination is given by [1.30]

$$E_{DAP} = E_G - (E_A + E_D) + \frac{e^2}{\epsilon R} \qquad 1.64$$

where E_G, E_A and E_D are the band-gap, acceptor and donor binding energies respectively, ϵ is the dielectric constant and R is the pair separation. The appearance of the Coulomb term in equation 1.64 can be understood by following an energy cycle. The binding energy of a hole on an ionized acceptor is reduced by the presence of a nearby ionized donor core adding a repulsive potential. The subsequent binding of an electron on the ionized donor is not appreciably affected by the now neutral acceptor. The summed binding energy of the electron and hole on the DAP is thus

$$E_{pair} = E_A + E_D - \frac{e^2}{\epsilon R} \qquad 1.65$$

R is quantized due to the fact that the donor and acceptor must occupy well-defined lattice sites. In very pure samples sharp lines

corresponding to close DAP are sometimes observed. For more distant DAP recombination the spectrum becomes quasi-continuous and the observed luminescence feature is a very broad peak consisting of contributions from many DAP of different separations.

Free-to-bound transitions, namely free electron to neutral acceptor (A^o,e) or free hole to neutral donor (D^o,h), are observed at a photon energy below the gap corresponding to the binding energy of the neutral impurity. These lines are usually characterized by a Boltzmann tail to higher energy, reflecting the initial kinetic energy of the free particle, provided the impurity is deep enough that the necessary larger wavevector contributions exist in the k-space expansion of the impurity wavefunction.

The DAP oscillator strength can be calculated from equation 1.41 [1.13] as follows. The donor and acceptor are both assumed to bind the electron and hole respectively in the 1S-like hydrogenic states. Furthermore, as is the case in GaAs as well as the II-VI compounds studied here, $m_E << m_H$, meaning that the donor wavefunction is much more extended than the acceptor wavefunction. A particular pair is also assumed to be isolated from the effects of other impurities. Picking the center of our coordinate system to lie at the acceptor core the DAP wavefunction can be written as

$$\Psi_{DAP}(\underline{r}_E,\underline{r}_H) = \Phi_A(\underline{r}_H)\Phi_D(\underline{r}_E)$$

$$= \left(\frac{1}{\sqrt{\pi}}\frac{1}{a_A^{3/2}}\exp(-r_H/a_A)\right)\left(\frac{1}{\sqrt{\pi}}\frac{1}{a_D^{3/2}}\exp[-|\underline{r}_E-\underline{R}|/a_D]\right) \qquad 1.66$$

The integral in equation 1.41 can then be approximately evaluated by taking the donor wavefunction to be constant over the whole space covered by the acceptor wavefunction, and equal to the value evaluated at the acceptor core. This is consistent with the assumption that $a_D >> a_A$. The integral thus becomes

$$\left|\int \Psi_{DAP}(\underline{r}_H, \underline{r}_H) d^3r_H\right|^2 = \left|\phi_D(R) \int \phi_A(r) d^3r\right|^2 \quad 1.67$$

$$= 64\pi a_A^3 |\phi_D(0)|^2 \exp(-2R/a_D)$$

Substituting this into the expression for the oscillator strength in terms of the FE oscillator strength equation 1.41, yields

$$f_{DAP} = f_x |\phi_D(0)/\phi_x(0)|^2 (32\pi a_A^3/\Omega_O)(\omega_X/\omega_{DAP}) \exp(-2R/a_D) \quad 1.68$$

The extra factor of 1/2 arises because the electron and hole must have opposite spin to recombine and this occurs, on average, in one half of the cases. Note, in particular, the strong dependence of the oscillator strength on the pair separation R. The oscillator strength decreases exponentially with increasing pair separation. This has profound implications on the time resolved spectra of a DAP band. The observed peak of the DAP band shifts to lower energy with increasing time delay after excitation since, at long delay times, only DAP pairs

with large R have failed to recombine. This is the characteristic signature of a DAP band.

The free-to-bound oscillator strength can also be calculated along the above lines. The pair envelope wavefunction appearing in the integral of equation 1.41 is in the case of a free hole and a bound electron

$$\Psi_{FB}(\underline{r}_H,\underline{r}_E) = \Phi_f(\underline{r}_H)\Phi_D(\underline{r}_E)$$

$$= \left(\frac{1}{\sqrt{V}}\exp(i\underline{q}\cdot\underline{r}_H)\right)\left(\frac{1}{\sqrt{\pi}a^{3/2}}\exp(-r/a_D)\right) \qquad 1.69$$

Choosing the core of the donor as the origin the integral of equation 1.41 becomes

$$\int\Psi_{FB}(\underline{r}_E,\underline{r}_E) = 8\left(\frac{\pi}{V}\right)^{1/2}\left(\frac{1}{a_D}\right)^{5/2}\frac{1}{(1/a_D^2+q^2)} . \qquad 1.70$$

From this result one can see that the integral, and hence the oscillator strength, decreases rapidly with increasing q particularly if the impurity wavefunction is diffuse, i.e. a_D small. This is the factor that causes the characteristic Boltzmann tail of free-to-bound transitions to be cut off for very shallow bound states. The largest oscillator strength is obtained for q=0, for which case the integral of equation 1.70 squared becomes

$$\left|\int \Psi_{FB}(r_E, r_E)\right|^2 = \frac{64\pi\hbar^3}{\sqrt{8}V(m_E E_D)^{3/2}} \qquad 1.71$$

Here m_E is the electron effective mass and E_D the donor binding energy. This result can be inserted in equation 1.41 with some modifications. The oscillator strength so obtained must be multiplied by the total number of neutral donors in the sample $N_D V$, where N_D is the neutral donor density. This is necessary since the free particle is totally delocalized and can interact with all impurities at once. The free hole to neutral donor oscillator strength is thus given by

$$f_{FB} = N_D V f_o \frac{\omega_B}{\omega_{FB}} \left|\int \Phi_{FB}(r_E, r_E) d^3 r_E\right|^2$$

$$= \frac{f_X}{|\Phi_X(0)|^2 \Omega_o} \frac{64\pi\hbar^3}{\sqrt{8}(m_E E_D)^{3/2}} \frac{\omega_X}{\omega_{FB}} N_D \qquad 1.72$$

The analogous result for the free electron to neutral acceptor oscillator strength is obtained from equation 1.72 by replacing m_E, E_D and N_D by m_H, E_A and N_A. The factor of 1/2 that occurred in the DAP case is cancelled here by an extra factor of 2 arising from the fact that a free particle, being totally delocalized, does not impose a particular polarization on the emitted light and can couple to both polarizations unlike the other cases discussed earlier. This result is identical to the result quoted by Pankove [1.31] when rewritten in terms of the averaged band-to-band matrix element instead

of the FE oscillator strength.

2 INTRODUCTION TO TIME-RESOLVED SPECTROSCOPY

2.1 TIME-RESOLVED-SPECTROSCOPY

The extension of spectroscopy into the time domain can yield valuable information on the interactions of elementary excitations in solids [2.1]. These interactions typically proceed on a picosecond time scale, and hence have only recently been experimentally accessible. Time-resolved luminescence measurements are sometimes possible without pulsed laser excitation by sinusoidally modulating the laser output and measuring phase shifts, with respect to the excitation, in the induced luminescence [2.2,2.3]. This method is essentially limited to single exponential decays and the results are thus easily misinterpreted.

The technique of modelocking [2.4-2.7] the axial modes of a laser provides the means of reliably generating picosecond and sub-picosecond pulses for use in time-resolved spectroscopy. With pulsed lasers, non-linearities in the luminescence intensities can be employed to generate correlation functions [2.8-2.10] which yield time information even without fast detectors. This technique is in principle similar to the second harmonic generation method of determining the laser pulse width described in section 2.8. A simpler, more reliable method is the use of pulsed lasers and direct measurement of the decay of the luminescence with time. Currently, the best time resolution (<10 ps) is obtained with streak cameras [2.11-2.13], but photomultipliers are rapidly approaching this time

resolution [2.14] and in addition have much better dynamic range and sensitivity.

The advent of modelocked lasers and concurrently, the development of fast photomultiplier tubes and streak cameras, has enabled the direct measurement of luminescence decay to be pushed into the picosecond regime. This opens up the possibility of experimentally studying the dynamical interactions of elementary excitations in solids. A survey of experimental techniques and applications of ultrashort light pulses has been given in several recent publications [2.15,2.16].

2.2 MODELOCKING

A laser resonator places restrictions on the allowed wavevectors of the light in lasing modes. An electro-magnetic wave corresponding to an allowed mode must have exactly the same phase after one round trip through the laser cavity [2.17]. Consider a cavity consisting of plane mirrors separated by a distance L. The above criteria is thus expressed mathematically as

$$k \cdot 2L = 2\pi m \qquad 2.1$$

where k is the wavevector of light, i.e. the change of phase with distance, and m is an integer. Each of the values of k above corresponds to an allowed axial laser mode. In an inhomogeneously broadened laser many of these axial modes will generally be above threshold and lase simultaneously [2.18]. The number of such modes can be very large due to the close spacing in frequency given by

$$\Delta f = \frac{\Delta\omega}{2\pi} = \frac{c\Delta k}{2\pi\sqrt{\epsilon}} = \frac{c}{2L\sqrt{\epsilon}} \qquad 2.2$$

In the ~1.5 m long cavity of an argon ion laser the mode spacing is thus ~100 MHz, and the number of participating modes within the ~5 GHz Doppler broadened bandwidth is about 50. In a similarly dimensioned dye laser the bandwidth is much larger and thousands of axial modes

can participate. For a laser operating in the TEM_{00} mode meaning that the intercavity electric field depends only on the axial coordinate x, the allowed cavity modes are standing waves of the form

$$E_m = E_{m0}\cos\left(\frac{\pi m x}{L}\right)\cos\left(\frac{\pi m c t}{L} + \phi_m\right) \qquad 2.3$$

Focusing our attention on a particular point in space, the time dependent electric field can be written as a sum of contributions from the different axial modes

$$E(t) = \mathrm{Re}\left(\sum_{m=-n}^{n} E_n \exp[(\omega_0 + m\Omega)t + \phi_m]\right) \qquad 2.4$$

where ω_0 is the angular frequency of the center mode, Ω is the angular mode spacing frequency and ϕ_m is the phase of the mth mode. For simplicity each mode will be assumed to be of equal amplitude E_0. A common factor can then be extracted from the sum leaving

$$E(t) = \mathrm{Re}\left(E_0\exp(\omega_0 t)\left(\sum_{m=-n}^{n}\exp(m\Omega t + \phi_m)\right)\right) \qquad 2.5$$

This has the form of a carrier wave, at the center mode frequency, modulated by the sum term. Normally the phases of the modes change randomly and the resultant field fluctuates unpredictably. If,

however, the phases can be locked together [2.19] such that

$$\phi_{m+1} - \phi_m = \phi \qquad 2.6$$

where ϕ is a constant ϕ_m becomes $m\phi$ and the sum in equation 2.5 becomes a geometric series which can easily be summed to yield

$$E(t) = E_o \cos\omega_o t \left(\frac{\sin[(2n+1)(\Omega t + \phi)/2]}{\sin[(\Omega t + \phi)/2]} \right) \qquad 2.7$$

The power output, which is proportional to the electric field amplitude squared, of such a laser is thus

$$P(t) = \frac{1}{2} T c \epsilon_o E_o^2 \left(\frac{\sin^2[(2n+1)(\Omega t + \phi)/2]}{\sin^2[(\Omega t + \phi)/2]} \right) \qquad 2.8$$

where T is the transmission of the output coupler and ϵ_o is the vacuum dielectric constant. The factor of 1/2 arises from averaging over the very rapid oscillations of the center frequency. The time origin has been chosen to eliminate the constant phase factors. Several interesting conclusions can immediately be drawn from this result. First, it is periodic with period $\tau = 2\pi/\Omega$ which, through equation 2.2 can be seen to be the round trip time of an optical pulse in a laser cavity of length L. Second, the power is concentrated in short pulses occurring at times when the denominator in equation 2.8

is zero. The limit of equation 2.8, for t tending to $j\tau$, where j is any integer, is

$$P(t)_{t \to j\tau} = \frac{1}{2}Tc\epsilon_o E_o^2 (2n + 1)^2 = \frac{1}{2}Tc\epsilon_o E_o^2 N^2 \qquad 2.9$$

where N=2n+1 is the number of participating modes. In contrast, for N modes with random phases, the power is obtained by summing the powers in the N modes thus obtaining

$$P(t)_{t \to n\tau} = \frac{1}{2}Tc\epsilon_o E_o^2 N \qquad 2.10$$

The modelocking thus causes a peak power enhancement proportional to the number of participating modes. The pulse width, taken as the time between nodes, can be found by looking at only the numerator in equation 2.8 since, if the number of participating modes is large, the numerator changes much more rapidly than the denominator. The pulse width is thus equal to the period of the sine function in the numerator

$$\Delta t = 2\pi/N\Omega = 2\pi/\Delta\omega \qquad 2.11$$

Here $\Delta\omega = N\Omega$ is the gain bandwidth of the laser. The pulse width is thus inversely proportional to the available bandwidth. This is just

the usual statement that the product of the time and frequency spread should be of order 1. The exact value depends on the pulse shape. The mödelocked laser thus operates in an intrinsically pulsed mode, with a repetition rate set by the round trip time of the optical pulse in the cavity. What remains to be seen is how this locking of phases can be achieved.

2.3 METHODS OF MODELOCKING

Modelocking is achieved by modulating the laser gain, or loss, at the pulse round trip frequency Ω [2.20]. Assume that a laser, which is lasing on one axial mode, is modulated at the round trip frequency by a sinusoidal function of the form

$$M = \{1 + \delta\cos(\Omega t + \Phi)\} \quad 2.12$$

where δ, the modulation amplitude, is <1 and Φ is the phase of the modulation. The resultant field, at the modulator, is thus

$$\begin{aligned} E_m(t) &= ME_{mo}\cos(\omega_m t + \phi_m) \\ &= E_{mo}\{1 + \delta\cos(\Omega t + \Phi)\}\cos(\omega_m t + \phi_m) \end{aligned} \quad 2.13$$

With the help of a trigonometric identity, this can be rewritten as

$$\begin{aligned} E_m(t) &= E_{mo}\left(\cos(\omega_m t+\phi_m) + \frac{\delta}{2}\cos((\omega_m+\Omega)t+\phi_m+\Phi) + \frac{\delta}{2}\cos((\omega_m-\Omega)t+\phi_m-\Phi)\right) \\ &= E_{mo}\left(\cos(\omega_m t+\phi_m) + \frac{\delta}{2}\cos(\omega_{m+1}t + \phi_{m+1}) + \frac{\delta}{2}\cos(\omega_{m-1}t + \phi_{m-1})\right) \end{aligned} \quad 2.14$$

The phase of the sideband, relative to the fundamental, is a constant

$$\phi_{m+1} - \phi_m = \phi \qquad 2.15$$

fixed by the phases of the fundamental and the modulator. This is precisely the modelocking condition of equation 2.6. The sidebands, being allowed axial modes, are amplified by stimulated emission and in turn generate sidebands of their own, until all the allowed axial modes under the laser gain profile oscillate. The phases of all these modes are now related through equation 2.6. The modes all transfer energy amongst each other and this prevents the phase of a mode from drifting, since a reference phase is continually being supplied from the mode's neighbours by this energy transfer. A more rigorous discussion of modelocking can be found in Yariv [2.18], but no greater physical insight into the modelocking mechanism is gained.

The modulation of the laser gain can be achieved using a saturable absorber, a Pockels cell, or an acousto-optic device near one of the cavity mirrors. For the Argon ion laser used in this work, modelocking was achieved with an acousto-optic modulator driven at 1/2 of the cavity mode spacing frequency of 82 MHz. This establishes an acoustic standing wave in the crystal, provided this frequency is also an acoustic resonance of the modulating crystal. The crystal resonance frequency can be temperature tuned to exactly 1/2 of the mode spacing frequency. A method of locking the crystal resonance to the drive frequency by actively varying the RF power supplied to the crystal is described in appendix 1. Such an arrangement ensures that a good standing wave is always present, a necessary precondition for reliable

modelocking. Whenever the acoustic wave amplitude goes through zero (twice per cycle) the transmission through the cell is at a maximum. At other times, some of the light is diffracted out of the cavity by the acoustically induced refractive index grating, thus producing some loss. This technique of modelocking a CW laser by externally modulating the gain at exactly the cavity round trip frequency is called active modelocking. For an argon laser, which has a bandwidth of approximately 5 GHz on a given laser transition, it is possible to generate pulses of width ~200 ps by this method.

The discussion of modelocking so far has been confined to the frequency domain. Modelocking can also be understood in the time domain. Here one imagines a fast shutter in the laser cavity near one of the end mirrors opened for a short period with a repetition rate equal to the round trip time of a pulse in the cavity. Only a pulse which arrives at the shutter when it is open can be sustained. The pulse can, however, be substantially shorter than the length of time the shutter is open, but this is harder to understand in this picture. Fast turn off can be readily understood, since the inversion can be depleted after passage of the large pulse. This cuts off any trailing wings. The origin of the fast turn on is however not so obvious. An actual shutter can be constructed using a cell containing a saturable absorbing dye. A large pulse bleaches the dye and propagates through it without much loss. Subsequent smaller pulses arriving after the dye has recovered are unable to bleach the dye and are thus strongly attenuated. This leads to a so called passively modelocked laser.

Both descriptions of modelocking are formally identical to each

other, but certain aspects of modelocking are easier to understand in either the frequency or time domain. Both points of view can be used interchangeably. A laser is said to be completely modelocked when <u>all</u> the axial lasing modes are locked together. This results in a train of pulses, whose width is said to be transform limited, with a repetition rate set by the cavity round trip time. Such a laser provides an ideal source for time-resolved spectroscopy on a ns or ps time scale.

2.4 SYNCHRONOUS DYE LASER PUMPING

An actively modelocked ion laser can be used to synchronously pump a dye laser, which will then automatically also be modelocked, provided the dye laser cavity length is precisely matched to the pump laser cavity length [2.21]. With this geometry the circulating dye laser pulse arrives at the dye jet just after the pump pulse has brought the dye to threshold. This can result in extremely short pulses, since the leading edge of the pulse arrives at the dye jet when the gain is still below threshold, whereas the trailing edge arrives after the pulse peak has depleted the inversion, thus putting the gain below threshold [2.22]. The peak of the pulse is thus amplified, while the skirts of the pulse are suppressed, resulting in pulses substantially shorter than the pump pulses, provided the necessary bandwidth exists. The process of synchronously pumping can also be understood in the frequency domain. The dye laser gain is modulated by a train of pump pulses rather than a sinusoid, but because of its periodicity, the modulation can be expressed as a Fourier sum containing only contributions of frequency an integral multiple of the cavity axial mode spacing frequency. The situation is thus as in the previous section, except that a single mode now transfers energy to a whole host of neighbours, rather than just its nearest neighbours. In any case, the modes are again locked together in phase and because of the large available dye laser bandwidth, this can result in very short modelocked laser pulses. Pulses shorter than 100 fs [2.23,2.24] have recently been achieved. Adding a tuning

element to the dye laser allows the generation of tunable modelocked pulses at the expense of pulse width. A spectral width of 0.5 meV, which corresponds to ~125 GHz, results in a transform limited pulse width of order 10 ps. This spectral width is narrow enough to allow resonant excitation of particular exciton luminescence features, while still being short enough to be considered a delta function excitation pulse given the time resolution limits of the detection system employed in this work. A synchronously pumped dye laser system as described here is thus capable of delivering a continuous train of tunable, modelocked pulses, of spectral linewidth ~0.5 meV, time duration ~10 ps, and at a repetition rate of 82 MHz.

2.5 CAVITY DUMPING

The pulse repetition rate of a modelocked laser is set by the cavity length and is thus not easily variable. The modelocked laser used in this work has an intrinsic repetition rate of 82 MHz corresponding to a period between pulses of ~12 ns. This is inconveniently short when measuring the decay of a system with a lifetime in the ns range, since the next laser pulse arrives before the luminescence has a chance to decay completely. A method of lowering the repetition rate would thus be desirable.

This can be done by replacing the partially transmitting output mirror by a totally reflecting one and placing an acousto-optic deflector crystal, called a Bragg cell, in the laser cavity at a beam waist near one of the end mirrors. Output coupling is now achieved by launching a short acoustic wave in the crystal, which deflects a part of the beam out of the crystal by Bragg diffraction [2.25] from the induced, transient refractive index grating. Bragg diffraction efficiencies can be very large (>70%) [2.25,2.26] and thus most of the intracavity energy can be dumped out of the cavity in one pulse. By synchronizing the cavity dumper driver and the modelocker driver, the timing of the applied acoustic wave can be adjusted so that it is launched just before a modelocked pulse arrives at the Bragg cell. Thus, provided the acoustic wave has travelled out of active region impinged upon by the light before the next modelocked pulse arrives, only one pulse is ejected from the cavity. By this method, pulses can

be ejected from the laser cavity at a rate corresponding to an arbitrary submultiple of the intrinsic, modelocked repetition rate. An added bonus of cavity dumping is greater peak power. This occurs because of the increased cavity Q at times when there is no Bragg deflection, thereby allowing the modelocked pulse to build up to a greater intensity.

One important parameter characterizing cavity dumper performance is the trailing pulse (the next modelocked pulse) suppression. Typically, a commercial cavity dumper is specified as having a trailing pulse suppressed by a factor of order 500 [2.26]. These trailing pulses can still appear as annoyingly large peaks on a logarithmic scale (figure 2.1) and can interfere with lifetime fits to the data. The trailing pulses can be further suppressed by following the cavity dumper with a Pockels cell, triggered to cut off transmission right after the main pulse has passed through. Only the cut off of transmission needs to be rapid, the buildup to full transmission need be only fast enough so that full transmission is restored before the next cavity dumped pulse arrives. The maximum cavity dumper repetition rate is 4 MHz, thus full transmission must be restored in 250 ns while transmission must be cut off in 12 ns. These relaxed Pockels cell drive requirements can readily be achieved by simple circuitry, as described in appendix 2. The result is depicted in figure 2.1, which shows an additional suppression of order 100, resulting in a total trailing pulse suppression of order 10^5.

This completes the description of the synchronously pumped, cavity dumped, modelocked dye laser used in this work as an excitation

source for the time-resolved spectroscopy of semiconductors. A block diagram of the complete system is shown in figure 2.2.

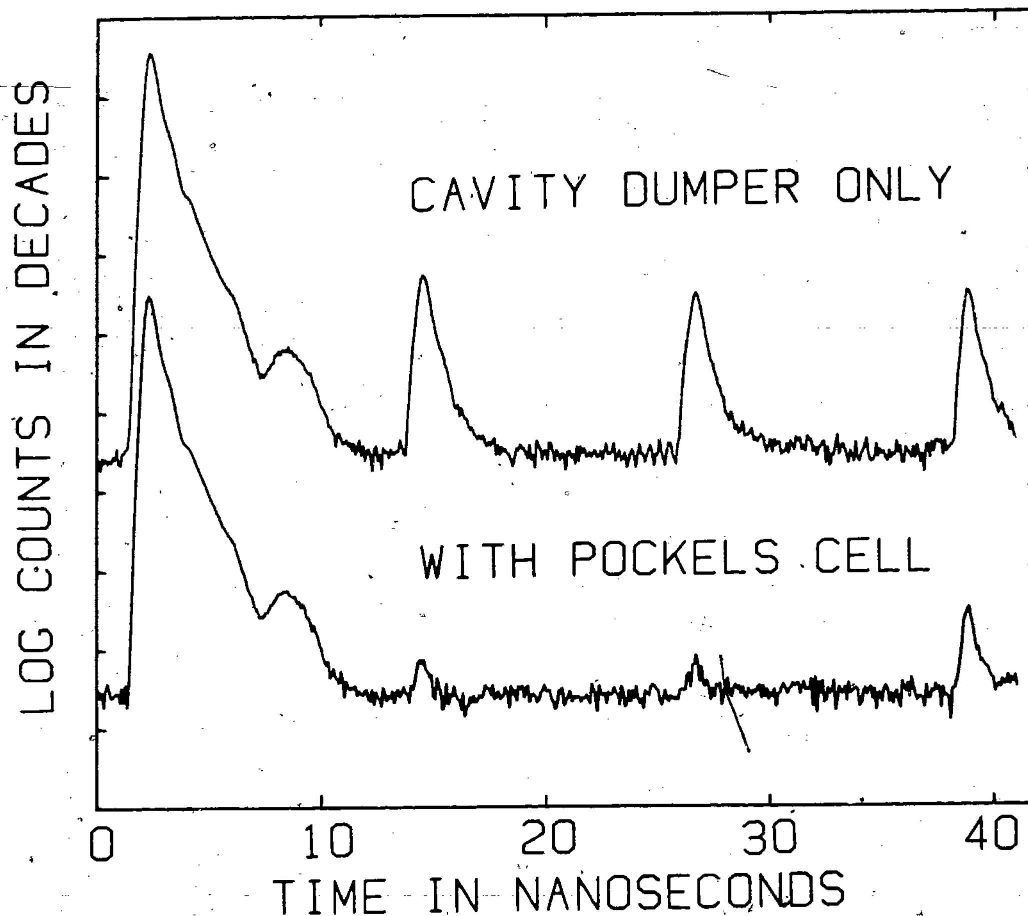

Figure 2.1

Top curve: output of the mode-locked cavity dumped laser system at 600 nm and a 4 MHz repetition rate without the modulator as detected by the Varian photomultiplier tube described in section 2.6. The main pulse and three trailing pulses are shown. The markers along the vertical axes represent decades.

Bottom curve: as above but with the Pockels cell trailing pulse suppressor added.

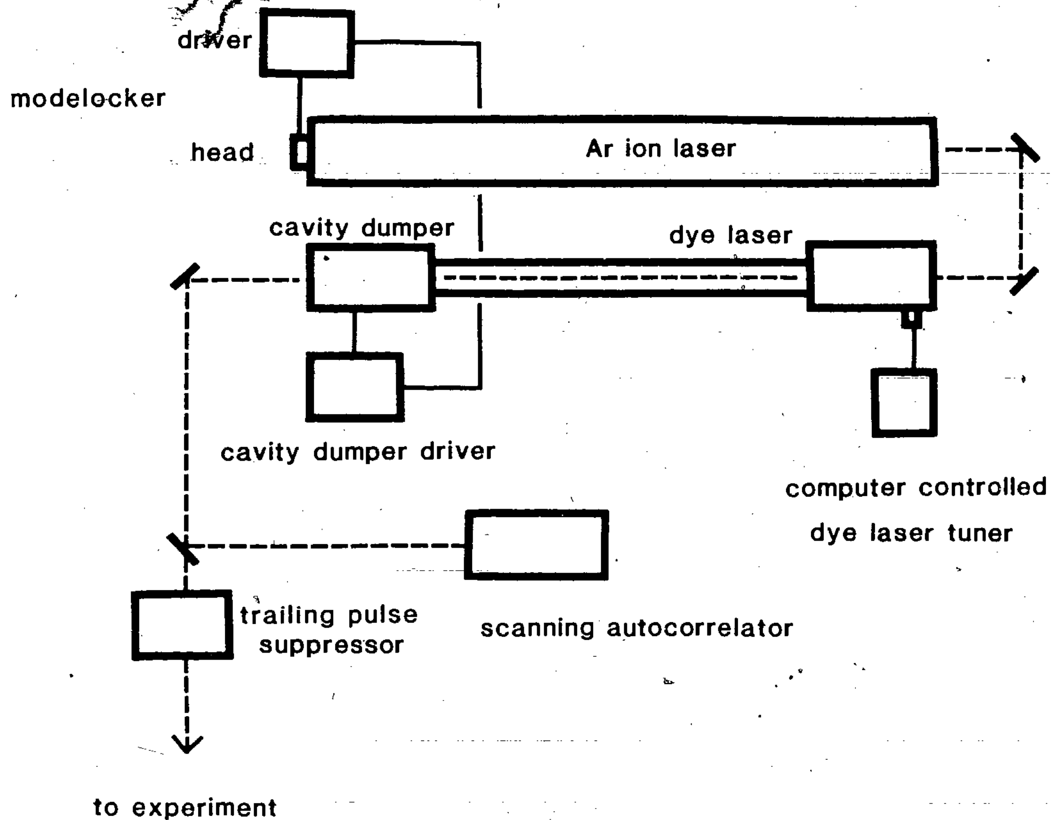

Figure 2.2

This is a block diagram of the synchronously pumped, cavity dumped dye laser system used to generate tunable, picosecond laser pulses.

2.6 DELAYED COINCIDENCE PHOTON COUNTING

Photoluminescence lifetime measurements can be made with a technique borrowed from nuclear physics called delayed coincidence photon counting. Figure 2.3 is a schematic diagram of the data collection system. The time measurement is done by the TAC or time-to-amplitude-converter. A start pulse to this device starts a voltage ramp which ramps up until a stop pulse arrives. The terminal voltage is then clamped and appears as a pulse at the output of the TAC. The output voltage is thus proportional to the time difference between the start and stop pulses. Remarkably, the time resolution of a good TAC is less than 10 ps [2.27]. The output of the TAC is then digitized by an analog to digital converter and sent to a computer. The computer thus receives a number corresponding to the time difference between the start and stop pulses for each pair of pulses. The computer interprets this number as an address in a memory bank and increments the number at that address by one. After collecting many such numbers, a histogram of the luminescence decay is built up in memory.

The luminescence from the sample, after being analyzed by a spectrometer, is detected by a photomultiplier tube operating in the photon counting mode. When a photon is detected, the resulting photomultiplier current triggers the constant fraction discriminator, and a start pulse is generated and applied to the TAC. The stop pulses are generated by sampling a portion of the exciting laser beam with an avalanche photodiode the output of which is fed to a second constant

fraction discriminator. The stop pulses are delayed with a long coaxial line so that they arrive at the TAC sometime after the start pulses. The stop rate is the same as the laser repetition rate whereas the start rate is much lower, since a luminescence photon is not detected for every laser pulse. This choice of start and stop is much more efficient than the more intuitive reverse choice since the TAC has a reset dead time of ~10 μs after each start pulse initiated cycle. A high start rate, corresponding to the repetition rate of a modelocked laser, would result in the luminescence stop pulses overwhelmingly arriving during this reset time and hence being wasted. In the reverse arrangement employed here however a TAC cycle is only initiated when a luminescence photon is detected, thus each luminescence photon contributes to the histogram of the decay. The luminescence count rate must be kept low enough that the probability of detecting two luminescence photons per laser pulse is very low [2.28,2.29]. This is necessary since the above method can only process one photon per cycle, and distortions of the data would result if a significant number of photons were missed. Practically this means keeping the luminescence count rate a factor of 1000 or so below the laser pulse rate. This data collection scheme is ideally suited for modelocked laser excitation since the high repetition rate of such lasers allows a histogram with good signal to noise to be collected in a short space of time. Typically, a decay can be collected in about 10 minutes or less.

The overall time resolution of the above system is limited by the response time of currently available photomultipliers. Two different

photomultipliers were used in this work. One, a Varian VPM159A3, has an instrumental half width in response to a train of modelocked pulses of ~250 ps whereas the other, a Hammamatsu R1294U-01, has an instrumental width of ~130 ps. The Hammamatsu tube has a long wavelength cutoff around 800 nm and thus could not be used for the Si and GaAs work. The Varian tube on the other hand, has a long wavelength cutoff around 1.2 μm as well as greater dynamic range and lower dark count. If the observed lifetime is of the same order of magnitude as the instrument response one must remember that the observed decay is the convolution of the true luminescence decay with the instrument response. The true lifetime of the luminescence can then still be extracted with a deconvolution procedure. This is the subject of appendix 3. With deconvolution, lifetimes as short as 30 ps with the Hammamatsu tube, and 100 ps with the Varian tube, can be reliably extracted.

Better time resolution is possible with a streak camera [2.11-2.13], but with reduced sensitivity and dynamic range. The described instrumentation, with its high sensitivity and adequate time resolution, is optimum for studying exciton phenomena in semiconductors.

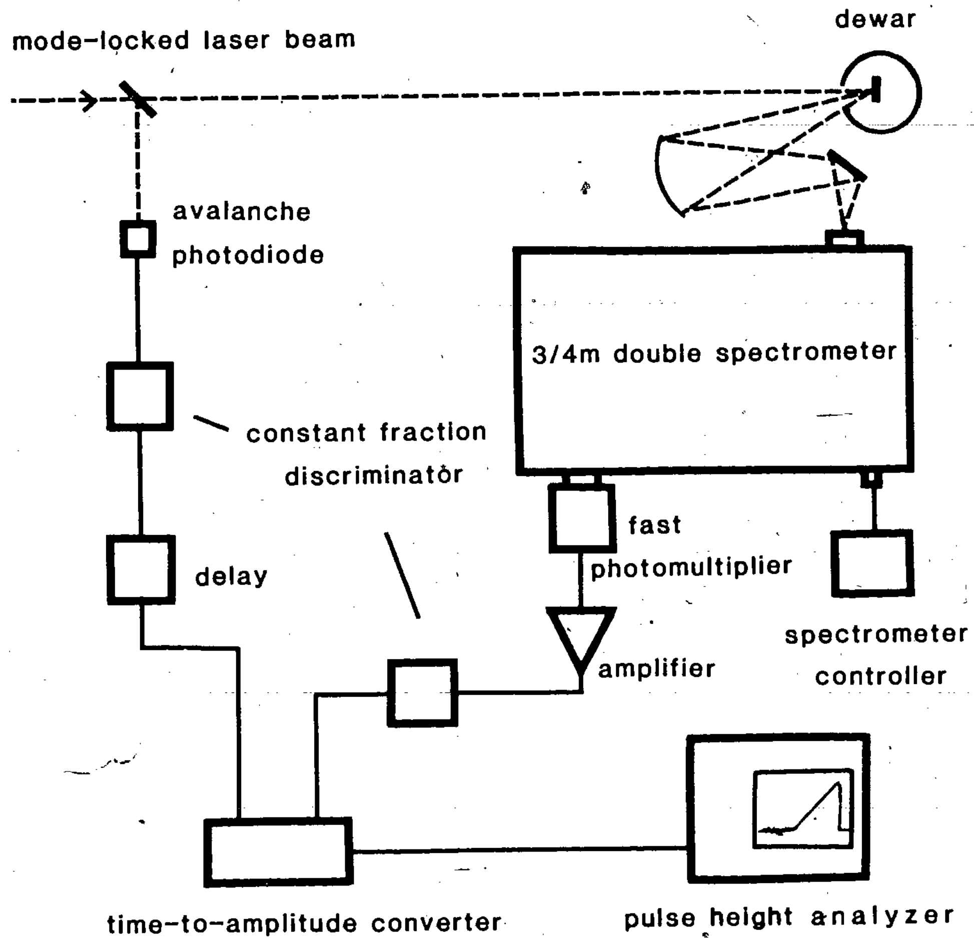

Figure 2.3

Block diagram of the delayed coincidence photon counting system

2.7 DATA ACQUISITION

The time correlated photon counting technique results in a histogram of the luminescence decay at the wavelength of the spectrometer. It would be desirable to have whole spectra corresponding to different time windows. Such a set of spectra shows the evolution of the spectral features with time. This is particularly useful if the wavelength peak of a luminescence feature shifts with time, such as with a DAP band. Such a set of spectra is also useful for locating replicas of the principal transitions, which must all decay at the same rate. By operating the whole data collection system under computer control, the collection of a set of time-resolved spectra can be realized. The computer collects a histogram of the luminescence decay at a given wavelength for a timed interval. The total number of counts in all the histogrammer channels corresponding to software-set time windows are summed, and each sum is stored separately in a page of memory. After this task is accomplished, the histogrammer is cleared and the spectrometer advanced to the next wavelength location. With the present software, up to 8 time windows can be set and thus, up to 8 time-resolved spectra can be collected simultaneously. The scan can be repeated an arbitrary number of times and the result averaged. Since all spectra are collected at once, rather than sequentially, there is no chance of a change in experimental conditions for spectra corresponding to different time windows. A schematic of the computer system is shown in figure 2.4.

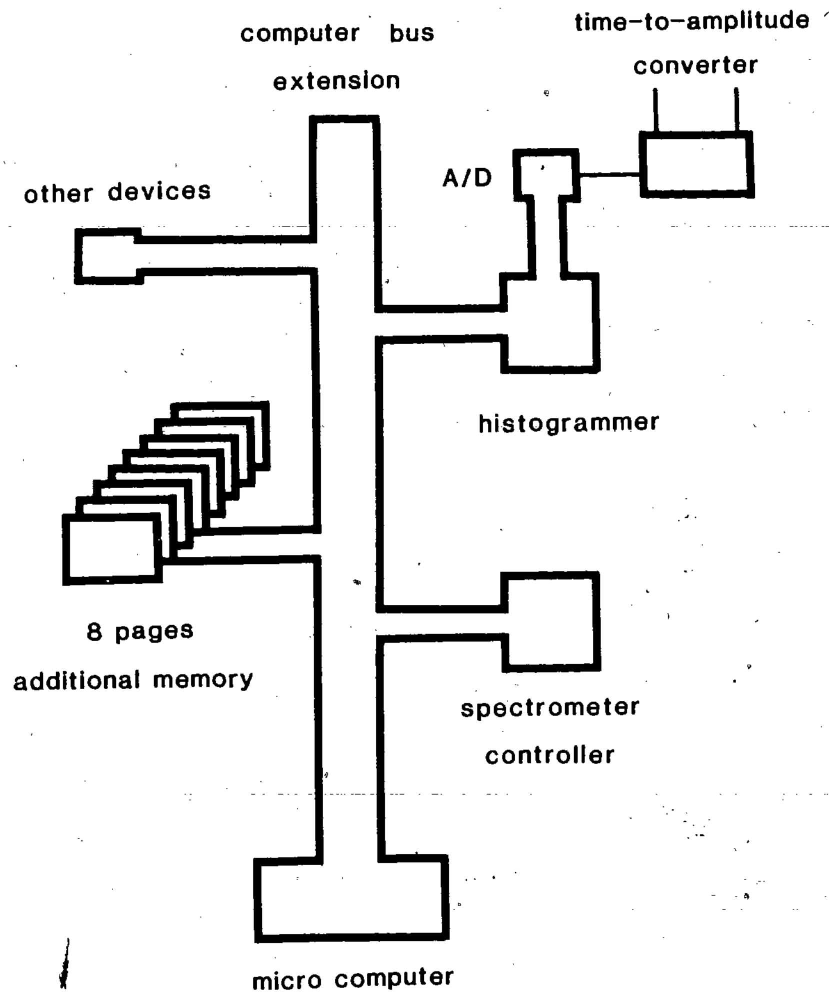

Figure 2.4

Block diagram of computer used for experimental control and data acquisition. During time-resolved spectroscopy each of the indicated pages of memory contains a spectrum corresponding to a different time window.

2.8 DETERMINING THE LASER PULSE WIDTH

The delayed coincidence photon counting data acquisition method of section 2.6 in conjunction with the presently available photomultiplier tubes does not have sufficient time resolution to determine the laser pulse width. To determine the pulse width directly a streak camera is needed, but lacking that, the pulse width can still be determined with an indirect, non-linear technique [2.30,2.31] based on second harmonic generation [2.32]. A block diagram of the necessary apparatus is shown in figure 2.5. The laser pulse is split into two equal pulses by a beam splitter. These pulses then travel down the arms of an interferometer, one arm of which is of variable length. The pulses are then recombined at the beam splitter and sent through a non-linear crystal. The resultant second harmonic ultra-violet (UV) light pulse is sent through a UV pass visible cut filter and the intensity of the UV is detected by a photomultiplier tube. The amount of UV generated depends on the spatial overlap of the pulses inside the non-linear crystal. An autocorrelation trace can be formed by periodically varying the path length of the variable interferometer arm and displaying the resultant UV intensity on an oscilloscope. The resultant trace is an average of a very large number of laser pulses with a slowly varying overlap. The intensity of the the second harmonic generated by the two equal amplitude pulses is proportional to the time average of the fourth power of the electric field inside the non-linear crystal [2.31]

$$I(2\omega,\tau) \propto \left\langle \int_{-\infty}^{+\infty} (E(\omega,t)^2 \sin^2 \omega t)(E(\omega,t+\tau)\sin^2 \omega(t+\tau))d\tau \right\rangle \qquad 2.16$$

Here the quantity $E(\omega,t)^2 = I(\omega,t)$ is the intensity of one of the input pulses at the fundamental frequency. $\tau = c/\Delta L$ is the time difference in arrival of the two pulses at the non-linear crystal due to a path difference ΔL in the interferometer. The triangular brackets signify a time average long compared to the pulse duration and repetition rate of the laser but short compared to the rate of change of τ. With the aid of trigonometric identities equation 2.16 can be written as

$$I(2\omega,\tau) \propto G^2(0) + 2G^2(\tau) + R(\tau) \qquad 2.17$$

where $R(\tau)$ contains very rapidly varying terms corresponding to the interference fringes. This term is not observed in experiment [2.31] and can be ignored. The autocorrelation function $G^2(\tau)$ is given by

$$G^2(\tau) = \langle I(t)I(t+\tau) \rangle \qquad 2.18$$

$G^2(\infty) = 0$ for pulses, thus from equation 2.17 the contrast ratio, $I(2\omega,0):I(2\omega,\infty)$, is easily seen to equal 3:1. The width of the autocorrelation trace is approximately equal to the time width of the laser pulse. The actual relationship is determined by the pulse shape

[2.30], but for practically desired accuracies can be taken as one. The autocorrelation trace is useful for determining the extent of modelocking. Two traces are shown in figure 2.6, a) represents an incompletely modelocked pulse train and b) a completely modelocked pulse train. The large spike in the middle of figure 2.6a corresponds to exactly zero path difference, where all the noise fluctuations are spatially superimposed in the non-linear crystal, leading to an anomalously large UV output. In a completely modelocked pulse train these noise fluctuations caused by randomly varying phases are absent since all the phases are locked, (section 2.2) and this coherence spike is therefore not observed.

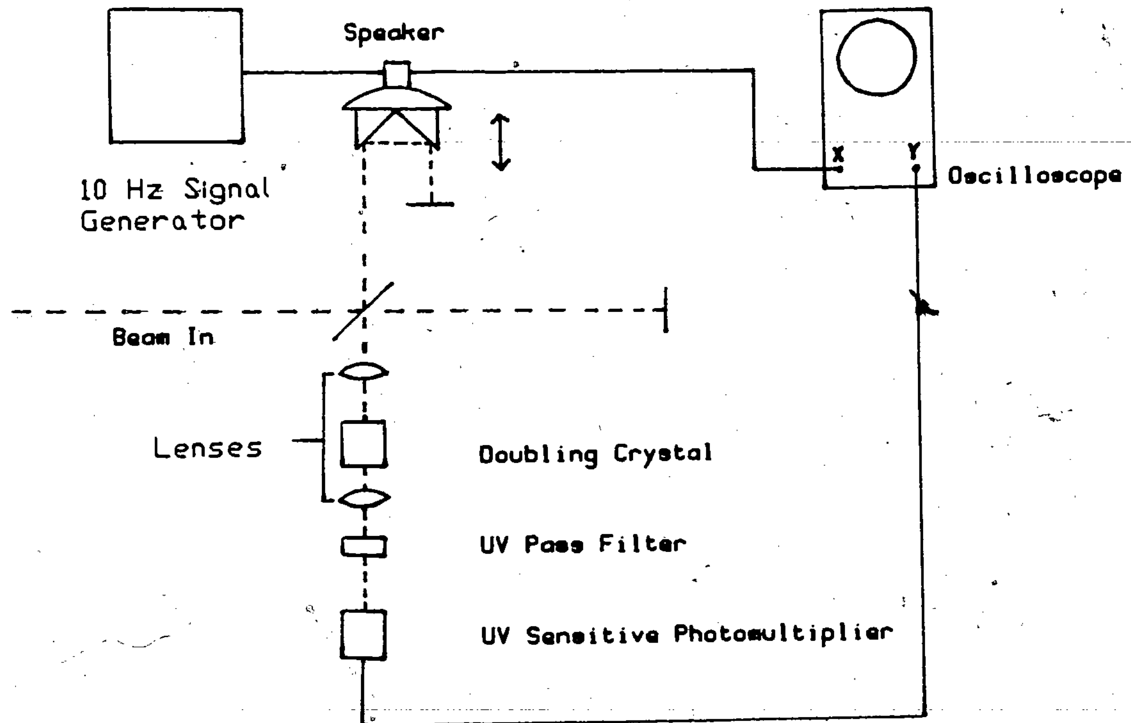

Figure 2.5

Block diagram of the autocorrelator used to determine the laser pulse width. The path length of one arm of the interferometer is varied periodically by a retro-reflector mounted on a high compliance speaker.

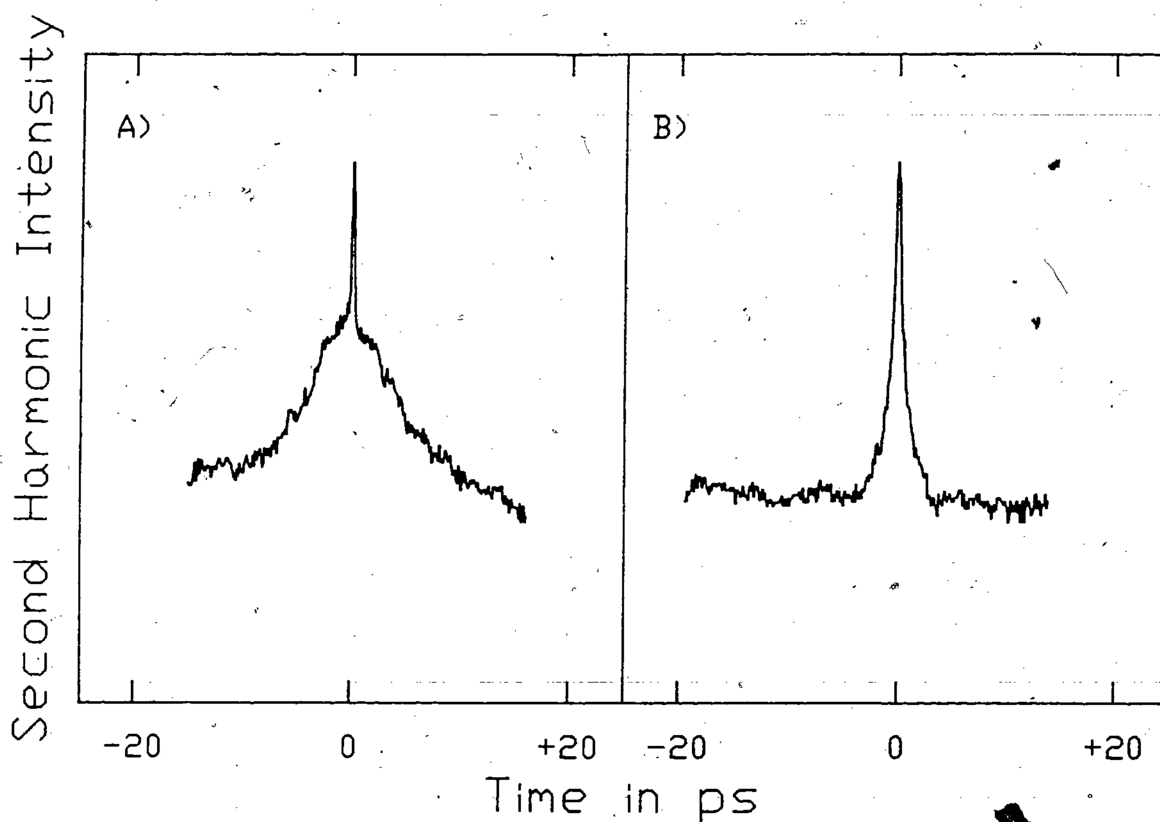

Figure 2.6

Examples of autocorrelation traces obtained using the system depicted in figure 2.5. The trace in A) corresponds to an incompletely modelocked laser with an autocorrelation trace width of ~10ps FWHM whereas B) is the ~1ps FWHM autocorrelation trace obtained from a fully modelocked laser.

3 DECAY OF BE IN Si

3.1 INTRODUCTION

Silicon is an indirect-gap semiconductor, and should according to the discussion in chapter 1 have its BE decay rates dominated by the non-radiative Auger mechanism (section 1.4). The experimentally observed luminescence decay rates are thus indicative of the Auger rates. A number of studies of Auger processes in silicon have been undertaken, both experimental and theoretical [3.1-3.3]. These studies are in good agreement and show a rapid decrease in BE lifetime with increasing binding energy. This can be qualitatively understood in terms of a greater spread in K-space for the more localized excitons, resulting in a larger overlap with possible free particle final states and hence, a larger Auger decay rate. Schmid [3.1] has deduced an empirical power law relationship between binding energy and Auger decay rates of BE in Si. For acceptor BE,

$$\tau_A \propto E_A^{-4.5} \qquad 3.1$$

and for donor BE

$$\tau_D \propto E_D^{-3.9} \qquad 3.2$$

where E_A and E_D are the acceptor and donor binding energies, respectively. The agreement with the -4.0 exponent derived for a crude BE model in section 1.4 is quite remarkable.

Recently it has been suggested that the effective mass approximation (section 1.1) underlying the theoretical calculations of the BE lifetimes should break down for deep centers [3.4]. This would lead to much longer BE lifetimes than would be expected from direct extrapolation by means of equations 3.1 and 3.2 from the results for shallower centers. This prompted the measurement, for the first time, of the BE decay times for Tl and Bi, respectively the deepest simple acceptor and donor in Si. For the 246 meV deep Tl acceptor, extrapolating from In (154 meV), using relation 3.1, and an In BE lifetime of 2.4 ns yields an expected BE lifetime of 280 ps. On the basis of the measured Tl oscillator strength and luminescence efficiency (section 1.2 and 1.4) the Tl Auger decay rate had previously been estimated to lie between 75-300 ps [3.5]. The measured result is 270 ± 50 ps, in good agreement with both of these predictions. Thus the effects predicted by Jaros et. al. [3.4] are apparently not important for the Tl BE.

Using a value for the Bi binding energy of 69 meV [3.6] and relation 3.2 to extrapolate from As (BE lifetime = 183 ns, donor binding energy = 53 meV) [3.1] results in an expected Bi BE lifetime of ~60 ns. The measured lifetime was, however, only 8.6 ns, 7 times shorter than expected indicating that the simple theory of Dean (section 1.4) leading to equation 3.2 is not entirely applicable for deep donors in Si.

3.2 EXCITON KINETICS

Neglecting saturation effects, meaning that the number of bare binding centers is negligibly affected by the free exciton (FE) concentration, the FE decay is give by

$$\frac{dn_{FE}}{dt} = -\frac{n_{FE}}{\tau_o} - \frac{n_{FE}}{\tau_{FE}} \qquad 3.3$$

where n_{FE} is the FE concentration and $1/\tau_{FE}$ is the FE capture rate by the impurities. τ_o is the radiative decay rate of free excitons which is of the order of ms in Si [3.7]. The free exciton capture rate on the other hand is very fast, on the order of ns, even for lightly doped samples (10^{15} impurities per cm^3). The radiative term in 3.3 is thus totally negligible in comparison to the capture term. Equation 3.3 thus simplifies to

$$\frac{dn_{FE}}{dt} = -\frac{n_{FE}}{\tau_{FE}} \qquad 3.4$$

The BE concentration, n_{BE} is similarly given by

$$\frac{dn_{BE}}{dt} = K\frac{n_{FE}}{\tau_{FE}} - \frac{n_{BE}}{\tau_{BE}} \qquad 3.5$$

where $1/\tau_{BE}$ is the decay rate for the BE and K is a constant factor

less than unity which reflects that the particular BE of interest may not be the only available decay channel for the FE, i.e. there could be other impurities which bind excitons. Since the sample temperature is very low (T < 4.2K) and the exciton localization energy is greater than several meV, a term corresponding to thermal evaporation [3.7] of BE need not be included. The set of equations 3.4 and 3.5 can be written in matrix form as

$$\nabla_t \underline{n} = \begin{pmatrix} -1/\tau_{FE} & 0 \\ K/\tau_{FE} & 1/\tau_{BE} \end{pmatrix} \underline{n} \qquad 3.6$$

The general solution is of the form [3.8]

$$\underline{n}(t) = \underline{m}\exp(rt) \qquad 3.7$$

where r and the constant vector $\underline{m}$ have to be determined. Substituting this into equation 3.6 and dividing out the exponential term yields the algebraic equation

$$\begin{pmatrix} -1/\tau_{FE}-r & 0 \\ K/\tau_{FE} & 1/\tau_{BE}-r \end{pmatrix} \underline{m} = 0 \qquad 3.8$$

The eigenvalues, r, are found from the secular equation obtained by setting the determinant of the coefficient matrix equal to zero yielding

$$r_1 = -1/\tau_{FE} \quad \& \quad r_2 = -1/\tau_{BE} \tag{3.9}$$

The eigenvectors, found by substituting the above eigenvalues in equation 3.8 are

$$\underline{m}_1 = \begin{pmatrix} \tau_{FE}/\tau_{BE} - 1 \\ K \end{pmatrix} \quad \& \quad \underline{m}_2 = \begin{pmatrix} 0 \\ 1 \end{pmatrix} \tag{3.10}$$

The general solution of equation 3.6 is thus

$$\underline{n} = c_1\underline{m}_1\exp(r_1t) + c_2\underline{m}_2\exp(r_2t) \tag{3.11}$$

At $t=0$ $\underline{n} = (n_{FE}(0)\ 0)$ and hence the constants c are determined to be

$$c_2 = -Kc_1 = Kn_{FE}(0)\,\frac{\tau_{BE}}{\tau_{BE} - \tau_{FE}} \tag{3.12}$$

Writing the general solution equation 3.11 in scalar form and substituting in the above values for the constants c results in

$$n_{FE}(t) = n_{FE}(0)\exp(-t/\tau_{FE}) \tag{3.13}$$

for the FE population and

$$n_{BE}(t) = Kn_{FE}(0)\ \frac{\tau_{BE}}{\tau_{BE} - \tau_{FE}}\ [\exp(-t/\tau_{BE})-\exp(-t/\tau_{FE})] \qquad 3.14$$

for the BE population. The BE luminescence intensity, which is proportional to the number of BE is thus of the form

$$I_{BE} \propto \exp(-t/\tau_d) - \exp(-t/\tau_r) \qquad 3.15$$

Here τ_d, the decay time constant, is the longer of τ_{FE} and τ_{BE}, and τ_r, the rise time constant, is the shorter. Thus if the sample is heavily doped, resulting in a very short FE trapping time, the measured luminescence decay will correspond to the BE lifetime. In this case the luminescence rise time constant will correspond to the FE lifetime. If, on the other hand, the impurity concentration is relatively light, the FE trapping time may well be longer than the BE lifetime. In this case the luminescence rise time constant will correspond to the BE lifetime and the luminescence decay time to the FE lifetime. In a lightly doped sample, high excitation densities may saturate the FE decay channels, in which case the rise and fall of the luminescence will no longer be described by simple exponentials. Nevertheless, the picture remains qualitatively the same with the rise time related to the BE decay time and the fall corresponding to the

decay of the FE population. This situation can usually be recognized by a non-exponential decay curve as well as by an excitation density dependence of the photoluminescence decay curve characteristics.

3.3 EXPERIMENTAL RESULTS FOR THE Tl,In AND Bi BE IN Si

The measurements were done using the cavity dumped, modelocked dye laser described in chapter 2 operating at 600 nm with a 4 Mhz repetition rate and a <10 ps pulse width as an excitation source. The samples were mounted in a liquid He immersion cryostat allowing observations at temperatures between 1.8 and 4.2k. The luminescence was detected using a fast photomultiplier (Varian VPM-159A3) operating in a photon counting mode as discussed in section 2.6.

The temporal instrument response was found to be wavelength dependent, with the response time lengthening as the long wavelength cutoff of the photomultiplier is reached. At wavelengths corresponding to near gap luminescence in Si, the response time of the Varian photomultiplier used here is considerably longer than the temporal response to visible optical pulses quoted in section 2.6. The response time of the photomultiplier at the Tl BE wavelength was experimentally determined by parametrically generating photons [3.9-3.11] at the Tl wavelength from the 600 nm modelocked pulse train, using a nonlinear crystal. The total system response was thus determined to have a risetime of 70 ps, a FWHM of about 500 ps and an exponential tail with a fall time constant of 530 ps at the wavelength of Tl BE (1.116 μm). Hence, in order to interpret the Tl data the measured BE decay curve must be deconvoluted with this measured 1.116 μm instrumental response to obtain the true BE transient behaviour as discussed in appendix 3. In the case of the In and Bi BE deconvolution was unnecessary since these lifetimes were found to be considerably longer than the system

response, and hence would be negligibly affected by deconvolution.

Observations of the transient photoluminescence of 2 different Tl doped Si samples illustrates both possible cases of relative BE and FE lifetimes. Figure 3.1a was obtained from a relatively lightly doped sample. Here the decay is slightly non-exponential and intensity dependent, indicating that some saturation is occurring. By fitting a solution of the form of equation 3.5 to the rise and initial decay, the Tl BE decay time constant is determined to be 290 ps. The curve in Figure 3.1b is from a more heavily doped Tl sample. It shows an exponential, pump power independent decay, indicating that saturation effects are negligible. Fitting a solution of the form of equation 3.15 to the data using the deconvolution program results in a rise of 260 ps and a fall of 270 ps. Interpreting the fall as the BE decay gives a lifetime of 270 ps for the Tl BE in good agreement with that obtained from the rise in Figure 3.1a. Reasonable fits could be obtained over a region of τ_d = 270 ± 50 ps, with suitably adjusted rise times. This rather large uncertainty occurs because the system fall time at 1.116 µm is only slightly faster than that of the luminescence. There was no observed temperature dependence of the lifetimes between 1.8 and 4.2 K. This first direct measurement of the Tl BE decay rate is thus in good agreement with an extrapolation from the known results for shallower acceptors, as well as falling within the range expected from oscillator strength and luminescence efficiency measurements [3.5].

For the In data the BE recombination time was determined by a straight line fit to the log of the luminescence decay at 1.0864 um.

Figure 3.2 shows the results from 3 different samples of different doping concentrations ranging from 4×10^{16} cm^{-3} (Figure 3.2a) to 2×10^{17} cm^{-3}(figure 3.2b) to 5×10^{17} cm^{-3} (Figure 3.2c). There was no observed temperature dependence in the 1.8 to 4.2 K range, and no pump power dependence over a wide range of pump powers. These results seem to indicate a slight dependence of the Auger rate on the impurity concentration. The above results agree reasonable well with that of Schmid [3.1], who obtained 2.7 ns.

This is believed to be the first measurement of the Bi BE lifetime. On the basis of relation 3.2 the expected BE lifetime is 60 ns. The measured lifetime at 1.0806 μm was 8.6 ns (figure 3.3), considerably shorter than the predicted value. Again there was no observed temperature dependence or pump power dependence.

Concluding the Si work, the Tl BE lifetime was determined to be close to the anticipated value showing that the effects predicted by Jaros et. al. [3.4] do not occur even for the deepest simple acceptor in Si. The In results were in reasonable agreement with a previous measurement and showed a slight concentration dependence. The Bi BE lifetime was found to be much shorter than anticipated on the basis of extrapolation from shallower donors indicating that the simple theory of section 1.4 is not applicable for some as yet unexplained reason.

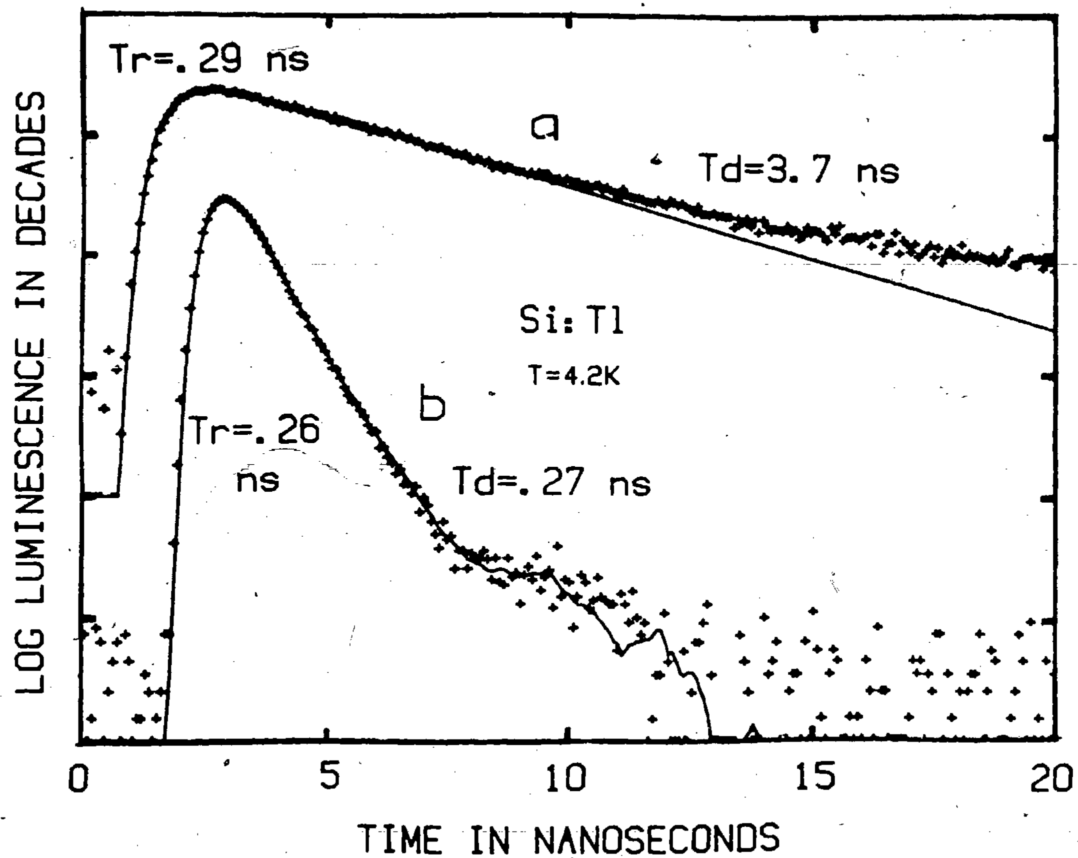

Figure 3.1

Time resolved luminescence from the Tl BE at 1.116 µm. The + are the experimental points. The solid line is the best fit using the indicated rise and fall times in equation 3.15 and convoluting with the instrument response. The vertical markers represent decades of intensity.

a) 4×10^{14} Tl cm^{-3}

b) $\sim10^{17}$ Tl cm^{-3}

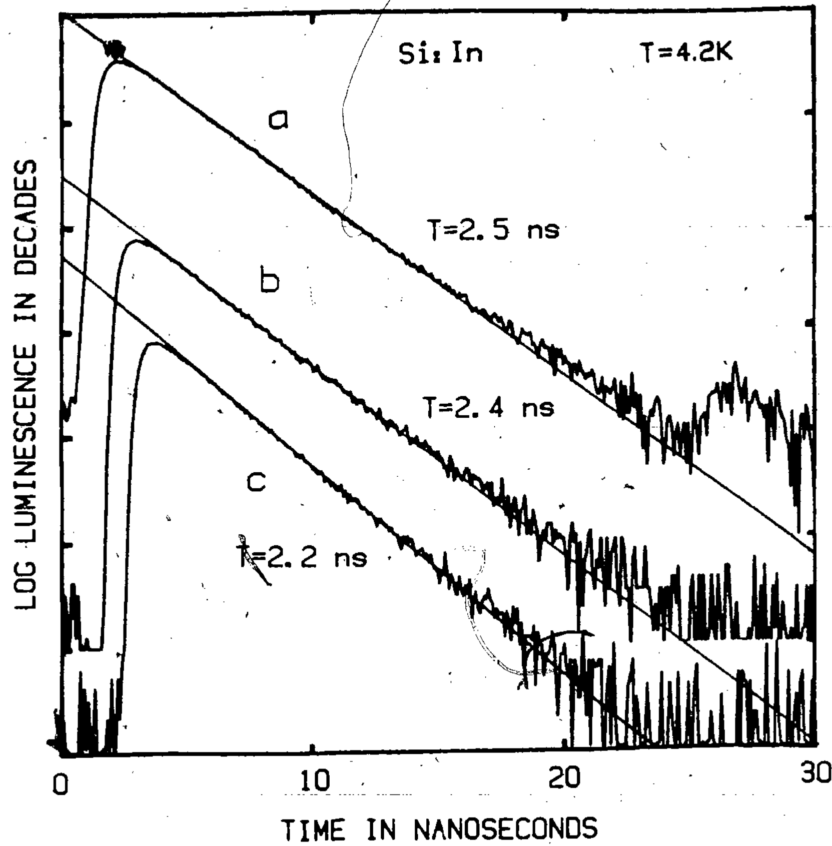

Figure 3.2

Luminescence decay of the In BE. The straight lines are least squares fits to the data yielding the indicated lifetimes. The vertical markers represent decades of intensity.

a) 4×10^{16} In cm^{-3} sample

b) 2×10^{17} In cm^{-3} sample

c) 5×10^{17} In cm^{-3} sample

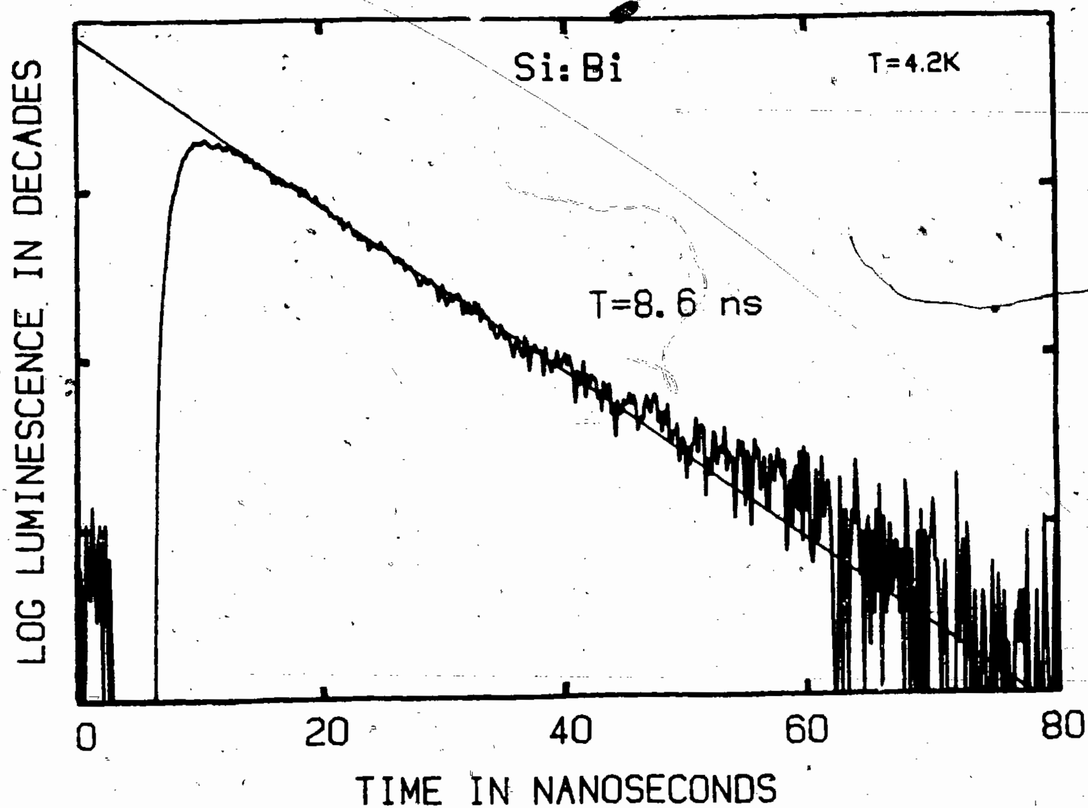

Figure 3.3

Luminescence decay of the Bi BE. The straight line is a least squares fit to the data yielding a lifetime of 8.6 ns. The vertical markers represent decades of intensity.

4 TRANSIENT STUDIES OF EXCITON LUMINESCENCE IN CdSe

4.1 INTRODUCTION

The photoluminescence spectrum of weakly excited (eg. in the region where stimulated emission and exciton-exciton interactions are unimportant) CdSe has been extensively studied over the last 20 years [4.1-4.5] and was found to be in general agreement with the model put forward by Thomas and Hopfield [4.6] to explain the photoluminescence of the similar direct-gap material CdS. The spectrum consists of intrinsic polariton luminescence, and at lower energies the unresolved luminescence from excitons bound to neutral donors (I2 line) and acceptors (I1 line), plus the various replicas of these lines.

The lifetime of the I2 line in CdS was first determined by the phase shift method [4.7] (section 2.1), which relies on the assumption that the decays are strictly exponential and that the build up is very fast. More recently the I2 and I1 lifetimes in CdS have been directly determined, using a modelocked laser source and a fast photomultiplier tube detector, to be 0.6 and 1.0 ns respectively [4.8]. Jorgensen and Hvam attempted to measure the I2 and polariton lifetimes in CdSe by an indirect technique utilizing the non-linearity of the luminescence intensity with respect to excitation power [4.9]. They obtained results which suggested that the luminescence decay of I2 was much faster than that of the polaritons. This led them to conclude that the capture of polaritons by the neutral donors to form donor BE is insignificant at low excitation and hence that polariton capture by

neutral donors was not the dominant method of BE formation or of polariton decay in CdSe. This seemed a very suspect conclusion, particularly as direct lifetime measurement [4.8] and excitation spectroscopy [4.10] in CdS had shown the contrary to be the case in this very similar material. This prompted the first direct measurement of the lifetimes of the BE and polaritons in CdSe using both above band-gap and resonant excitation on samples obtained from the same source [4.11] as those used by Jorgensen and Hvam. These samples where thin platelets with the c-axis in the plane of the crystal. No information about the impurity content of these crystals was available.

With resonant excitation of the I1 line a replica of I1 was observed which is believed to be a two-hole transition (section 1.5). This fixes the binding energy of the neutral acceptor responsible for the I1 line in this sample at considerably less than that of either the Na or Li acceptor values reported earlier [4.2]. This is believed to be the first two-hole BE transition to be observed in a II-VI wurtzite semiconductor.

In this CdSe sample two distinct peaks in the intrinsic polariton region of the spectrum were observed. These seemed to have very different coupling strengths to LO phonons, as well as slightly different decay characteristics. This, together with the 2 meV splitting between the peaks, suggests that they originate from different polariton branches. The origin of similar splittings observed in the polariton spectrum of most other direct-gap semiconductors is the subject of considerable dispute (chapter 7).

One of the interesting results of the transient measurements was the observation that the polariton and donor and acceptor BE decay times were strongly dependent upon the excitation intensity even in the very low-power limit, even though at any given power level the observed decays appeared to be single-exponential to a very good approximation. This may indicate that even in these high quality samples, the donor and acceptor concentrations are so high that inter-impurity tunnelling is substantial. It would appear that the usual assumption of well-defined lifetimes for particular excitonic species in the 'low-power regime' requires careful scrutiny in this and similar direct-gap materials.

4.2 EXPERIMENTAL APPARATUS

The excitation source used in this experiment was the modelocked synchronously pumped, cavity dumped dye laser system described in chapter 2. The laser dye LD688 (available from Exciton) provided a tuning range of approximately 660-720 nm, covering the entire region of interest. Rhodamine 6G was also used for some of the above band-gap excitation experiments. The pulse width as determined by the autocorrelator (section 2.8) was less than 30 ps, and the repetition rate was in most cases 4 MHz. Due to the inadequacies of the tuning element, the spectral line width of the laser pulses proved in some cases to be much too wide for selective excitation experiments, necessitating the use of 3/4 m Spex monochromator to narrow the laser line sufficiently (<1 meV FWHM).

The CdSe platelets with the c-axis in the plane were mounted in a strain free manner and immersed in ~1.5 K liquid He. The luminescence was detected by a second 3/4 m Spex monochromator coupled to a very fast microchannel plate photomultiplier (Hammamatsu R1294U-01) cooled to -30 C. The time-resolved spectra were collected by the data acquisition system described in section 2.7. The total system response to the dye laser excitation pulses in this wavelength region is depicted in figure 4.3e.

The spectral scans were done using a different detector (Varian VPM 159A3) with a much lower dark count and larger dynamic range, connected to a double 3/4 m Spex monochromator operated at a spectral resolution of about 0.2 meV.

4.3 CW PHOTOLUMINESCENCE SPECTRA OF CdSe

A low-power continuous-excitation photoluminescence spectrum typical of our CdSe samples is shown in figure 4.1. I2 & I1 are the neutral donor and acceptor BE lines, respectively. The lines α, β, γ, δ collectively labeled I2-2e are the so called two-electron transitions (section 1.5) of the neutral donor BE, or of the excited exciton states thereof [4.3,4.4]. The 1 and 2-LO phonon replicas of I2 and I1 are also clearly visible. The low energy band labeled DAP is the donor-acceptor pair recombination band [4.1]. The LO phonon energy can be accurately determined to be 26.4 ± 0.2 meV from the positions of the sharp BE and BE-LO replicas. The polariton peaks in these CdSe samples are much closer to I2 than those in a previously published spectrum [4.4]. The location of the polariton peaks seems to be sample dependent in CdSe [4.12] for some as yet unexplained reason.

The peaks A1 and A2 are both from polariton luminescence as verified by their intensities relative to the BE with increasing temperature (figure 4.2). Had A2 been due to a localized state, its intensity relative to the polaritons would have decreased at higher sample temperatures. The polariton nature of A1 and A2 has also been verified by recording a reflection spectrum, which shows sharp structure at exactly the same energies seen in luminescence. In their study of transient behavior in CdSe, Hvam and Jorgensen [4.9] did not resolve the no-phonon polariton lines, nor the fine structure in the LO phonon replica energy region evident in figure 4.1. The line they label A_1-LO in their figure 2 would seem to consist mostly of

unresolved BE LO replicas.

The low energy dashed line on the spectra in figure 4.2 indicates the extrapolated, sharp, low energy edge of the polariton 1-LO phonon replica. The second dashed line has been drawn exactly 1 LO phonon energy (26.4 meV) above the first. This higher energy dashed line falls right in between the A1 and A2 peaks seemingly indicating that the low energy edge of the LO replica originates from the population of polaritons responsible for the low energy edge of the A1 peak. This is however not the case. Toyozawa [4.13] showed that the strength of the coupling between an exciton and the 1-LO replica should vary as q^2 for small phonon wavevectors q. This means that the lower polariton branch (A2) should couple more effectively to LO phonons. This result has been verified in CdSe by resonant Brillouin scattering [4.14]. The apparent contradiction of the present experimental results with these conclusions can be reconciled by realizing that the above mentioned extrapolation to determine the low energy edge of the 1-LO replica is invalid for polaritons. A glance at the polariton dispersion curve (figure 1.1) shows that unlike a regular free exciton the lower polariton branch curves in such a way that the wavevector changes very little for a relatively large change in energy below the knee in the dispersion curve. This has the effect of adding a curved tail to the 1-LO phonon replica as seen in figure 4.2. This means that the observed 1-LO phonon replica can in fact originate from the lower polariton branch.

Since the splitting between the upper and lower polariton branches in CdSe has been determined to be ~.5 meV by resonant

Brillouin scattering [4.14], the experimental result that the two polariton peaks are separated by 2 meV seems incompatible with an explanation of the high energy polariton peak A1 in terms of a maximum in the transmission of the crystal surface as has been suggested for CdS [4.8,4.12,4.15]. This result instead suggests that these peaks arise from the two different branches of the polaritons: A1 from the upper polariton branch and A2 from the lower. Further support for this suggestion is the observation that the measured photoluminescence decays of A1 and A2 (figure 4.4) are slightly different. The A1 decay shows a stronger fast component as well as having a slightly shorter overall decay time. There was, however, no observed wavelength dependence of the decay characteristics within each peak A1 or A2. The decay changes from 'A1 type' to 'A2 type' quite suddenly upon changing the energy of observation from 1826 meV to 1825 meV. If both A1 and A2 arose from the same polariton branch the decay characteristics would be expected to vary continuously over both lines since the more rapid decay of the A1 peak would then have to be interpreted as the cooling of these higher energy polaritons.

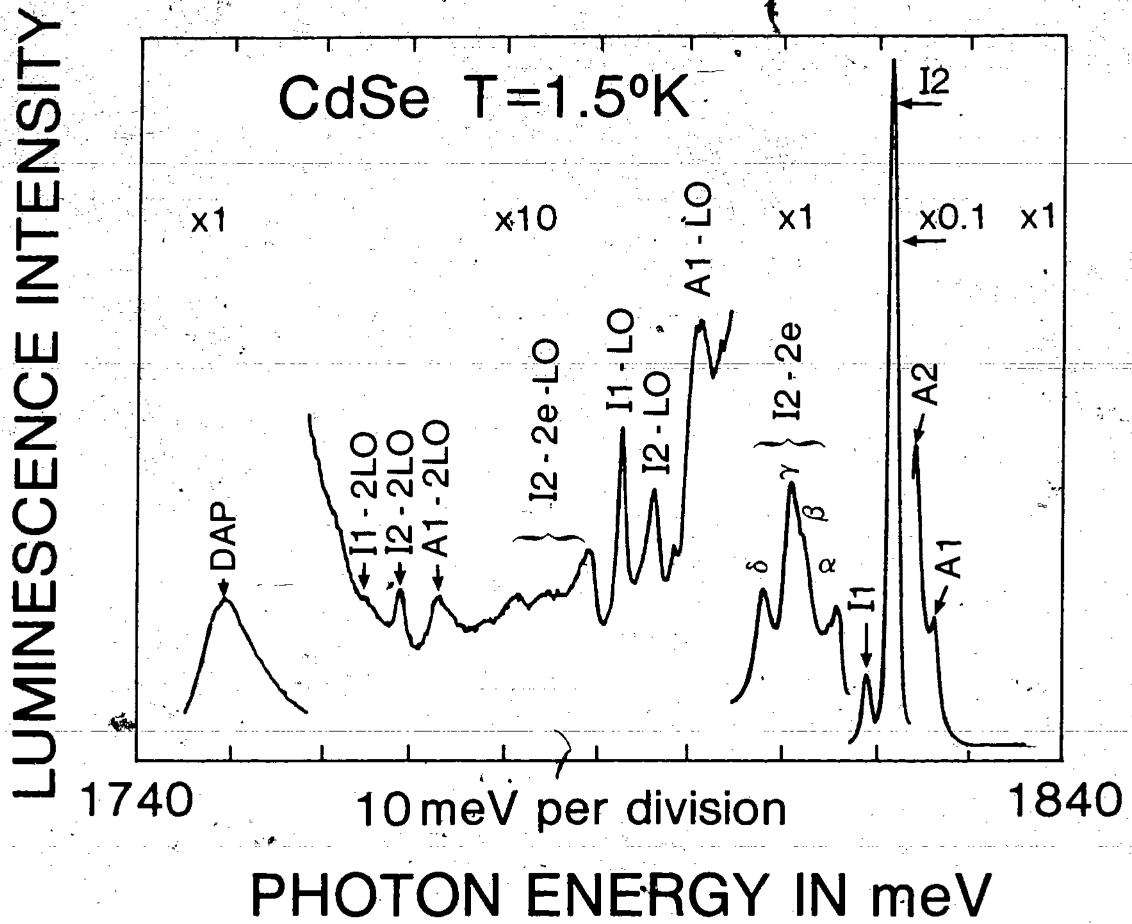

Figure 4.1

Photoluminescence spectrum of CdSe at 1.5 K with ~100 mW/cm² of above band-gap excitation light at 590 nm.

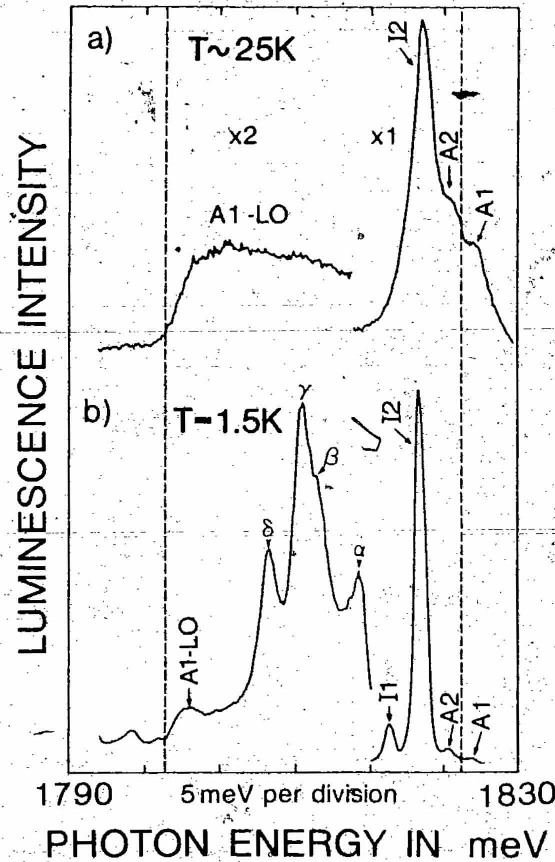

Figure 4.2

A portion of the photoluminescence spectrum at higher temperature T ~ 25K a) and at T = 1.5K b). The lower energy dashed line represents the apparent low energy edge of the polariton LO replica. The higher energy dashed line is exactly one LO phonon energy (26.4 meV) above the lower line. The high temperature spectrum has been shifted up in energy by 2 meV to match the low temperature spectrum, in order to compensate for the temperature induced band-gap shift [4.5]. The ~25K sample temperature has been estimated from this shift, since the sample was freely mounted in He gas and its temperature could not be measured directly.

4.4 TRANSIENT CdSe PHOTOLUMINESCENCE RESULTS

Figure 4.3 shows the photoluminescence decay of the A1, A2, I2, and I1 lines at a fixed, average, above band-gap pump intensity of approximately 100 mW/cm² at a repetition rate of 4 MHz. The decay of the A1 and A2 polariton luminescence (figure 4.3 c & d) was non-exponential and faster than that of I2 (figure 4.3b) or I1 (figure 4.3a). Figure 4.3e shows the total instrument response to the 30 ps wide dye laser pulses. Surprisingly, the lifetimes of the I2 (figure 4.5) and I1 lines were found to depend strongly on pump intensity. This was found to be true even with resonant excitation of the BE, indicating that the lengthening of their lifetimes with increasing pump power is not merely due to saturation of the polariton capture rate. A sample heating effect can be ruled out since the observed lifetimes depend only on the peak pulse intensity and not on the average pump power. This was verified by lowering the repetition rate of the cavity dumper by a factor of 10, thus decreasing the average power by a factor of 10 while leaving the peak power almost unchanged. No change in the shape of the decay curves was observed.

With above band-gap excitation at high power levels, saturation of the recombination channels does play a role as evidenced by the substantial lengthening of the polariton lifetime (figure 4.4). In this above band-gap high excitation density regime the lifetimes of all of the lines increased substantially, in accordance with our expectation that under any given set of conditions the BE lines can never decay more rapidly than the polaritons. In obtaining the

different I2 lifetimes depicted in figure 4.4 the pump intensity was varied by a factor of 10^6. The highest excitation density used was ~10 W/cm^2 average, or a peak pump density of ~10^5 W/cm^2, and the lowest (corresponding to figure 4.5g) 10^{-5} W/cm^2 average. The only difference in the experimental conditions resulting in the decay curves of figure 4.5 was the insertion of various neutral density filters in the exciting laser beam. The focussing of the laser spot on the sample was not changed. For the higher excitation powers neutral density filters were placed in the luminescence path to keep the count rate low.

The reason for the observed behaviour is not clear. The donor and acceptor concentrations in these CdSe samples must be quite large, as evidenced by the strong DAP luminescence and the persistence of the I2 line at high temperatures, as seen in figure 4.2. It is possible that the large spatial extent of the BE wavefunctions and the close proximity of other defects leads to large variations in the lifetimes and to tunnelling between binding centers. There appears to be 2 distinct regions in the pump power dependence of the lifetimes. In the high power regime, beginning at ~100 mW/cm^2 average power at a 4 MHz repetition rate (figure 4.5d), where the lifetimes lengthen rapidly with increasing pump power, saturation of the polariton recombination rate appears to be the dominant factor. Below this region the lifetime of I2 varies more slowly with pump intensity and saturation is not involved. It must be stressed, however, that at all excitation densities at which both the polaritons and I2 were observable the lifetimes of the polaritons were always shorter than those of the BE.

As a result of this behaviour it is not possible to unequivocally state a donor BE lifetime for these samples. At low excitation densities the I2 lifetime asymptotically approaches a value of ~150 ps. It cannot be decided, however whether this is the true donor BE lifetime or the lifetime of some perturbed centers. In any measurement of the BE lifetimes in these materials the extent of any pump power dependence such as the one presented here should be investigated. Very recently Minami and Era [4.16] have presented the results of direct lifetime measurements of the I2 and I1 lines in CdSe using the same experimental method, which yielded the considerably longer lifetimes of 0.51 ns and 0.80 ns for I2 and I1 which were apparently excitation density independent. Since the lifetime of an exciton bound to an isolated center should not depend on the excitation density the above results indicate that the BE lifetimes observed here are representative of centers perturbed by nearby impurities whereas those observed by Minami and Era [4.16] in their apparently higher quality sample are the unperturbed lifetimes of isolated impurity BE.

The initial fast drop of the polariton luminescence shown in figure 4.4 c & d was due to the trapping of polaritons on binding centers until saturation was reached. This conclusion is supported by the observation that the buildup of the I2 luminescence (figure 4.4b) was not complete until the polaritons had reached their final decay rate. The initial fast drop of the I1 luminescence must be due to some superimposed, short lived luminescence of a different nature, as is evident in the time-resolved spectra of figure 4.6. These spectra also show the rapid buildup of I2 at the expense of the polaritons until

saturation was reached. The LO phonon replicas of the polaritons in these spectra show the initial rapid cooling of the polariton gas in the first nanosecond after the laser pulse [4.17]. A line shape analysis is not possible due to the presence of strong nearby BE luminescence. It might be thought that the initial fast drop in the no-phonon polariton luminescence could be due to this cooling. In this case, however one would expect the ratio of the fast to the slow component to vary with wavelength inside of a polariton peak with no fast component at the very low energy edge. In fact in this case the luminescence from the low energy edge corresponding to the lowest energy polaritons should show an observable buildup due to feeding from the hotter higher energy polaritons. There is however no observable change in the ratio with wavelength within one polariton no-phonon peak. Lastly, the intensity ratio of the fast to the slow components decreases with increasing pump power which agrees with expectation of the trapping model.

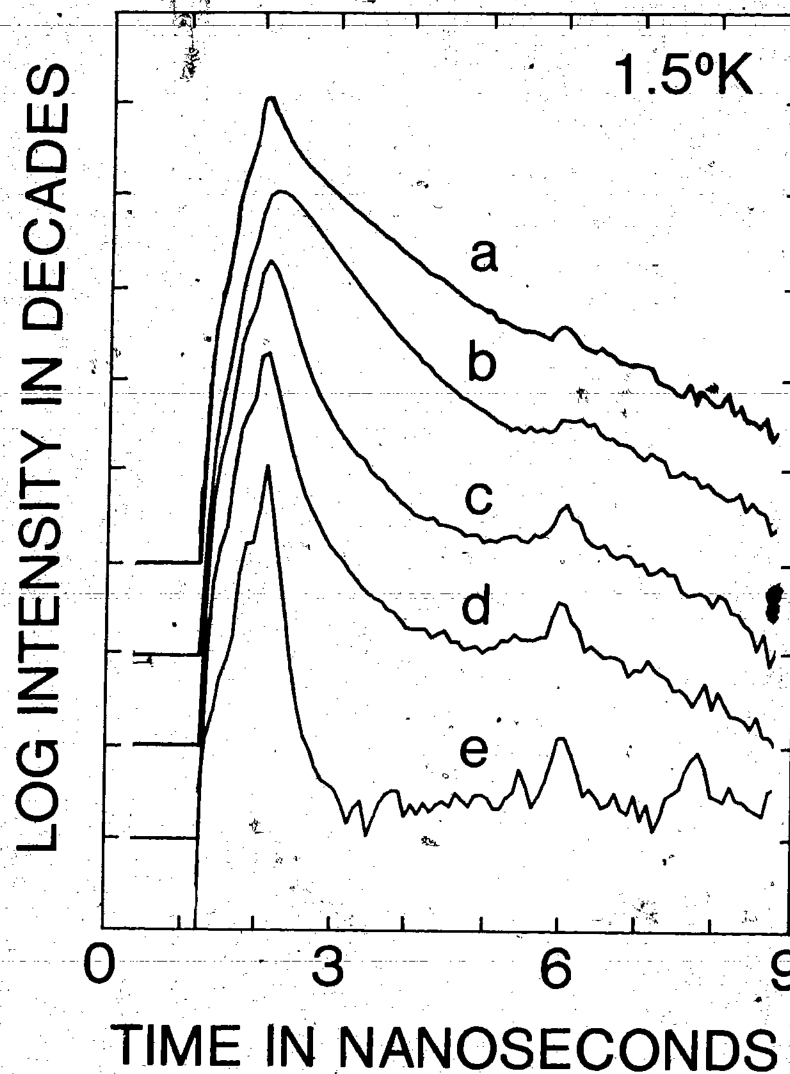

Figure 4.3

Luminescence decay of various lines with ~100 mW/cm² of above band-gap excitation at a 4 MHz repetition rate.

a) I1 line

b) I2 line

c) A2 polariton

d) A1 polariton

e) instrument response to < 30 ps wide laser pulses.

Each curves has been offset by one decade for clarity.

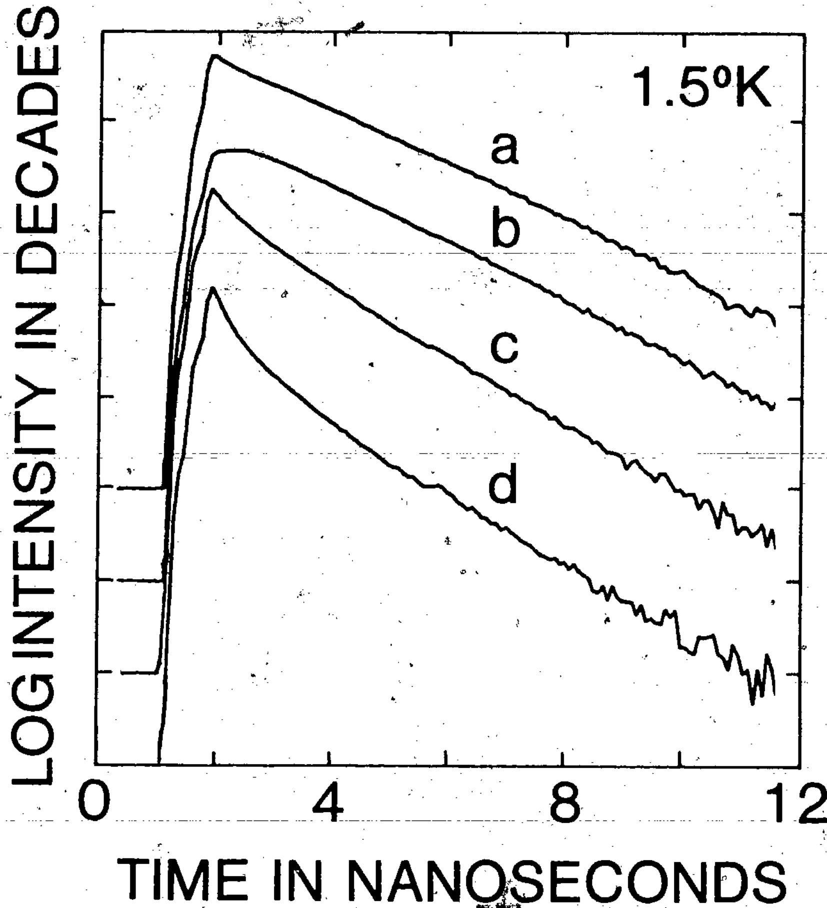

Figure 4.4

Luminescence decay of various lines with ~3 W/cm² of above band-gap excitation.

a) I1 line

b) I2 line

c) A2 polariton

d) A1 polariton

Each curve has been offset by one decade for clarity.

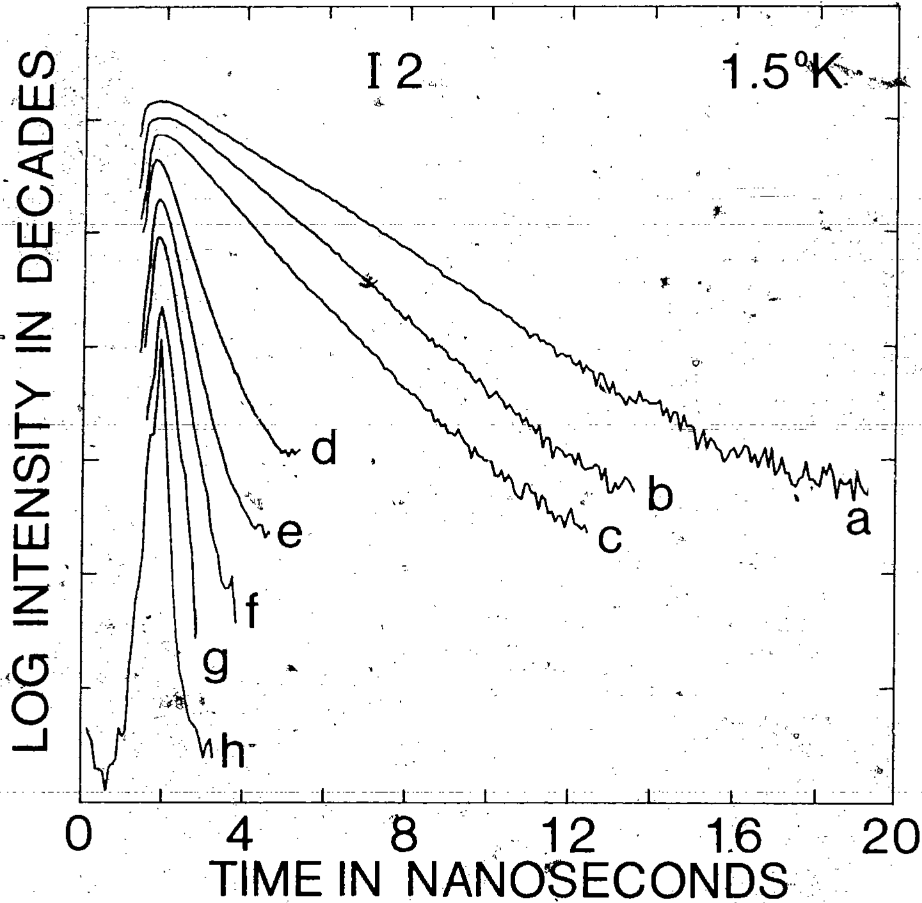

Figure 4.5

Luminescence decay of the I2 line with various excitation densities:

a) ~10 W/cm² b) ~3 W/cm² c) ~1 W/cm²

d) ~.1 W/cm² e) ~10^{-2} W/cm² f) ~10^{-3} W/cm²

g) ~10^{-5} W/cm² h) instrument response to < 30 ps wide laser pulses.

For clarity, the curves have been offset by arbitrary shifts.

4.5 RESONANT EXCITATION OF DONOR AND ACCEPTOR BE

With resonant excitation it is possible to determine unequivocally which lines are replicas of I2, I1 or the polaritons. This is very useful for identifying possible BE two-electron or two-hole transitions [4.18] (section 1.5). These are processes where the remaining constituent (electron or hole) of the neutral donor or acceptor is left in an electronic excited state upon annihilation of the BE. These transitions can be used to estimate the donor or acceptor binding energy by assuming an effective mass hydrogenic model (section 1.5). two-electron transitions of this type have been observed in CdSe by various groups [4.3,4.4]. Henry et. al. [4.4] have determined in this manner that a typical donor binding energy in CdSe is 19.5 meV. Analogous two-hole transitions have not, until now, been reported.

Pumping the high energy polariton peak A1 resonantly produced a spectrum identical to one resulting from above band-gap excitation. This is further evidence that the capture of polaritons by neutral donors and acceptors is the main source of BE luminescence. Pumping the second polariton peak A2 (figure 4.7a) produced a spectrum almost like an above band-gap one except that the polariton LO replica is almost non-existent and the strength of the line labeled α is much greater. We conclude that α and γ, which are approximately the same distance above β and δ, respectively, are two-electron transitions from an excited state of the donor BE lying above A2. α and γ are the corresponding two-electron transitions from the BE ground state, as

verified by resonant pumping of I2 (figure 4.7b). Excited states of BE have been studied in CdS by Malm and Haering [4.19], Henry and Nassau [4.20] and more recently by Puls et. al. [4.21-4.23]. The strongest of these, called c, is located ~3 meV above the ground state, equal to the approximate γ-δ and α-β splitting. Hence α and γ probably result from the c excited states of the donor BE responsible for δ and β. The extraordinary strength of these excited state lines indicate that the excited state lifetimes must be of the same order of magnitude as that of the BE ground state, and that the relaxation to the ground state is relatively slow. Furthermore, the capture cross section of a polariton into a donor BE excited state must be large. This is perhaps not surprising considering the near resonance of these excited state with the A2 polariton in our CdS samples, as evidence by the dramatic increase in the α line strength with resonant excitation of A2 (figure 4.7a).

Pumping I2 resonantly as in figure 4.7b results in a spectrum consisting of only the ground state two-electron transitions and the 1 and 2-LO phonon replicas of I2. By varying the wavelength of the pump source slightly within the I2 linewidth, the ratios of δ and β can be changed, suggesting that they arise from different donors. δ is favored by excitation on the high energy side of I2. δ seems to correspond to the two-electron transition of an exciton bound to a substitutional donor such as the one studied by Henry et. al. [4.4]. A study in CdS of 7 different substitutional donors [4.24] shows that central cell corrections are very small and that consequently the donor binding energy can be calculated to about ± 1 meV by assuming a

hydrogenic model. The line β, which from its excitation dependence seemed to correspond to a donor which binds an exciton more strongly, was however higher in energy than the line δ. This indicates a large negative central cell correction, which by analogy to CdS, suggests that the center responsible for β is probably not a simple substitutional donor.

Pumping I1 resonantly results in the spectrum shown in figure 4.7c. It consists of the LO phonon replicas of I1 and a line labeled I1-2-hole along with some other weak, unidentified lines. Assuming a hydrogenic model and noting that this line is 57 meV below I1 leads to an estimate of the acceptor binding energy E_A of 76 meV. This is substantially less than the ~109 meV binding energy of the Li & Na acceptors in CdSe [4.2]. The value of 76 meV is, however borne out by the position of the DAP band. The photon energy of the DAP luminescence is given by (section 1.7)

$$E_{DAP} = E_G - (E_A + E_D) + \frac{e^2}{\epsilon R} \qquad 4.1$$

where R is the distance between the donor and acceptor. For CdSe the polariton binding energy is ~16 meV [4.25,4.26]. Adding this to the energy of the lowest polariton (A2) yields for the band-gap energy E_G = 1824 + 16 = 1840 meV. Using 20 meV [4.4] as the donor binding energy E_D, and 1750 meV corresponding to the peak of the DAP band as E_{DAP} and estimating the Coulomb term to be 7 meV from the difference between the low energy edge and the peak of the first DAP band gives a rough estimate of 77 meV for E_A, the acceptor binding energy. This

is in remarkably good agreement with the previous result.

Time-resolved spectra with resonant excitation of I2 show that at least for the first 5ns or so all lines decay with the same lifetime, further confirming that all lines in figure 4.7b are replicas of I2. Similarly all lines in figure 4.7c, with resonant excitation of I1, decay at the same rate. At longer delays after the laser pulse some unidentified, longer lived, broad luminescence bands appear.

The luminescence decay curves of the BE with resonant excitation were obtained by monitoring the luminescence at the 1-LO phonon replica while pumping the no-phonon line directly. As mentioned previously, a pump level dependence was again observed, although due to the relative weakness of the LO replica it could not be followed over as wide a range as with above band-gap excitation. With this resonant excitation we were able to extend the I2 lifetime to ~0.8 ns and the I1 lifetime to ~1.7 ns. Inserting a 10^2 neutral density filter reduced the I2 lifetime to ~0.2 ns and the I1 lifetime to ~1 ns. With resonant excitation, saturation of the polariton decay rate cannot be a factor and hence this clearly shows that some other mechanism in addition to saturation was responsible for the power dependence of the I2 lifetime with above band-gap excitation (figure 4.5).

There was some excitation wavelength dependence of the I2 lifetime. Pumping the high energy side of I2 resulted in a longer, single-exponential decay, whereas the low energy side showed a dual exponential decay with an initial much faster (typically 250 ps) decay followed by a longer decay (1 ns) more characteristic of the high

energy side. One possible explanation for this is again the existence of 2 different donors with different BE lifetimes. The fast component would then correspond to the decay of excitons bound to the donor primarily responsible for the low energy side of I2, and the long component to the tunnelling of the shallower, longer lived donor BE to the deeper states. The behaviour of the two-electron transitions previously associated with the high and low energy sides of I2 is however, incompatible with this explanation since in this case one would expect to see a buildup of β with low energy excitation. These expectations are not borne out by experiment. Neither δ or β show a buildup and both δ and β have both a fast and a slow component following excitation on the low energy side of I2, albeit with different ratios of fast to slow components. No consistent explanation of these observations has been offered.

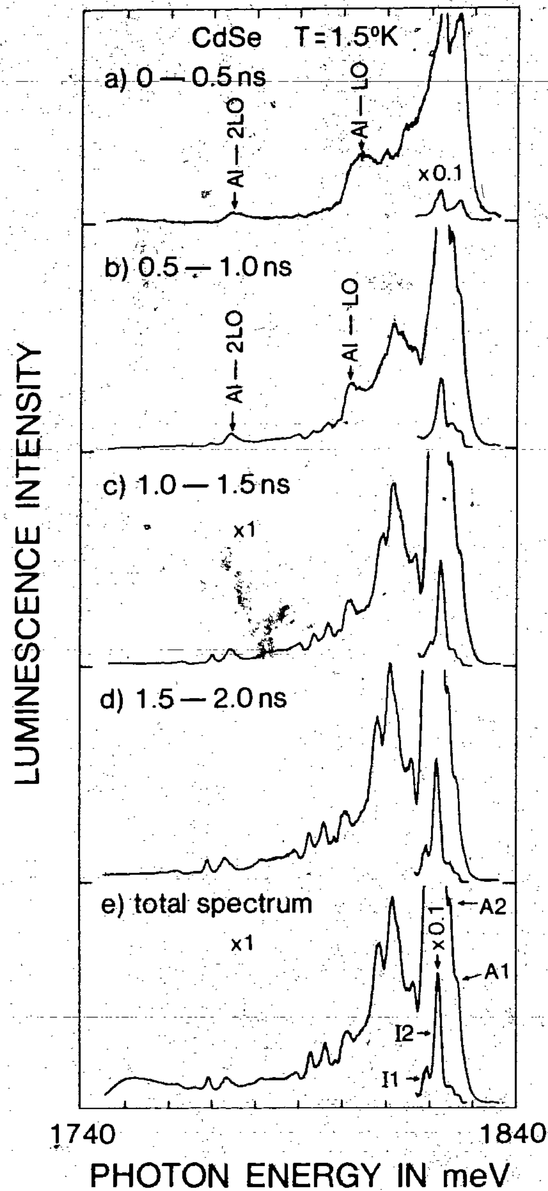

Figure 4.6

Time-resolved spectrum with ~100 mW/cm² of above band-gap excitation.

a) 0 - 0.5 ns after laser pulse

b) 0.5 - 1 ns   c) 1 - 1.5 ns   d) 1.5 - 2 ns

e) total, time integrated, spectrum

The region of the I1 and I2 peaks has been reduced by a factor of 10 in every spectrum.

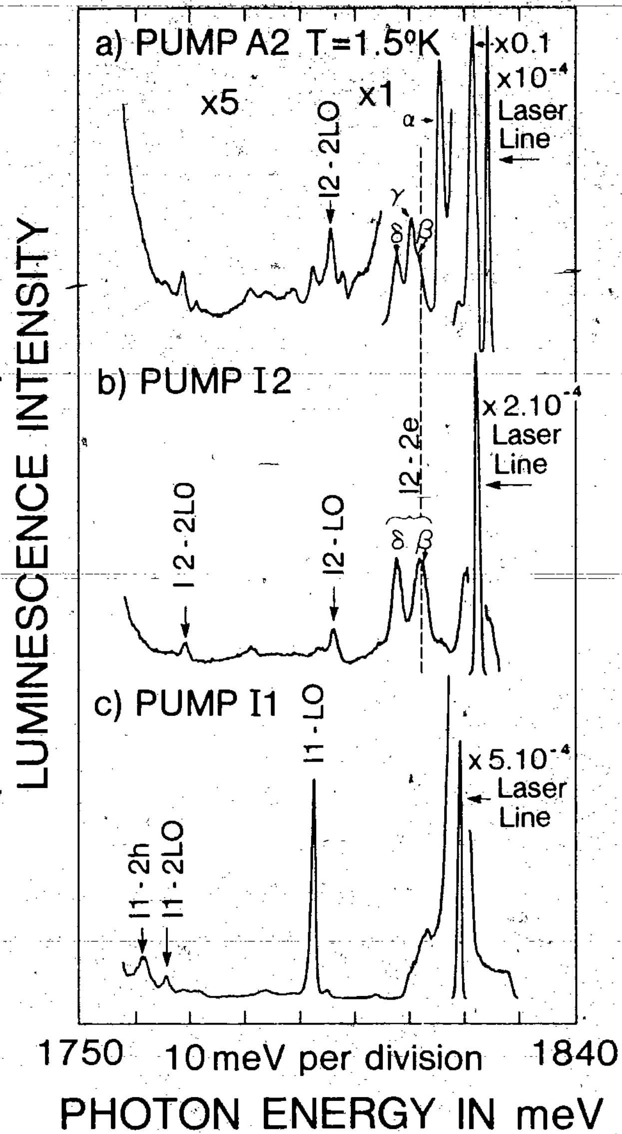

Figure 4.7

Resonant excitation spectra showing the replicas of the BE lines.

a) pumping A2

b) pumping I2

c) pumping I1

The broken line shows that the shoulder seen in a) is due to the line labelled in b).

5 PHOTOLUMINESCENCE LIFETIMES OF BE IN ZnSe

5.1 INTRODUCTION

The decay rate of BE in II-VI semiconductors was first studied in CdS using the phase-shift method [5.1] (section 2.1). The lifetimes of the donor and acceptor BE were found to be 0.5 and 1.0 ns, respectively, in good agreement with a theory previously put forward by Rashba and Gurgenishvili [5.2,5.3]. More recently Sanders and Chang developed a theory for effective-mass like BE decay times and have calculated the expected donor and acceptor BE lifetimes for many materials [5.4]. There exists, at this time, very few experimental results with which to compare these predicted decay rates.

The phase-shift method used to determine the BE lifetimes in CdS depends on there being only one simple exponential decay component. The presence of a second component or of a slow buildup results in ambiguities in the interpretation of the data. The advent of synchronously pumped modelocked dye lasers and fast photomultiplier tubes has opened the door to direct lifetime measurements in the sub-nanosecond regime coupled with great sensitivity and dynamic range. Recently, using such a system the lifetimes of BE in CdSe have been determined (section 4.3). This was also done by Minami and Era, [5.5] who obtained substantially longer lifetimes possibly indicative of higher quality samples. The observed lifetimes are often shortened by large impurity concentrations or high laser pump power due to overlap of the very extended BE wavefunctions. The most reliable

measurements of the unperturbed BE lifetimes are thus obtained from high quality samples in the low excitation power limit. Here the results of BE lifetime measurements in ZnSe are presented. This material is of technological interest because of the possibility of making photoemitting devices in the blue spectral region [5.6]. The quality of available ZnSe is as a result quite good.

5.2 EXPERIMENTAL RESULTS

The experimental apparatus consists of the actively modelocked, synchronously pumped, cavity dumped dye laser system using R6G dye (chapter 2), producing a train of 10 ps wide pulses at 590 nm with a repetition rate of 4 MHz. To create the necessary above-band-gap photons (2.83eV for ZnSe), a KDP frequency doubling crystal was used. The resultant 295nm beam was then focused on to the samples, which for these experiments were immersed in superfluid He at 1.8K. The average power density of excitation incident on the sample was ~10 mW/cm^2 corresponding to a peak power of ~250 W/cm^2. The photoluminescence was analyzed using a single stage 3/4 m spectrometer and detected by a microchannel plate photomultiplier tube (Hammamatsu R1294U-01). The samples used in this study were all bulk samples doped with Na, Li, Cu, Ag and Au acceptors [5.7]. No characterization data was supplied for these samples which were obtained from Phillips.

The donor BE line (I2) decays extremely rapidly (figure 5.1e). Deconvoluting (appendix 3) with the measured instrumental response function and verifying the results in several different samples produces a measured lifetime of 50 ± 10ps, close to the limit of our experimental time resolution. The unresolved Na & Li acceptor BE lines (I1) have a lifetime of 360ps (figure 5.1d). Only one lifetime component was observed in a sample containing both Na and Li acceptors, indicating that both acceptor BE have the same lifetime. This is expected within the framework of the Rashba and Gurgenishvili model in which the BE lifetime in a given material is dependent only

on the exciton localization energy. The Cu-related line labeled I1-deep has a lifetime of 960ps (figure 5.1b). Doping with Ag results in an emission corresponding to a very strongly localized BE with a series of LO phonon replicas [5.7]. This line (labeled Ag_1° by Dean et. al. [5.7]) has a time decay constant of 2.7ns. We were unable to observe the Ag_2° line, which is isoenergetic with I1, or the Au BE reported to lie just below the usual I1 line, presumably because of the very low average power of our excitation source.

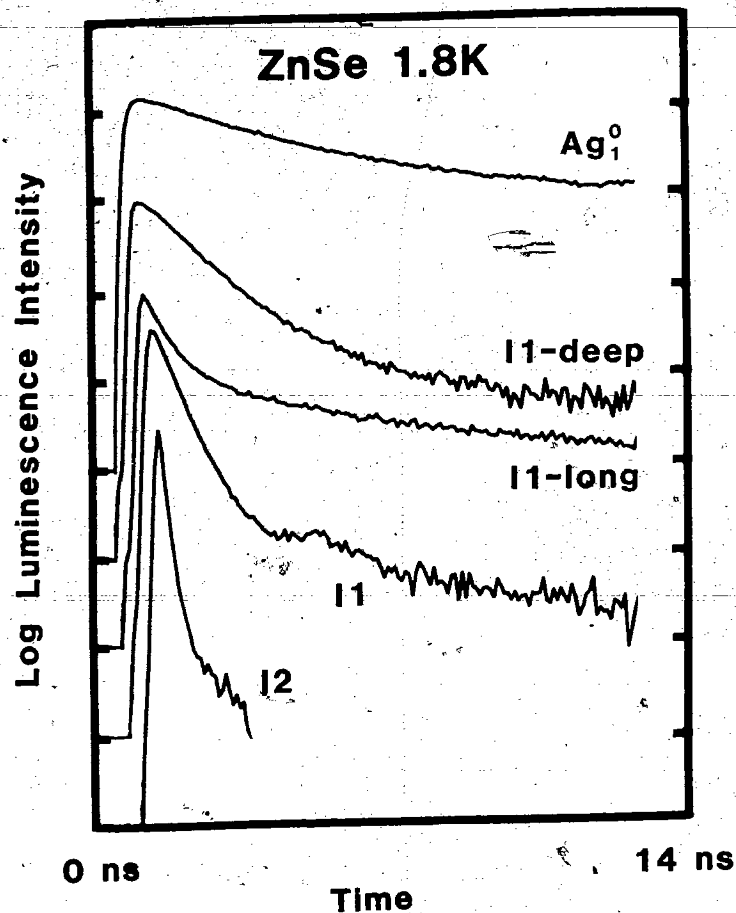

Figure 5.1

The luminescence decay of the various BE lines after pulsed excitation. I2 and I1 are the shallow donor and acceptor BE respectively. The trace labelled I1-long corresponds to a perturbed shallow acceptor center. I1-deep is the Cu-related BE line, whereas Ag_1^o is an Ag related BE line. The numerical values of the lifetimes are shown in Fig. 5.2. Each of the tick marks on the vertical scale represents one decade of intensity. The curves have been displaced vertically for clarity.

5.3 COMPARISON WITH THEORY

Figure 5.2 is a log-log plot of the observed BE lifetime vs. the exciton localization energy E_b. The dashed line, arbitrarily drawn through the I1 point, corresponds to the trend predicted by the theory of Rashba and Gurgenishvili which gives (section 1.3)

$$\tau \propto E_b^{3/2} \qquad 5.1$$

The experimental points are in reasonable agreement with this theory even for the deep Ag acceptor complex responsible for the Ag_1^o line. Consequently, the observed BE decays correspond to dominantly radiative lifetimes, since the Auger rate increases with increasing BE binding energy [5.8] (section 1.4), and hence if it were important there would be a reversal of the observed trend to longer lifetimes with increasing exciton localization energy. This is in contrast to the reported case of ZnTe where the Auger mechanism does play an important role for the deeper BE [5.9].

The BE lifetime τ is related to the transition oscillator strength f by equation 1.26

$$\tau = \frac{4.50\lambda^2}{nf} \qquad 5.2$$

where λ is the transition wavelength in cm in vacuum and n is the

refractive index. According to the Rashba and Gurgenishvili theory, the impurity BE oscillator strength is related to the FE oscillator strength per molecular volume f_x by equation 1.50

$$f = f_x \frac{8\pi \ell^3}{\Omega_o} \qquad 5.3$$

where Ω_o is the volume of one ZnSe molecule and ℓ is the characteristic length of the impurity BE wavefunction. The relationship between the characteristic length and the BE localization energy E_b is given by equation 1.49

$$\ell = \frac{\hbar}{\sqrt{(2mE_B)}} \qquad 5.4$$

where m is the exciton mass. Using equations 5.2-5.4 with the values $n = 2.61$ [5.10], $\Omega_o = 4.1\times10^{-2}nm^3$ [5.10], $m = .91m_o$ [5.10] and $f_x = 1.4\times10^{-3}$ [5.11] appropriate for ZnSe as well as $\lambda_{I2} = 4.43\times10^{-5}cm$, $\lambda_{I1} = 4.44\times10^{-5}cm$, $E_{I2} = 5.6$ meV and $E_{I1} = 10.5$ meV from the measured spectra, yields the predicted I2 and I1 lifetimes of 200 and 495 ps respectively.

Rashba and Gurgenishvili (section 1.3) calculate the envelope BE wavefunction by using a delta function potential with adjustable strength. This does not lead to a very realistic BE wavefunction although the theory does seem to correctly predict the BE lifetime dependence on the localization energy. In particular, the theory

treats the recombination as occurring entirely within the exciton. No provision is made for recombination with the impurity carrier. It also does not include the effects of inter-particle correlations on the wavefunction. Sanders and Chang [5.4] have attempted to rectify some of these deficiencies, within the spherical effective mass approximation, by constructing a variational BE envelope wavefunction which includes correlation effects. The wavefunction depends on the ratio of the impurity carrier mass to the mass of the carrier of the opposite sign. Thus, for a donor the mass ratio σ is given by $\sigma = m_E/m_H$. The wavefunction is adjusted to correctly handle the known limits of small and large σ corresponding to analogs of the H_2 and H^- systems respectively. They obtain for the impurity BE oscillator strength the expression

$$f = \frac{P^2}{\hbar\omega} |\langle I|F\rangle|^2 \qquad 5.5$$

where ω is the angular transition frequency and P^2 is the energy equivalent band-to-band matrix element squared. They have calculated the value of the matrix element $\langle I|F\rangle$ for all values of the mass ratio σ. They do not give values for ZnSe, but using $\sigma = 0.21$ for donors and $\sigma = 4.76$ for acceptors and their figure 3, the estimated overlap integrals are $|\langle I|F\rangle|^2 = 17.8$ for I2 and 1.41 for I1. The previously used FE oscillator strength of 1.4×10^{-3} corresponds to a P^2 of 20.0 eV [5.11]. Using this value of P^2 and equations 5.5 and 5.2 results in predicted lifetimes of 27 ps and 340 ps for I2 and I1, respectively.

These values are displayed as open circles in figure 5.2. These values are in quite reasonable agreement with experimental values for I1 and I2. This is in contrast to the reported case of CdSe [5.5], where the Sanders and Chang theory predicts lifetimes an order of magnitude shorter than the observed values.

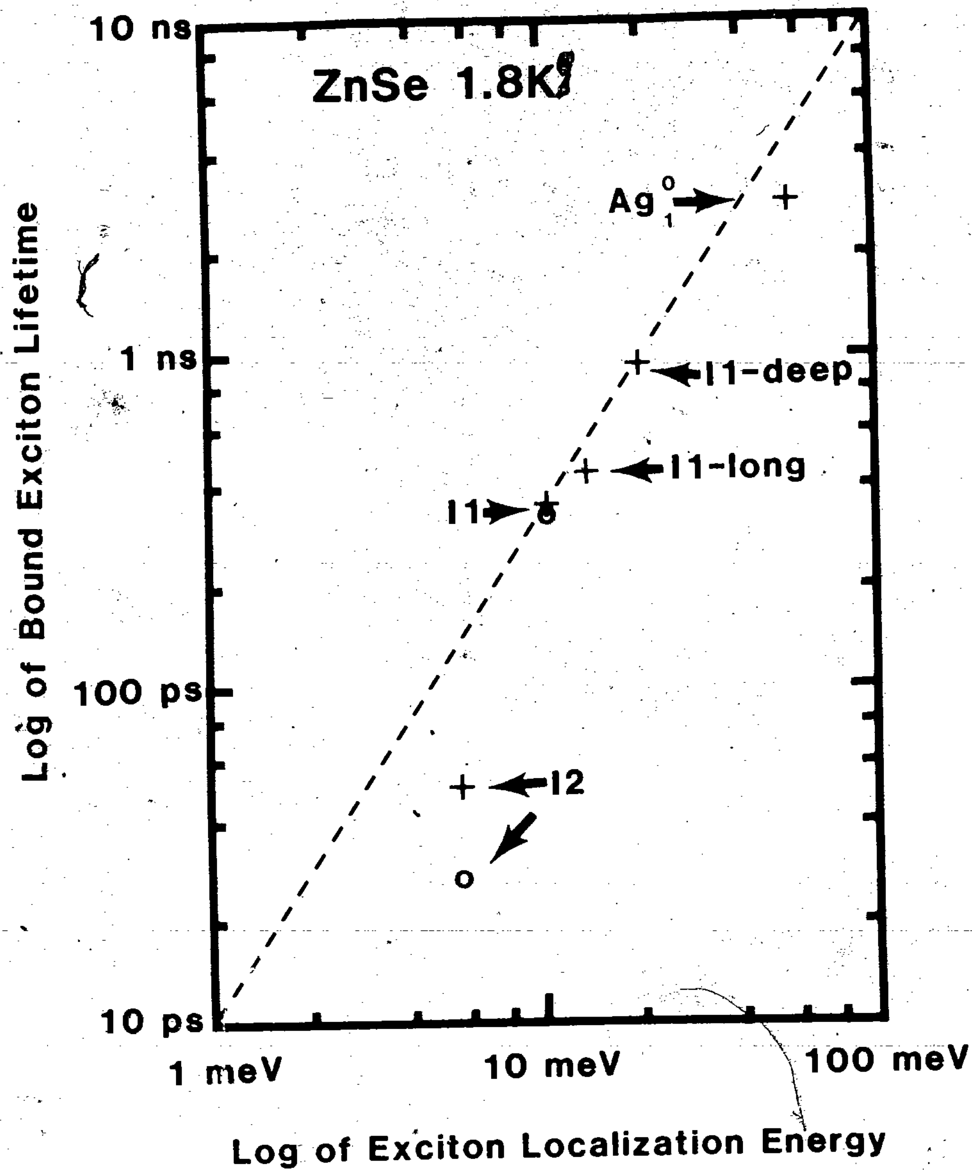

Figure 5.2

A log-log plot of BE lifetime vs. BE localization energy. The crosses represent the experimental points. The dashed line corresponds to the trend predicted by the Rashba and Gurgenishvili theory arbitrarily scaled to go through the I1 point. The open circles are the predicted values of the shallow donor and acceptor BE lifetimes as determined from the theory of Sanders and Chang.

5.4 TIME-RESOLVED SPECTRA

A series of time-resolved spectra of the sample doped with Na and Li (figure 5.3) shows that at long delay times after the laser pulses, two longer-lived lines emerge. One is immediately below the I1 line while the other lies below I1-deep. The line below I1, labeled I1-long, was observed in only two of our samples. Since both I1 and I1-deep have these associated lines, it seems reasonable that they are due to a perturbed version of the basic acceptor species. The time decay of I1-long is depicted in figure 5.1c. It shows a definite 2 component decay with a very strong long lived (~12 ns) component of unknown origin as well as an initial faster decay of ~440 ps. For the purposes of figure 5.2 we have assumed that this initial faster component is the radiative decay rate of excitons bound to this center. It is clear that these lower energy lines cannot be simple replicas of I1 and I1-deep since they do not have the necessary identical transient characteristics.

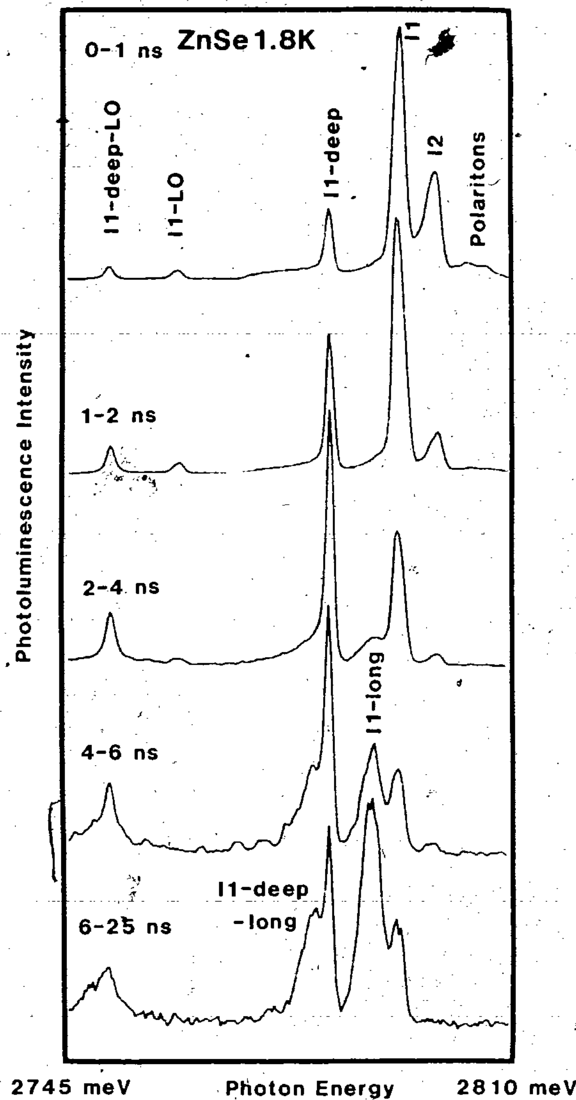

Figure 5.3

A series of simultaneously collected spectra which correspond to sequential time windows after the laser pulse. The first time window shows the very short-lived donor exciton I2 and the polariton luminescence. Later time windows reveal the emergence of the perturbed acceptor BE lines labelled I1-long and 1-deep-long. The spectrum for each time window has been normalized to the strongest line.

6 TRANSIENT PHOTOLUMINESCENCE STUDY OF DEFECT LINES IN MBE GaAs

6.1 INTRODUCTION

A series of sharp exiton-like lines just below the usual C_{As} acceptor BE line was first reported by Künzel and Ploog [6.1] in the low-temperature luminescence spectrum of high quality, p-type molecular beam epitaxially (MBE) grown GaAs (figure 6.1). Subsequently many groups have studied the intensity of these lines (henceforth called the KP lines) as a function of growth conditions and doping [6.1-6.5]. The tentative result of these investigations was that these lines could be due to the recombination of excitons bound to Ga vacancy-C complexes. This results is, however, by no means firmly established and no adequate microscopic model of the origin of the various lines of the defect complex has been suggested.

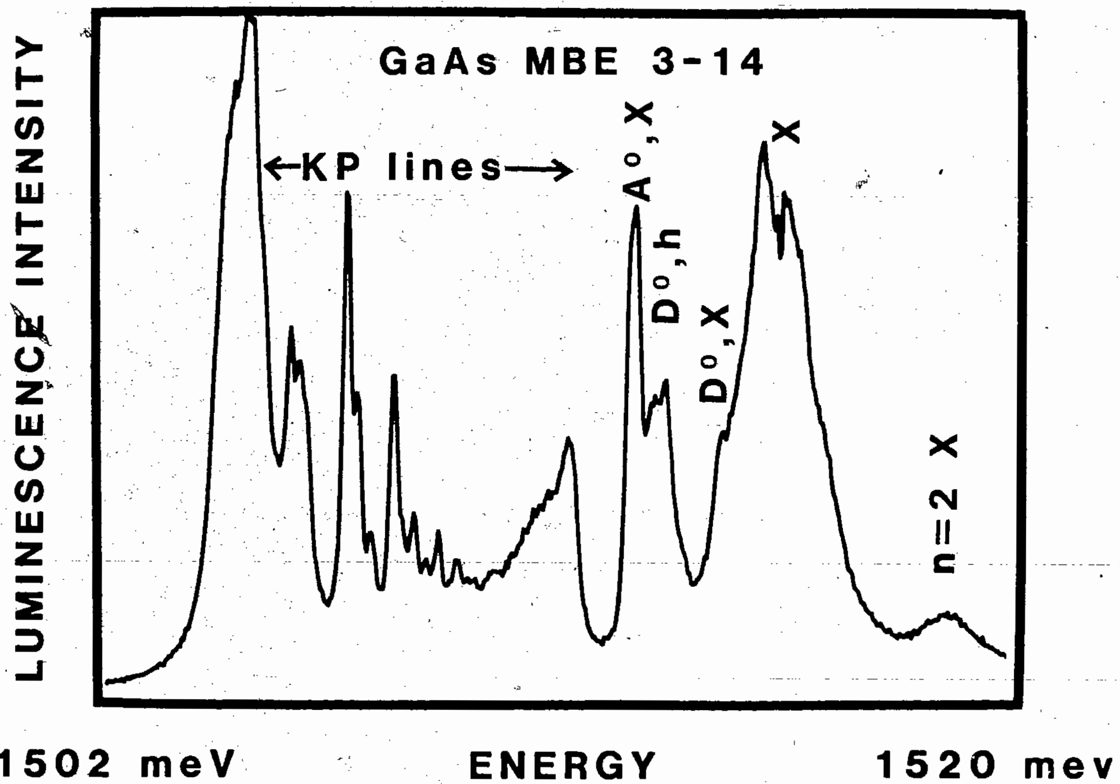

figure 6.1

This is a 1.8K spectrum of MBE GaAs showing the series of lines labelled KP below the energy of the usual acceptor BE labelled A°,X.

6.2 PROPOSED MICROSCOPIC MODELS

There have been some other models proposed which do endeavor to explain the details of the structure in the KP line spectral region (1504-1511 meV). Eaves and Halliday [6.6] proposed a model in which the lines correspond to excitons bound to acceptor pairs with different separations. The highest energy line (1511.1 meV), called g, would then correspond to an isolated acceptor BE, albeit a deeper one than the usual C acceptor BE in MBE GaAs. The line lowest in energy, or v, (1505.0 meV) would then correspond to excitons bound to nearest neighbor acceptor pairs. The lifetime of a BE is a sensitive function of binding energy [6.7] (section 1.3). The localization energy changes by a factor of ~2 in going from g to v, hence there should be an easily observable and continuous increase in the lifetimes of the lines going from g to v.

Reynolds et. al. [6.8] have suggested that the KP lines, of which they observe 60 subcomponents, are discrete DAP recombination lines between Si donors and C acceptors which are paired nonrandomly. This model is difficult to reconcile with the fact that the KP lines are quite strong in samples which have virtually no donor BE or free hole to donor luminescence from the epilayer. One of the characteristics of DAP recombinations is a very long lifetime which increases exponentially with increasing pair separation [6.9] (section 1.7). Thus, this second model predicts an easily observable change in the transient behavior of the KP lines going from the high-energy g to the low-energy v line.

6.3 TIME-RESOLVED SPECTRA

The experimentally observed transient behavior of the KP lines does not support either of these models. The line g and its associated low-energy shoulder were found to decay very much like the C acceptor BE line. The low-energy KP lines p through v, however, were found to have an identical transient behavior which differs substantially from that of g, and is much faster than typical DAP recombination rates.

The samples used in this study are the same as those reported on in two previous works [6.4,6.10]. These samples were all unintentionally doped p-type samples 3 to 4 microns thick grown by MBE and obtained from STE. Some of these samples, namely, samples 3-4, 3-9, and 3-14, have very small donor concentrations as evidenced by the single polariton peak and lack of donor BE luminescence [6.10]. These same samples had strong KP luminescence of the same general shape as that first reported by Künzel and Ploog [6.1].

The samples were immersed in superfluid He for the photoluminescence measurements. The luminescence was excited using the modelocked, cavity dumped dye laser system described in chapter 2 with a repetition rate of 4 MHz and a pulse width of <30 ps operated either above the band-gap (590 nm) or resonantly at the polariton wavelength (818 nm). The luminescence was analyzed using a double 3/4m spectrometer and detected by the time correlated photon counting system described in section 2.6 and 2.7 using the Varian VPM 159A3 photomultiplier. Simultaneously collected time-resolved spectra collected by the system described in section 2.7 were found to be

particularly useful in this experiment.

A series of time-resolved spectra of sample 3-4 using above-band-gap excitation is shown in figure 6.2. This series of spectra, with large 25-ns time windows, clearly shows that the acceptor BE and the g line decay much more quickly than do the lines p through v, which decay with identical or very nearly identical lifetimes. The relative intensities of these lines do not change even out to 180 ns after the laser pulse. Higher spectral resolution than that employed in figure 6.2 shows that the lines from p to v which are unresolved in figure 6.2 also decay identically with the main lines. The luminescence decay curves of some of these lines are shown in figure 6.3. The C acceptor BE (A^o,X) and the g line have identical lifetimes of 1.2 ± 0.1 ns which follows the polariton decay at this average pump intensity of ~500 mW/cm². At lower pump powers, where the polariton decay channels are not saturated, the g line has a lifetime slightly longer than that of (A^o,X), as expected from the general considerations of lifetime versus binding energy discussed in section 1.3. The top decay curve of figure 6.3 is from the v line and the second from the top is from the unresolved q,r,s lines. These lines, as well as the others between p and v, have an initial exponential decay time constant of 2.4 ± 0.1 ns followed by a relatively strong, longer lived component having a time constant of 26 ± 1 ns. The decay curves of all the p through v lines are indistinguishable. Note from figures 6.2 and 6.3 that both the C acceptor BE (A^o,X) and the g line also have a similar long-lived component (τ = 24 ± 3 ns) but that its relative strength is an order of magnitude weaker. It is assumed

that the fast components of all these decays, which are more characteristic of direct gap impurity BE, are the true radiative decay rates, while the long components are due to the transfer of excitation from some unidentified long-lived source.

The details of the decay curves depend somewhat upon the excitation density even in this relatively low power regime presumably due to wavefunction overlap with other nearby impurity BE, an effect which appears to be quite common in direct gap semiconductors (section 4.4). The general result that g and (A^o,X) decay more quickly than p through v, and that all p through v components decay similarly, does not, however, depend on the excitation density.

Lifetime measurements reported by Halliday et. al. [6.11] agree qualitatively with the above results. Their value for the g line lifetime is 1.0 ns in close agreement with the result presented here. The lifetimes of the lower energy lines were all reported to be ~3 ns and identical within the quoted margin of error. Halliday et. al. however chose to interpret these results as evidence for the paired acceptor model. Skolnick et. al. [6.12] have also reported lifetime measurements of the KP lines in a sample which shows a large number of resolved lines. They obtain a lifetime which increases smoothly from a value of 1.5 ns for the g-line to a value of 12 ns, for the line labelled q (14 in their notation) and all the remaining lower energy lines. On the basis of these results Skolnick et. al. argued that the paired acceptor model is applicable for the higher energy set of lines with the line q as the series limit, but that the lower energy lines have a different origin. Further evidence for this proposal is the

observation [6.13] of possible two-hole replicas of all the lines between g and p indicating the acceptor nature of these lines. It is noteworthy however that no two-hole replicas of principle lines lower in energy than p were discernible. On the other hand excitation spectroscopy results for portions of the v line [6.14] show contributions for all the higher energy lines, excluding g and its lower energy wing, in approximately the same ratios as seen in luminescence. This lends weight to the conclusion drawn from the time-resolved spectra that the lines p through v originate from the same initial state. If this were not the case the strong coupling between the lines p through v demonstrated by the excitation spectroscopy would result in all the luminescence intensity originating from the lowest energy line v.

In conclusion, time-resolved spectroscopy of the KP lines clearly shows that the two microscopic models of the KP lines discussed in the introduction cannot be applicable for the whole KP spectrum since both would predict a steady increase in lifetime for the series g through v which was not observed experimentally. It is possible that the paired acceptor model is applicable for the higher energy set of lines, but the weight of experimental evidence suggests that the lower energy lines have a different, as yet undetermined, origin.

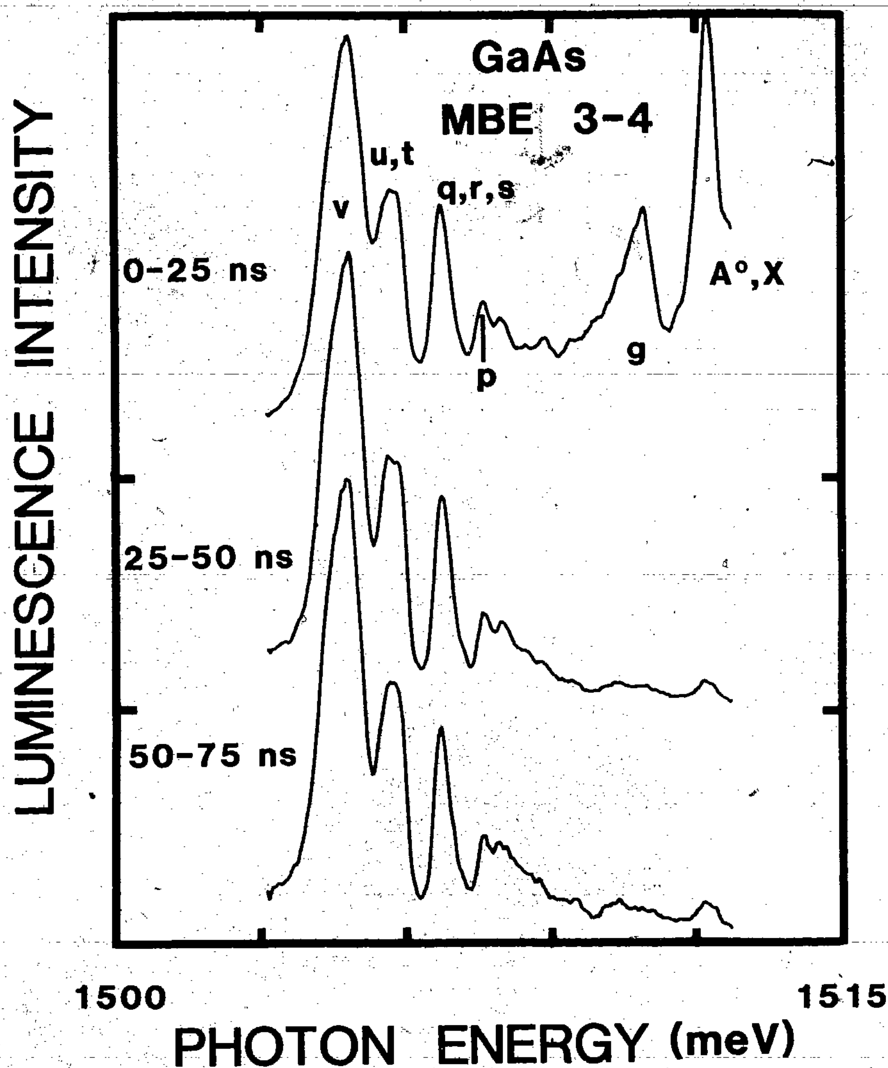

Figure 6.2

Sequence of spectra recorded during sequential 25-ns time windows after the laser pulse. After the initial fast decay of the acceptor BE, the shape of the spectra remain unchanged during later time windows out to 175 ns after the laser pulse. The sample temperature was ~1.6K and the average excitation density was 500 mw/cm² at 590 nm.

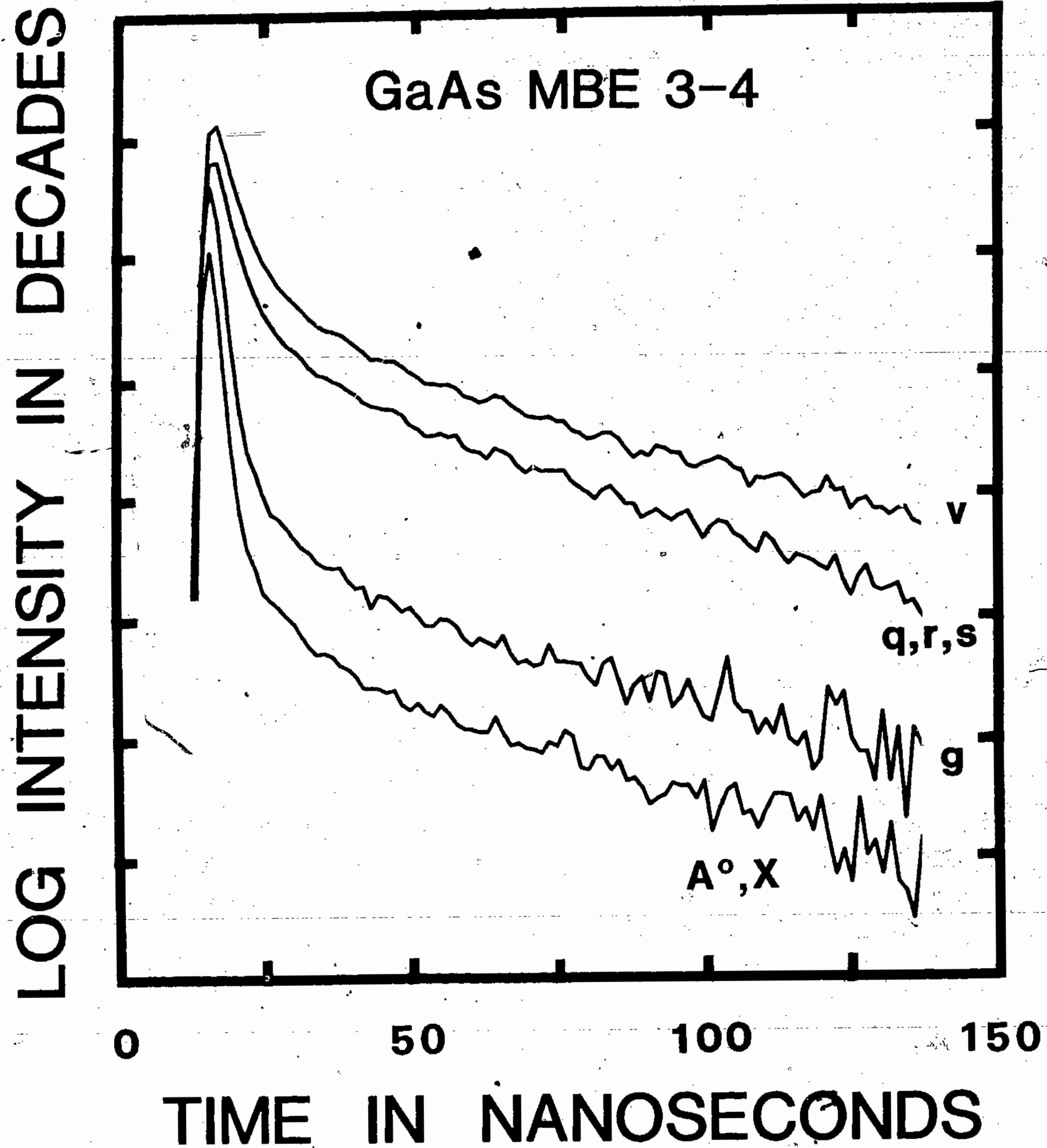

Figure 6.3

Luminescence decay measurement of selected lines shown in Fig. 6.1 under identical experimental conditions. At this excitation density the lifetimes of the lines are the following. q,r,s and v: 2.4 ± 0.1 ns short component, 26ns ± 1.0ns long component; (A^o,X) and g: 1.2ns ± 0.1ns short component, 24ns ± 3ns long component:

6.4 RESONANT EXCITATION OF THE g LINE

The result of these time resolved photoluminescence observations is that the KP lines consist of two distinct groups: g and its low-energy wing, and the lines p through v. This conclusion has already been reached by Contour et. al. [6.15] on the basis of resonant excitation with the subsequent observation of a two-hole replica (section 1.5) of g. The acceptor BE two-hole replicas are, in general, difficult to observe since they occur in the same spectral region as the donor-to-acceptor and free electron-to-acceptor transitions (section 1.7). Time-resolved spectroscopy can be of some utility here since the decay of the two-hole transitions must follow that of the acceptor BE whereas the free-to-bound and donor-acceptor pair transitions in this region have a decay time of hundreds of nanoseconds. By setting short time windows, it is possible to discriminate against the unwanted, long-lived luminescence.

A series of time-resolved spectra for MBE samples 3-4 with short (1.3 ns) windows and resonant excitation of the polaritons is presented in Fig. 3. On the top left, for comparison, is shown the 0-1.3 ns spectrum of a metal organic chemical vapor deposition (MOCVD) sample which does not exhibit any KP luminescence. It shows only the regular C acceptor 1S-2S (1493.7 meV) and 1S-3S (1489.8 meV) two-hole transitions. The MBE samples which have KP luminescence show additional short-lived luminescence features at 1494.8 and 1497.0 meV. The intensity of both of these peaks correlates with the intensity of the g line in the series of spectra extending to longer delay times.

The intensities of these peaks relative to the g line were also found to be constant among the MBE samples. This, as well as the absence of these lines in the MOCVD sample, indicates that these lines are replicas of g. We have interpreted the 1497.0 meV line as the 1S-2S replica and the 1498.8 meV line are the 1S-3S replica. Contour et. al. [6.15], who observed a broad peak around 1497 and a sharp line at 1497.8 meV, interpreted the 1494.8 meV line as the 1S-2S transition and the 1497 meV peak as the free electron to g-acceptor transition. Our transient results, however, clearly show that the 1497 meV peak cannot be a free-to-bound transition since the decay of such a transition follows the free-electron population, which is much longer lived as evidenced by the slow decay of the free electron to C-acceptor transition (e-A^{o}, figure 6.4). The new assignment of these replicas puts the 1S-2S energy difference of the g acceptor at 14.0 meV and the 1S-3S energy difference at 16.3 meV. Assuming a simple hydrogenic model (section 1.5), this gives a g-acceptor binding energy of ~18.5 meV, considerably less than the 22.9 meV deduced by Contour et. al. [6.15] or the 26.0 meV of the C acceptor. [6.16]

In conclusion the line g was determined on the basis of its transient behavior and the observed two-hole transitions to be due to an acceptor BE, confirming a previously published result on the nature of g [6.15]. However, the binding energy of g was found to be only ~18.5 meV, rather than the 22.9 meV previously reported, [6.15] on the basis of a reinterpretation of the observed replicas of g.

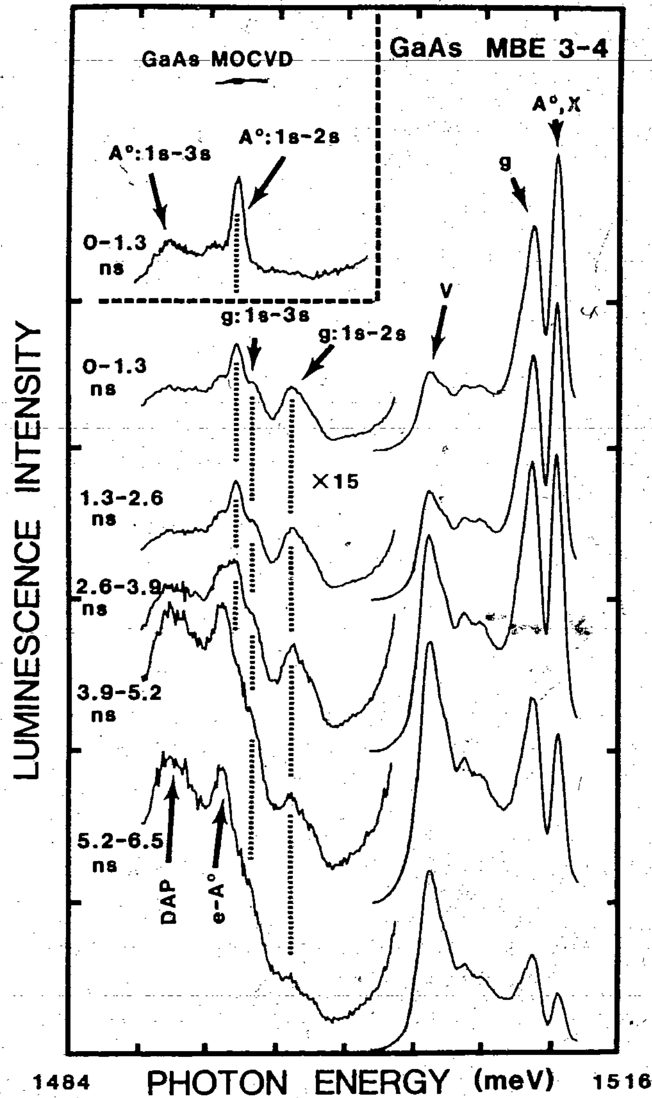

Figure 6.4

Series of spectra with sequential 1.3-ns windows after the laser pulse. The early windows show the BE features while the later ones show the rise of the donor and free electron-to-acceptor transitions (DAP and e - A°). A spectrum of an MOCVD sample is shown in the top left corner for comparison. These spectra were recorded by resonantly pumping the polariton with an average excitation density of ~20mW/cm² at a sample temperature of 1.6K. The two-hole replicas of the principal C-and g-acceptor BE peaks (A°,X and g, respectively) are labelled 1s-2s or 1s-3s depending on the final acceptor state.

7 THE EFFECT OF NEUTRAL DONOR SCATTERING ON THE TIME DEPENDENT POLARITON PHOTOLUMINESCENCE IN GaAs

7.1 INTRODUCTION

In direct gap semiconductors with dipole active excitons there exists a strong coupling of FE with photons of the same energy resulting in mixed modes called polaritons [7.1] (section 1.6). The nature of the polariton dispersion relation (figure 1.1a) has a profound effect on the luminescence mechanism in this energy region [7.1,7.2]. No-phonon polariton luminescence results from those polaritons which upon reaching the surface, are converted into photons external to the crystal. Thus, a theoretical description of polariton luminescence becomes a transport problem [7.3]. This introduces considerable complexity to the description of the luminescence, with the net result that the experimentally observed no-phonon polariton luminescence lineshape does not necessarily reflect the population distribution of polaritons inside the crystal.

The usual experimentally observed exciton-polariton spectrum is a doublet, rather than the singlet expected from the quasi-equilibriated polariton population above the knee in the lower branch of the dispersion curve [7.4]. This doublet structure has been interpreted in many ways. Gross et. al. [7.5] explained the higher energy polariton peak in CdS as arising from a minimum in the reflectivity of the surface at this energy. Sell et. al. [7.6] attributed the doublet polariton spectrum in GaAs to emission from the two polariton

branches. Alternatively the doublet has been attributed to polariton, free-electron scattering [7.7], or to intrinsic reabsorption (meaning scattering from phonons [7.2,7.8]) of polaritons moving towards the surface [7.9-7.11]. It has also been suggested that polariton impurity scattering is the dominant scattering mechanism at low temperatures [7.12]. Recently it has been experimentally shown that elastic neutral donor scattering has a marked effect on the polariton luminescence lineshape [7.13-7.15], and is consequently the scattering mechanism responsible for the 'reabsorption', where 'absorption' is here broadly defined as requiring only a change in direction of the polaritons. Very recently Schultheis and Tu [7.16] have instead suggested that the dip in the polariton spectrum is due to absorption caused by a surface electric field modified polariton resonance. Presented here is some experimental evidence which makes this last explanation unlikely for the samples used in this work. An alternative explanation of the experimental results of Schultheis and Tu will be suggested. However, it is important to understand the complexity of the problem and hence the limitations of a simplified model. Any mechanism which affects the transport of polaritons to the sample surface, the probability of transmission at the surface, the spatial distribution of polaritons in the crystal or the polariton energy distribution can influence the the observed polariton luminescence. Consequently, one can expect great variations in the observed emission with different samples, surface preparation or experimental conditions.

7.2 EXPERIMENTAL APPARATUS

The photoluminescence was excited using the modelocked synchronously pumped dye laser system described in chapter 2. This resulted in <10 ps pulses, at either 590 nm, well above the gap of GaAs, or around 820 nm for resonant excitation, by using the laser dyes R6G and styril 9 respectively. The intrinsic repetition rate of 80 Mhz set by the ion laser cavity length was reduced to 4 Mhz using a cavity dumper (section 2.5). The laser pulse train was directed onto the front surface of a MBE GaAs crystal immersed in superfluid He. The resultant luminescence was analyzed using the data acquisition system described in sections 2.6 and 2.7. The red response of the Hammamatsu micro-channel plate photomultiplier R1294U-01 proved to be insufficient for the GaAs work necessitating the use of the Varian photomultiplier (VPM159A3) with its lower time resolution (section 2.6). The incident excitation density on the samples had to be kept below about 1W/cm^2 in order to resolve the the different BE lines.

7.3 EXPERIMENTAL RESULTS

Using CW photoluminescence Koteles et. al. [7.13] have shown that the shape of the polariton luminescence depends strongly on the neutral donor concentration. A series of spectra of samples with progressively smaller donor concentrations as evidenced by the reduced donor BE and free hole to neutral donor (D^o,h) line intensities is displayed in figure 7.1. This set of samples (described in section 6.3) showed a change from the usual doublet to a narrow single line as the donor concentration was decreased. The results of time resolved measurements on the same series of samples are presented here. Figure 7.2b depicts a series of time resolved spectra of a sample having an intermediate neutral donor concentration (MBE 3-14) which, under CW excitation, exhibits only a single polariton peak. Note the evolution of the polariton lineshape from a doublet, at short delay times after the laser pulses, to a singlet at longer delays. Other samples, with even lower donor concentrations, such as MBE 3-9 have only a single peak at all times (figure 7.2c), whereas others with greater donor concentrations (eg. MBE 3-3) always have a doublet regardless of the time delay (figure 7.2a). For the sample with an intermediate donor concentration the singlet line shape is observed when the laser pump density is reduced as shown in figure 7.3b. Pumping the n=2 excited state of the polariton, just below the band-gap results in a singlet polariton peak in all samples, even those with relatively large donor concentrations (figure 7.3a). Careful observation of the transient luminescence curves (figure 7.4) shows that the dip is due to a slower

buildup of the observed luminescence in this energy region, rather than to a difference in luminescence decay rate. The polaritons in the energy region of the dip are thus delayed in their arrival at the surface with respect to polaritons of adjacent energies.

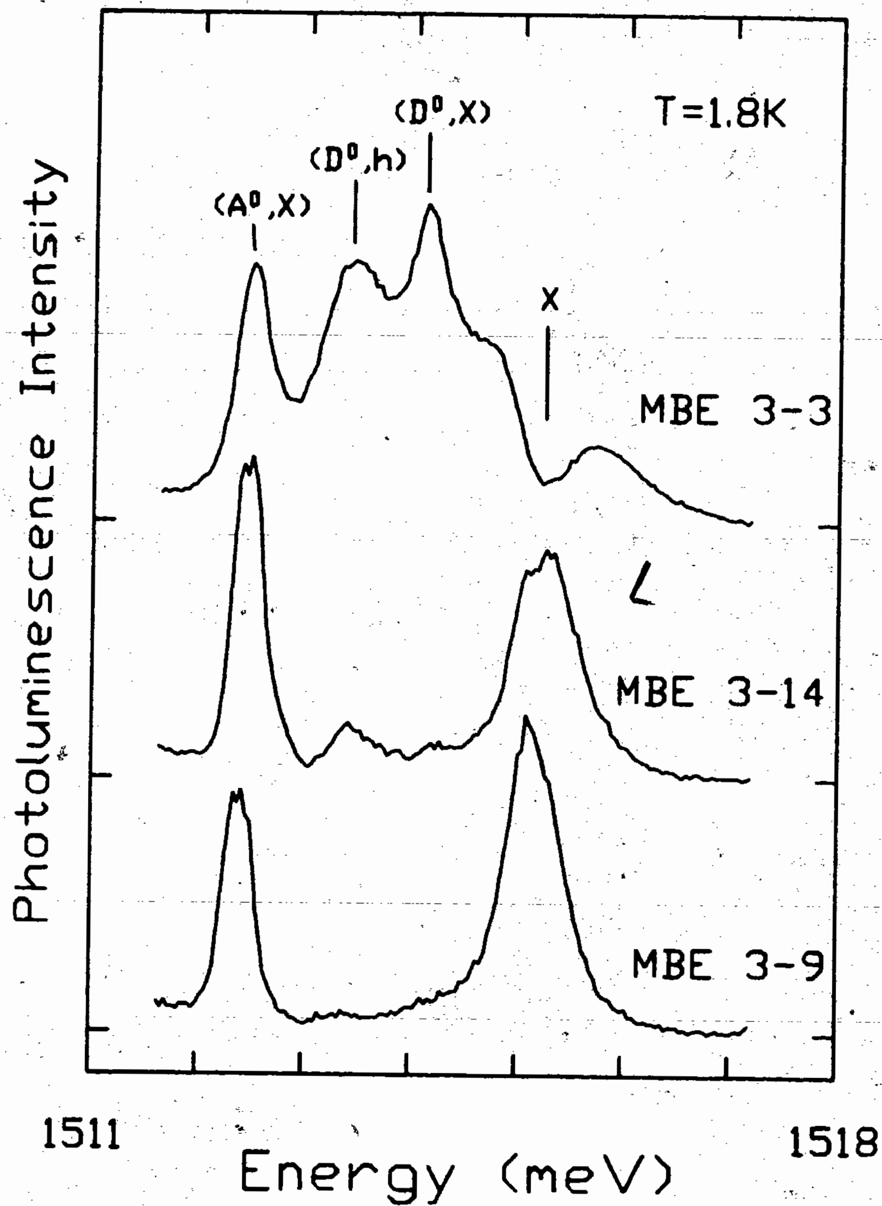

figure 7.1

These are CW spectra of a set of MBE GaAs samples with progressively lower donor concentrations as evidenced by the progressively weaker donor BE (D^o,X) and free hole to neutral donor (D^o,h) lines, as compared to the polariton (X) and acceptor BE (A^o,X) lines.

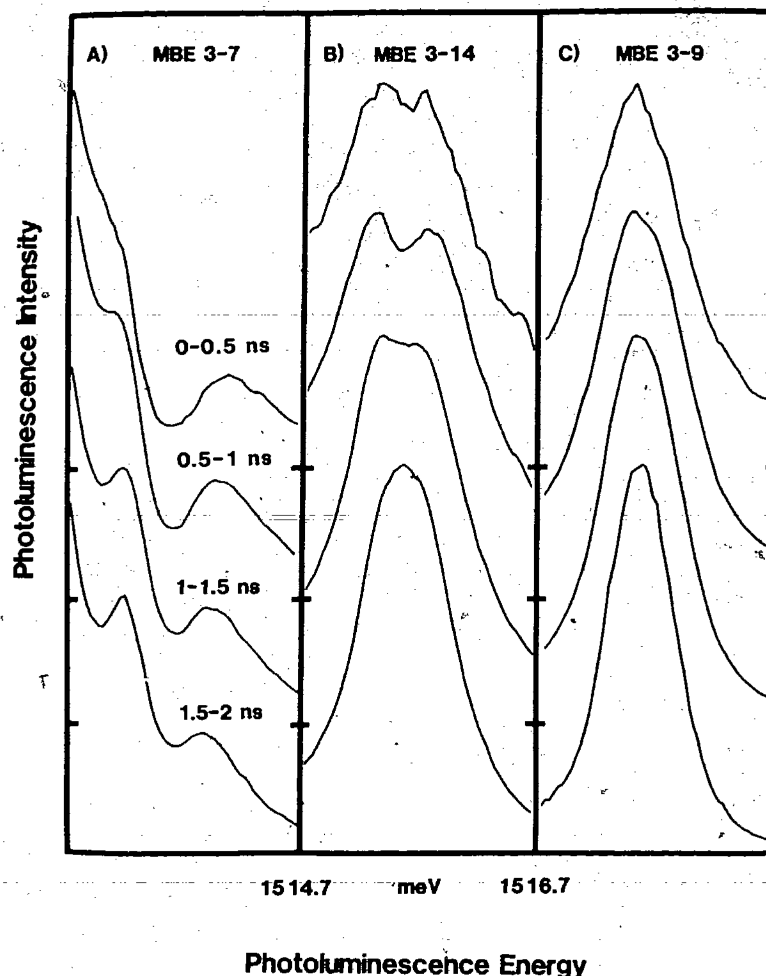

figure 7.2

A series of time-resolved spectra using 0.5 ns windows of 3 different samples with decreasing neutral donor concentration going from A) to C). Sample temperature was ~1.8K and the average excitation density was 500 mW/cm² corresponding to a peak power of ~10kW/cm². B) shows the time evolution of the dip in a sample with moderate neutral donor concentration. The energy scales for the three sets of spectra are identical to the one given for the central set.

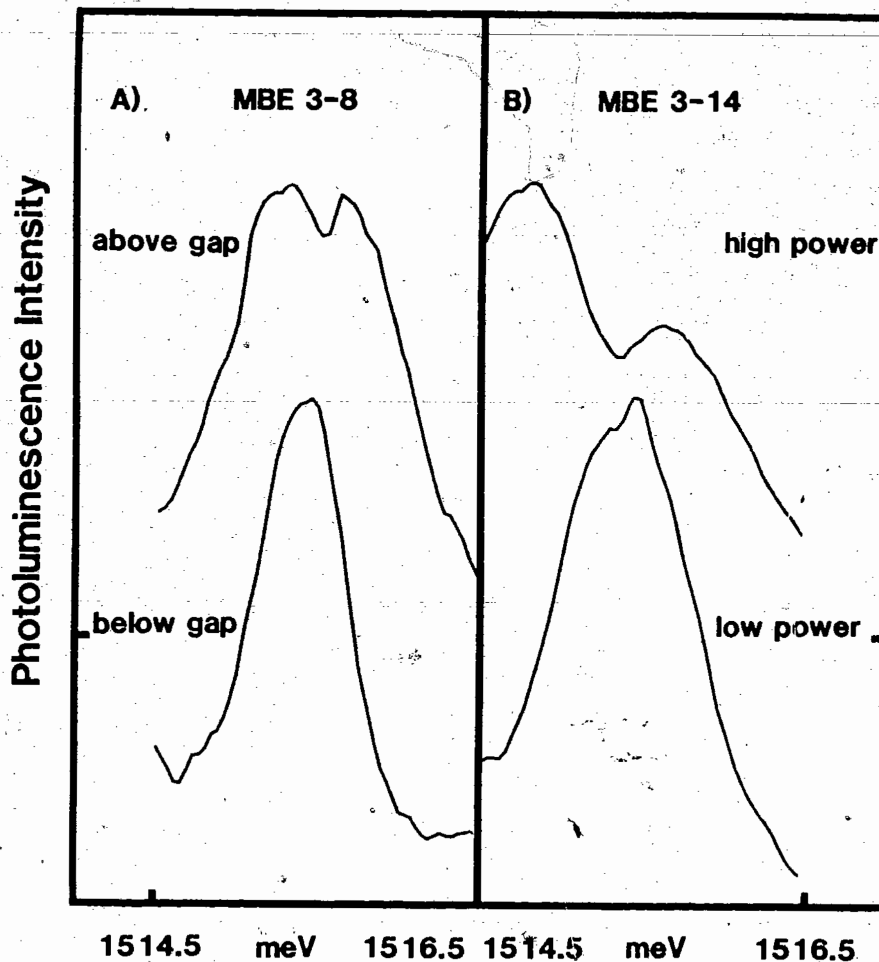

figure 7.3

A) compares the exciton-polariton spectra when the sample was excited by above and below band-gap radiation. The top spectrum was collected while pumping above the gap with an excitation density of ~500 mW/cm² with the sample immersed in superfluid He. The bottom spectrum was collected under identical experimental conditions except that the first excited state of the polariton was resonantly pumped.

B) demonstrates the effect of excitation density on the polariton spectrum. The top and bottom spectra were collected using average excitation densities of 2W/cm² and 200 mW/cm² respectively.

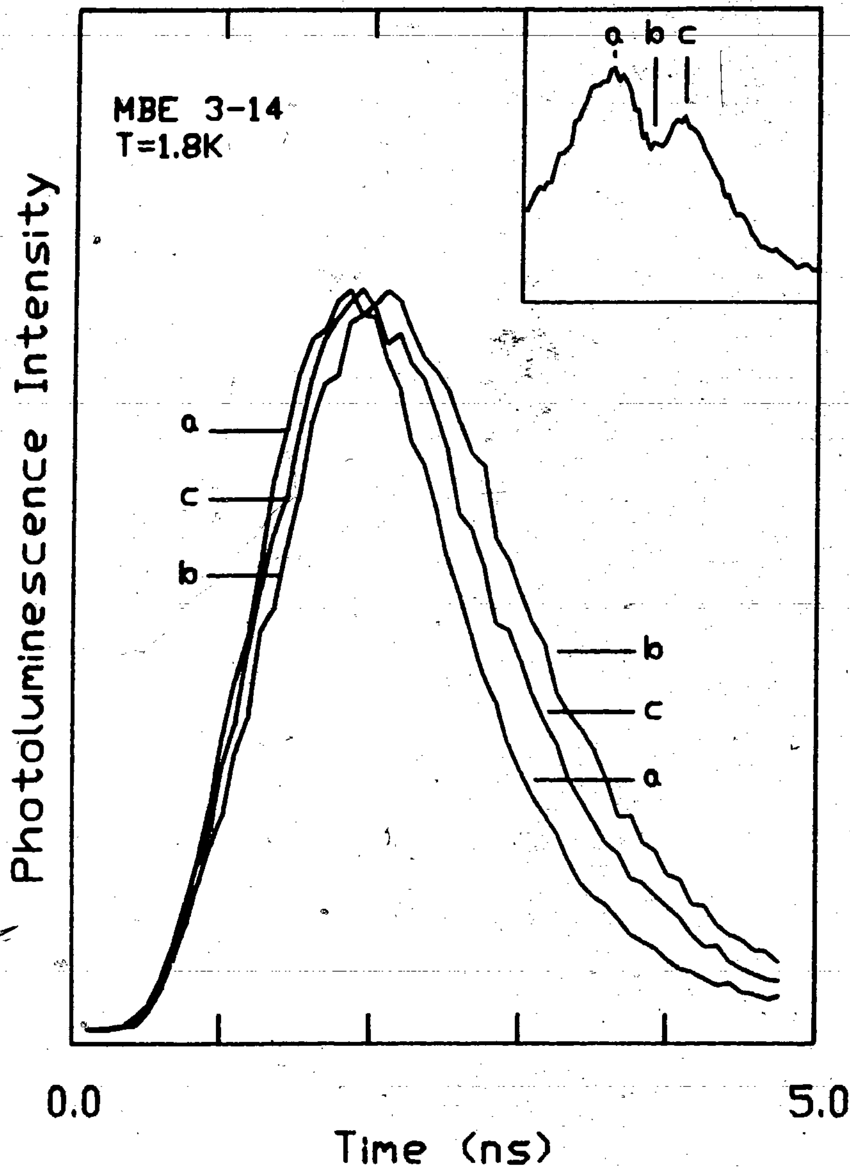

figure 7.4

These traces are the measured, time-dependent photoluminescence curves in the polariton energy region. The top right insert shows the 0.5-1.0 ns spectrum of MBE 3-14 as in figure 7.2, indicating at which energies the three measurements were done. a) below the dip in energy b) at the dip energy c) above the dip in energy

7.4 POLARITON ELASTIC SCATTERING THEORY

The impurity elastic scattering cross section for polaritons can be determined from the bare FE cross section as pointed out by Hopfield [7.17]. Using Fermi's golden rule the differential bare exciton scattering cross section can be written as [7.17]

$$\frac{d\sigma}{d\Omega} = \frac{2\pi}{\hbar v_x} |\langle k'|V|k\rangle|^2 \rho(k') \qquad 7.1$$

where v_x is the mechanical exciton velocity. For elastic, s-wave scattering, the matrix element depends only on the energy of the exciton. The total scattering cross section can thus be written as

$$\begin{aligned} \sigma_x(E) &= \frac{8\pi^2}{\hbar v_x} |\langle E|V|E\rangle|_x^2 \rho_x(E) \\ &= 4|\langle E|V|E\rangle|_x^2 \frac{k_x^2}{\hbar^2 v_x^2} \end{aligned} \qquad 7.2$$

For polariton scattering there are, in general, two bands for a given energy and thus elastic, inter-band scattering is possible. The polariton elastic scattering cross section can be written as

$$\begin{aligned} \sigma_{ri}(E) &= \frac{8\pi^2}{\hbar v_i} |\langle E|V|E\rangle|_p^2 \rho_r(E) \\ &= 4|\langle E|V|E\rangle|_p^2 \frac{k_r^2}{\hbar^2 v_i v_r} \end{aligned} \qquad 7.3$$

Here i and r are the initial and final state band indices. The matrix element, velocity and density of states now correspond to polariton, rather than bare exciton quantities. The polariton group velocity and final density of states

$$\rho(E) = \frac{1}{2\pi^2} \frac{k^2(E)}{\hbar v(E)} \qquad 7.4$$

can be calculated from the dispersion relation (equation 1.63). The polariton scattering matrix element is related to the bare exciton matrix element by

$$|\langle E|V|E\rangle|_p^2 = |\langle E_k|V|E_k\rangle|_x^2 |\phi(r,i)|^2 \qquad 7.5$$

Where $\phi(r,i)$ corresponds to the overlap of the exciton portion of the initial and final state polariton wavefunctions.

$\phi(r,i)$ can be evaluated using Hopfield's [7.1] c parameters [7.18,7.19].

$$\phi(r,i) = C_{i2}^*(E_i,k_i)C_{r2}(E_r,k_r) + C_{i4}^*(E_i,k_i)C_{r4}(E_r,k_r) \qquad 7.6$$

The relevant c parameters [7.1] are

$$C_{12} = \frac{-i\beta(1 + \epsilon_1)}{(\epsilon_1)^{1/2}[(1 - \epsilon_1^2)^2 + 4\beta^2]^{1/2}} \qquad 7.7$$

$$C_{14} = C_{12}\,\frac{(1 - \epsilon_1)}{(1 + \epsilon_1)} \qquad 7.8$$

$$C_{22} = \frac{\beta(1 + \epsilon_2)}{(\epsilon_2)^{1/2}[(1 - \epsilon_2^2)^2 + 4\beta^2]^{1/2}} \qquad 7.9$$

$$C_{24} = C_{22}\,\frac{(1 - \epsilon_2)}{(1 + \epsilon_2)} \qquad 7.10$$

In the above equations

$$\beta = \left[\frac{E_{LT}}{2E_T(0)}\right]^{1/2} \qquad \epsilon_1 = \left[\frac{E_1}{E_T(k_1)}\right]^{1/2} \qquad \epsilon_2 = \left[\frac{E_2}{E_T(k_2)}\right]^{1/2}$$

where E_{LT}, $E_T(k)$, E_1 and E_2 are the longitudinal-transverse energy splitting, the kinetic energy of the uncoupled transverse exciton of wavevector k, the lower branch (LPB) polariton energy and the upper branch (UPB) polariton energy respectively. The overlap squared of the exciton portion of the wavefunction was found to be essentially equal to 1 in the whole region of interest, for both inter and intra-band scattering. The polariton wavefunction is thus almost

completely exciton-like, but its group velocity is not [7.17].

E_k is the kinetic energy of the initial polariton given by $E_k = 1/2 m_x v_i^2$. Equation 7.3 can thus be rewritten as

$$\sigma_{ri}(E) = \sigma_x(E_k)\left(\frac{k_r(E)}{k_x}\right)\frac{v_x^2(E)}{v_r(E)v_i(E)} \qquad 7.11$$

where k_x and v_x are the bare exciton wavevector and velocity, respectively. The matrix element is evaluated for the kinetic energy of the incident polariton. Hence $v_x = v_i$ and equation 7.11 becomes

$$\sigma_{ri}(E) = \sigma_x(\tfrac{1}{2} m_x v_i^2)\left(\frac{k_r(E)}{k_x}\right)\frac{v_i(E)}{v_r(E)} \qquad 7.12$$

Again $k_b(E)$ and $v_b(E)$ are calculated for a given polariton energy and branch using equation 1.63. The transition rates Γ_{ri} are calculated from the above cross sections using

$$\Gamma_{ri}(E) = N_D \sigma_{ri}(E) v_i(E) \qquad 7.13$$

where N_D is the density of scattering centers and $v_i(E)$ is the velocity of the incident polaritons.

Lee et. al. [7.14] have calculated the exciton elastic scattering cross section using partial wave analysis. These results indicated that s-wave scattering is predominant and that neutral donor

scattering is at least an order of magnitude larger than neutral acceptor scattering at all energies. This result is reasonable on physical grounds. Since the donor binding energy in GaAs is much smaller than the acceptor binding energy, the neutral donor wavefunction is much more extended in space, and hence should provide a larger scattering cross section. Using the bare exciton scattering cross section for neutral donors calculated by Lee et. al. [7.14] and equations 7.12-7.13 as well as incident velocities calculated from equation 1.63 results in the transition rates depicted in figure 7.5 for a scattering center density of $10^{16}/cm^3$.

The neutral donor scattering cross section for polaritons obtained by dividing the scattering rate depicted in figure 7.5 by the group velocity, has a peak in the bottleneck region, which, coupled with the smaller group velocity in this energy region, results in a delay in the arrival of these polaritons at the surface. The arrival delay of ballistic polaritons in the dip region due to the reduction in group velocity alone, as might be the case in very lightly doped samples, is beyond the experimental time resolution since the bulk of the initial polariton population is formed within 1 um. In CW luminescence, this creates a dip in the exciton-polariton spectrum of samples with large donor concentrations, since on their slower journey to the sample surface inelastic scattering or trapping mechanisms have more time to depopulate polaritons in this energy region. In time-resolved photoluminescence however, this mechanism can lead to a time dependent dip in more lightly doped samples. At short times more of the faster travelling, less scattered polaritons above and below

the dip energy region reach the surface. At longer times the the more populous polaritons in the dip energy region reach the surface, giving rise to a spectrum more indicative of the population distribution. In these more lightly doped samples, even the polaritons in the dip energy region reach the surface before being inelastically scattered out of this energy region. Unlike the CW luminescence case, the existence of the dip in these samples does not depend on inelastic scattering mechanisms, but on the arrival delay of the dip region polaritons. For very small neutral donor concentrations all the polaritons diffuse rapidly and no dip is observed, even at short time delays. As the excitation density of above band gap light is increased the number of photo-generated free carriers is increased. This screens the Coulomb interaction, hindering polariton formation near the surface. The bulk of the polariton distribution thus ends up further from the sample surface. The observation that the magnitude of the dip increases with increasing excitation density can be qualitatively explained in this way since the centroid of the polariton distribution is now farther from the sample surface and consequently the difference in arrival time at the surface between the dip energy region polaritons and polaritons higher and lower in energy is enhanced. Similarly, below gap excitation, resonantly creating n=2 polaritons, results in an initial distribution closer to the surface since there is now no free carrier screening to hinder polariton formation. Such a distribution, with many more polaritons close to the surface, results in a much reduced arrival delay at the surface of polaritons of all energies. This results in a single peak polariton spectrum, even for

samples having substantial donor concentrations. The effect of the initial distribution on the observed exciton-polariton lineshape has also been studied using CW excitation [7.15].

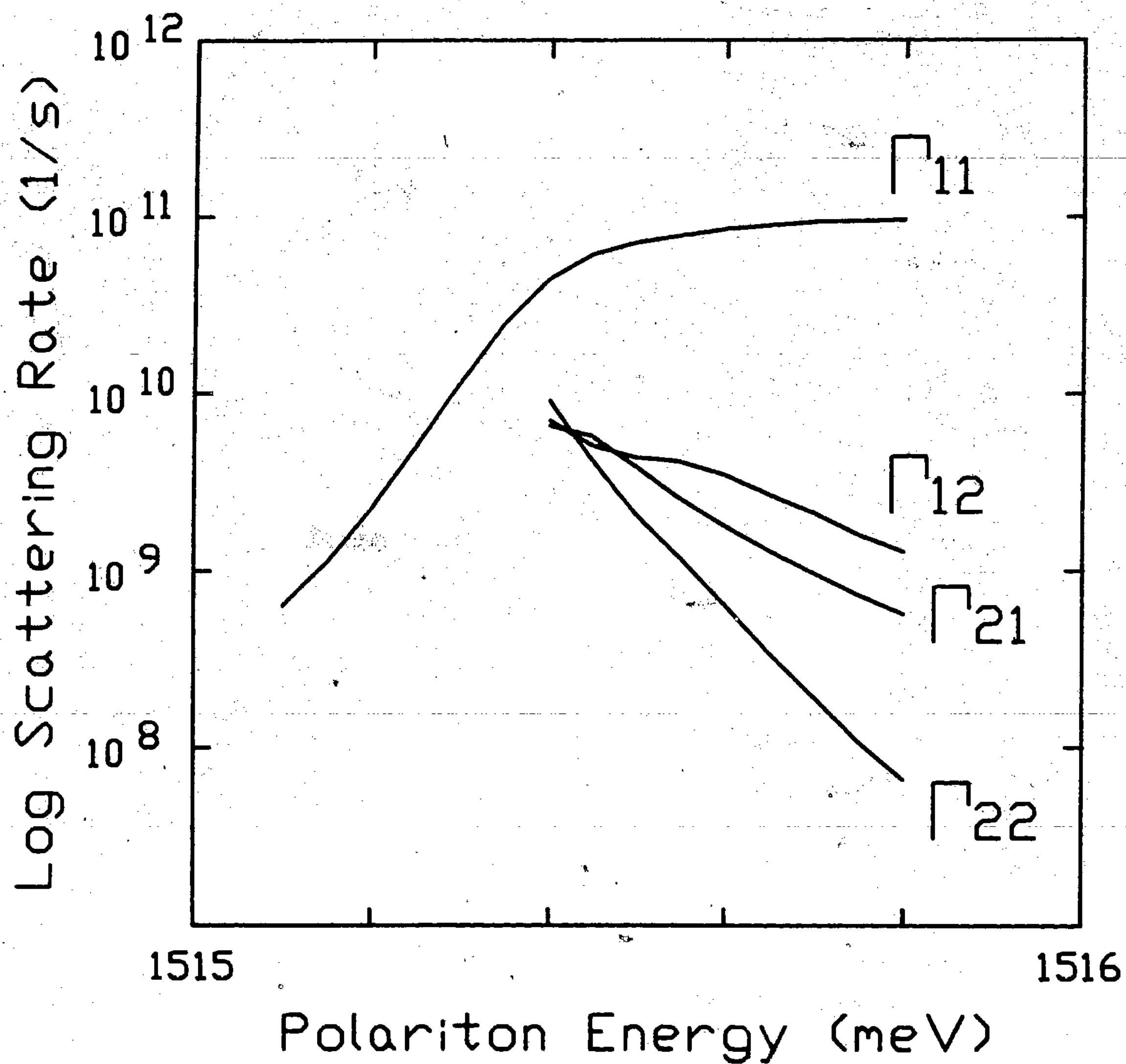

figure 7.5

The scattering rates Γ_{ri} from the initial branch i to the final branch r for a neutral donor concentration of $10^{16}/cm^3$. The indicies 1 and 2 refer to the LPB and UPB respectively.

7.5 BOLTZMANN EQUATION MODEL OF POLARITON LUMINESCENCE

A model of polariton luminescence using a time dependent Boltzmann equation and considering only elastic neutral donor scattering was constructed. This model intrinsically allows for multiple scattering events in contrast to previous treatments of polariton luminescence with neutral donor scattering under CW excitation [7.13-7.15]. The observed photon intensity, I(E,t) is given by the equation

$$I(E,T)d\Omega(E)dE = \sum_{b=1,2} T_b(E,\underline{\Omega})(\underline{v}_b(E,\underline{\Omega})\cdot\underline{\Omega})N_b(x=0,\underline{v}_b(E),t)\,\frac{d\Omega(E)}{n_b^2}dE \qquad 7.14$$

Here b is the branch index, n_b the refractive index calculated from equation 1.63, $T_b(E,\underline{\Omega})$ is the transmissivity of the surface, $\underline{v}_b(E)$ is the polariton group velocity, $N_b(x=0,v_b(E),t)$ is the polariton number density distribution function at the sample surface and $\underline{\Omega}$ is the angular direction of detection.

The transmission function of the LPB decreases rapidly above E_L whereas the transmission of the UPB increases (section 7.6). Luminescence from the energy region above E_L is thus primarily from the UPB. The polaritons of the upper branch, due to their large velocity and small scattering cross section, provide a path whereby LPB polaritons can rapidly escape the crystal if a mechanism for populating the UPB states exists. This scattering mechanism is provided by elastic neutral donor scattering. In a crystal with a

large neutral donor concentration, polaritons, both above and below the dip energy region, have a means of rapidly reaching the sample surface, whereas the dip polaritons are delayed in reaching the surface. This results in a doublet line shape. In samples with lower neutral donor concentrations, dip polaritons reach the surface more easily, while higher energy LPB polaritons cannot easily be scattered to the UPB, hindering their escape from the crystal resulting in a single polariton peak.

As has been pointed out by Travnikov and Krivolapchuk [7.3] for the CW time independent case, the solution of equation 7.14 hinges on calculating the distribution function N at the sample surface. In other words the luminescence problem boils down to a polariton transport problem. Considering only one branch for the moment, the time dependent Boltzmann equation for the distribution function N can be written as

$$\frac{dN(x,\underline{v},t)}{dt} = \int [N(x,\underline{v}',t) - N(x,\underline{v},t)] Q(\underline{v}',\underline{v}) d^3v' - \underline{v}\cdot\nabla_x N(x,\underline{v},t) \qquad 7.15$$

Here $Q(\underline{v}',\underline{v})$ is the scattering rate of polaritons from velocity $\underline{v}$ to velocity $\underline{v}'$. Since only isotropic, elastic pure s-wave scattering will be considered, Q is independent of the directions $Q(\underline{v}',\underline{v}) = \Gamma(E)$. For a semi-infinite crystal only motion perpendicular to the sample surface is important. This allows equation 7.15 to be transformed into a quasi-1-dimensional equation

$$\frac{dN(x,E,\theta,t)}{dt} = \Gamma(E)\int_0^{\pi}[N(x,E,\theta',t)q(\theta,\theta') - N(x,E,\theta,t)q(\theta',\theta)]d\theta - v\cos\theta\,\frac{dN(x,E,\theta,t)}{dx} \qquad 7.16$$

θ is the angle between the direction of polariton propagation and the positive x-axis which points into the crystal. Γ is the scattering rate, while q is the angular dependence of the scattering rate introduced by the geometrical factors resulting from the change in variables. Since only elastic scattering is being considered polaritons of different energies are not coupled by equation 7.16 and hence equation 7.16 can be separately calculated for each energy value. The explicit energy dependence will be dropped from the equation. For s-wave scattering $q(\theta,\theta')$ can be simply evaluated by considering the fraction of the total 4π solid angle represented by the final polariton direction θ. Hence q becomes

$$q(\theta,\theta')d\theta = \frac{2\pi\sin\theta d\theta}{4\pi} = \frac{1}{2}\sin\theta d\theta \qquad 7.17$$

q is no longer symmetric in this space and only depends on the final angle. Equation 7.16 can thus be rewritten in the form

$$\frac{dN(x,\theta,t)}{dt} = \frac{1}{2}\Gamma\sin(\theta)G(x,t) - (\Gamma+1/\tau)N(x,\theta,t) - v\cos(\theta)\,\frac{dN(x,\theta,t)}{dx} \qquad 7.18$$

where $\beta(x,t)$ is given by

$$\beta(x,t) = \int_0^{\pi} N(x,\theta',t)d\theta' \qquad 7.19$$

An energy independent trapping term, corresponding to a pure exponential decay with a phenomenological trapping time τ, has been added to the loss term in equation 7.18. However being energy independent, it cannot change the shape of the observed polariton distribution. Reintroducing the second polariton branch, and allowing for inter-branch scattering changes equation 7.18 into two coupled equations for energies above E_L

$$\frac{dN_1(x,\theta,t)}{dt} = \frac{1}{2}\sin\theta\Big(\Gamma_{12}\beta_2(x,t)+\Gamma_{11}\beta_1(x,t)\Big) - (\Gamma_{11}+\Gamma_{21}+1/\tau)N_1(x,\theta,t) - v_1\cos\theta\,\frac{dN_1(x,\theta,t)}{dx}$$

$$\frac{dN_2(x,\theta,t)}{dt} = \frac{1}{2}\sin\theta\Big(\Gamma_{21}\beta_1(x,t)+\Gamma_{22}\beta_2(x,t)\Big) - (\Gamma_{22}+\Gamma_{12}+1/\tau)N_1(x,\theta,t) - v_2\cos\theta\,\frac{dN_2(x,\theta,t)}{dx} \qquad 7.20$$

where Γ_{ri} is the transition rate from initial branch i to final branch r calcualted from the cross section using equation 7.13. This set of equations was solved numerically, for a number of energies in the polariton region of the spectrum, with different neutral donor

concentrations.

To solve this equation, one needs to assume a reasonable initial distribution function N_o. This initial distribution is completely unknown, but the qualitative results are not greatly dependent on the functional form chosen for the distribution. The spatial distribution should be peaked in the bulk of the sample, with all directions of propagation equally probable, while the energy distribution should be peaked in the knee region. For simplicity, N_o has been assumed to be separable into an energy distribution and a spatial distribution [7.3] given by

$$n(x) = \frac{1}{L_o - L_1}\left(\exp(-x/L_o) - \exp(-x/L_1)\right) \qquad 7.21a$$

Here L_o is the characteristic generation length of free carriers by the incident light and L_1 is the surface recombination length of free carriers due to free carrier traps at the sample surface which deplete the carrier concentration near the surface and hence also the polariton density. A Guassian energy distribution

$$n(E) = \frac{EW}{\sqrt{\pi}} \exp\left(\frac{(E-E_P)^2}{EW^2}\right) \qquad 7.21b$$

peaked at E_P and of width E_W was assumed.

7.6 SURFACE TRANSMISSION FUNCTION

In order to calculate the polariton luminescence from equation 7.14 an expression for the energy and branch dependent transmission function is needed. The existence of the two polariton branches complicates the calculation of the transmission function since the Fresnel equations no longer provide sufficient boundary conditions. Additional boundary conditions (ABC) must be supplied [7.20]. Following Askary and Yu [7.4,7.19] the transmission and reflection coefficients have been calculated using the Pekar ABC [7.21]. The generalized reflection coefficient is given by

$$R_{m}^{m'} = |\underline{x}\cdot\underline{S}_{m'}/\underline{x}\cdot\underline{S}_{m}| \qquad 7.22$$

where $\underline{S}$ is a generalized Poynting vector appropriate for polaritons and $\underline{x}$ is a unit vector perpendicular to the surface. m is the initial branch index and m' is final branch index. $m'=m$ corresponds to pure reflection into the same branch while $m'=0$ corresponds to tranmission into external photons. For the external photons the Poynting vector is given by [7.22]

$$\underline{S}_{o} = \frac{c^2}{8\pi\omega} |\mathcal{E}_{o}|^2 \underline{k}_{o} \qquad 7.23$$

For the polaritons there is an additional mechanical contribution from

the partial exciton nature to the Poynting vector [7.19]. Thus for LPB polaritons the Poynting vector is given by

$$\underline{S}_1 = \frac{c^2}{8\pi\omega} |\mathcal{E}_1|^2 \mathrm{Re}\{\underline{k}_1\}(1 - \chi_1/\chi_2) \qquad 7.24$$

and the UPB Poynting vector is

$$\underline{S}_2 = \frac{c^2}{8\pi\omega} |\mathcal{E}_2|^2 \mathrm{Re}\{\underline{k}_2\}(1 - \chi_2/\chi_1) \qquad 7.25$$

where $\chi_1 = (n_1^2 - \epsilon_o)$ is the polarizability. For simplicty the polarization of the polaritons was taken to lie always in the plane of the interface thus allowing this simplified problem to be solved without keeping track of a population of longitudinal excitons. Consider a LPB wave polarized in the plane of the interface incident on the surface. The continuity of the tangential component of $\mathcal{E}$ across the interface gives the condition

$$\mathcal{E}_o = \mathcal{E}_1 + \mathcal{E}_{1R} + \mathcal{E}_2 \qquad 7.26$$

where $\mathcal{E}_{1R}$ is the electric field of the component reflected back into the LPB. The continuity of the tangential component of H gives

$$k_o\cos\theta_o = k_1\cos\theta_1(\mathcal{E}_1 - \mathcal{E}_{1R}) - k_2\cos\theta_2 \qquad 7.27$$

The Pekar ABC [7.21] which states that the vector sum of the polarizations at the interface should be zero yields the final condition

$$(n_1^2-\epsilon_o)(\mathcal{E}_1+\mathcal{E}_{1R}) + (n_2^2-\epsilon_o)\mathcal{E}_2 = 0 \qquad 7.28$$

The angles in equation 7.27 are found from Snell's law

$$k_o\sin\theta_o = k_1\sin\theta_1 = k_2\sin\theta_2 = k_{1R}\sin\theta_{1R} \qquad 7.29$$

Defining $q_o=k_o\cos\theta_o$ ect., $a=\mathcal{E}_o/\mathcal{E}_1$, $b=\mathcal{E}_{1R}/\mathcal{E}_1$ and $c=\mathcal{E}_2/\mathcal{E}_1$ allows equations 7.26-7.28 to be written as

$$\begin{aligned} a &= 1 + b + c \\ q_o a &= q_1(1-b) - q_2 c \\ \chi_1(1+b) &+ \chi_2 c = 0 \end{aligned} \qquad 7.30$$

with solution

$$a = \frac{2q_1(1 - \chi_2/\chi_1)}{[q_2 - q_1\chi_2/\chi_1 + q_0(1 - \chi_2/\chi_1)]}$$

$$b = \frac{-q_2 - q_0(1 - \chi_2/\chi_1) - q_1(\chi_2/\chi_1)}{[q_2 - q_1\chi_2/\chi_1 + q_0(1 - \chi_2/\chi_1)]} \qquad 7.31$$

$$c = \frac{2q_1}{[q_2 - q_1\chi_2/\chi_1 + q_0(1 - \chi_2/\chi_1)]}$$

The squares of these coeficients, when substituted in equations 7.23-7.25 and subsequently in equation 7.22, gives the probability of transmission as a photon or reflection as a polariton into one of the two branches. Care must be taken when evaluating the squares of these coefficients since the q coefficients can be complex depending on the energy region and the angles. The calculated generalized reflection coefficients for normal incidence are displayed in figure 7.6

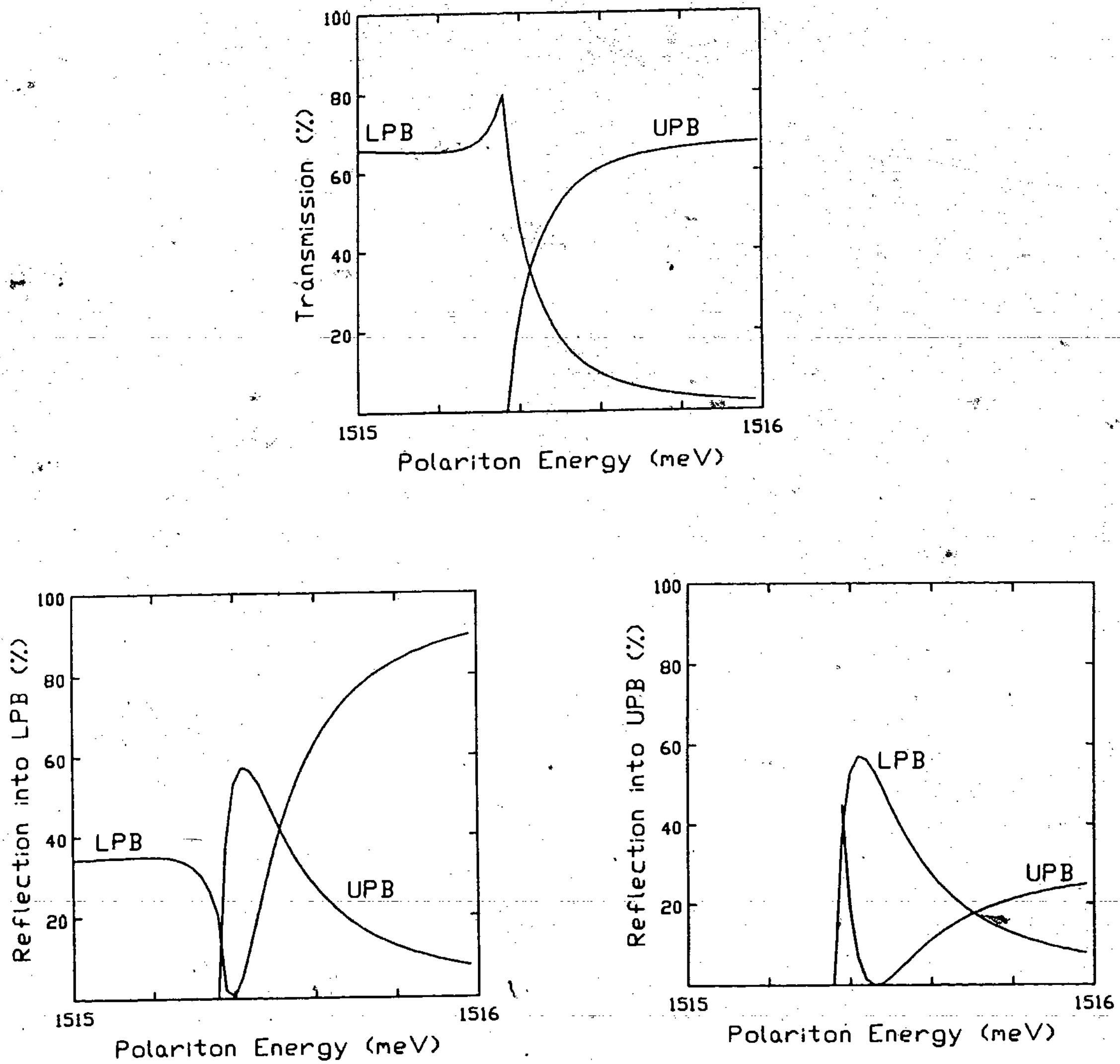

figure 7.6

a) is the percent of the incident polaritons of normal incidence transmitted as external photons using the Pekar ABC

b) is the percent of the incident polaritons of normal incidence reflected into the LPB

c) as b) but reflected into the UPB

7.7 DETAILS OF THE NUMERICAL SOLUTION OF THE BOLTZMANN EQUATION

Equations 7.20 can be written in finite difference form and solved numerically. At the interface the UPB and LPB distributions must be adjusted for those polaritons which are reflected (section 7.5). The chosen time increment must be small enough to avoid instabilities in the solution. Instabilities can arrise if for example the time increment is long enough that particles beyond the nearest neighbour cell can reach the current cell. To avoid this situation the following condition on the spatial and time increments must be satisfied

$$\frac{v\Delta t}{\Delta x} < 1 \qquad 7.32$$

In this case v is the maximum polariton velocity within the energy range of interest. Similarly the time increment must not be so long as to allow more than a small fraction, say 5%, of the total number of polaritons within a cell to be scattered during one time increment. For neutral donor scattering center densities not exceeding 10^{15} equation 7.32 represents the more restrictive condition.

The proceedure for evaluating equations 7.20 is as follows. First the wavevectors and velocities of both polariton branches are calculated from equation 1.63 for the current energy (only for the LPB if $E<E_L$). The surface transmission and reflection coefficients for all angles are calculated next followed by the transition rates Γ for

the current energy. Next the initial distribution is calculated and then allowed to evolve in time in accordance with equations 7.20. For each time increment the number of polaritons transmitted through the surface is saved, thus building up a decay curve for that particular energy. This is then repeated for the next polariton energy until decay curves have been calculated for the whole polariton spectrum. A series of time-resolved spectra, for comparison with experiment, are then generated by convoluting these calculated luminescence curves with a realistic instrument response and summing the luminescence for the duration of the desired time windows. The results for three different neutral donor concentrations are depicted in figure 7.7. The parameters used to generate these spectra are:

$m_{ex} = 0.55m_o$

$\epsilon_o = 12.8$

$E_{LT} = 0.07$ meV

ET = 1515.3 meV

EP = 1515.35 meV

EW = 0.5 meV

$L_o = 1.0$ um

$L_1 = 0.25$ um

L_o was set to the approximate above band gap absorption length of GaAs while L_1 was arbitrarily set to 0.25 um, a value which produced results resembling the experimental observations in figure 7.2.

7.8 DISCUSSION OF EXPERIMENTAL AND MODEL RESULTS

It is clear that the polariton spectrum depends drastically on the initial population distribution of polaritons. If the surface recombination length L_1 were reduced then there would be a decreased time dependent dip, since there would be a greater number of polaritons of all energies at the surface, leading to instantaneous luminescence at all polariton energies. The polariton spatial distribution would also have a large effect in CW photoluminescence, since a short surface recombination length would reduce the time available for the inelastic scattering mechanisms to reduce the number of dip energy region polaritons reaching the surface. The effects of surface preparation [7.16,7.23] on the luminescence spectrum can be explained in this way. Cleavage of a GaAs sample in ultra high vacuum [7.23] causes a disappearance of the dip during luminescence measurements, although subsequent exposure to air reestablishes the dip. This effect can easily be explained, as was done by the authors, by invoking surface states. Since the number of surface traps after cleavage in UHV is far less, L_1 will be decreased. The important effect of the spatial distribution of polaritons was also realized by Weisbuch and Ulbrich [7.10] in the interpretation of their experimental results. The effect of surface electric field on the polariton line shape [7.16] can also be interpreted along these lines. The observed dip increases with increasing electric field [7.16]. The surface field separates the photo generated holes and electrons hindering polariton formation in the surface region. This would serve

to increase L_1 by a different mechanism, but with the same final result of increasing the distance to the surface for all polaritons, and hence allowing increased scattering for those in the bottleneck energy region. Schultheis and Tu [7.16] have however argued that their results should be interpreted as arising due to an electric field modified polariton resonance near the surface. Our experimental results show that this mechanism is not applicable in our samples. Figure 7.3b shows the disappearance of the dip with decreased excitation power. Their proposed mechanism would predict the opposite, since an increase in excitation density would generate more free carriers which would discharge the deep surface traps responsible for the surface electric field, resulting in a reduced dip.

The results of the Boltzmann equation model do not exactly reproduce the experimental spectra. The main reason for the discrepancy is the omission of inelastic scattering processes in the model. This is not a rigorously justifiable simplification since inelastic scattering processes tend to repopulate those polaritons below the bottleneck, and in the UPB, which rapidly exit the crystal. The omission of these processes results in the calculated peaks being too narrow at long times, particularly for the low donor concentration case. Furthermore, with only elastic scattering, the single peak polariton spectrum is established after long enough delays regardless of the neutral donor concentration since elastic scattering can only delay the arrival time of the polaritons at the surface, but not redistribute the population. A complete theory would also require a more realistic initial energy distribution, calculated using inelastic

scattering rates. Nevertheless, these results clearly illustrate the important effect of elastic neutral donor scattering on the time evolution of the exciton-polariton photoluminescence lineshape of GaAs. We would like to reiterate however, that polariton luminescence is a complicated transport problem with non-trivial boundary conditions. Consequently, any mechanism that affects the initial distribution either in space or in energy, the transport of the polaritons in the crystal, or the nature of the crystal boundary itself can affect the experimentally observed polariton spectrum. Thus no single mechanism can explain the huge variety of observed polariton spectra in different crystals. It is clear however that a comprehensive theory of polariton luminescence must include the effect of elastic scattering from neutral impurities.

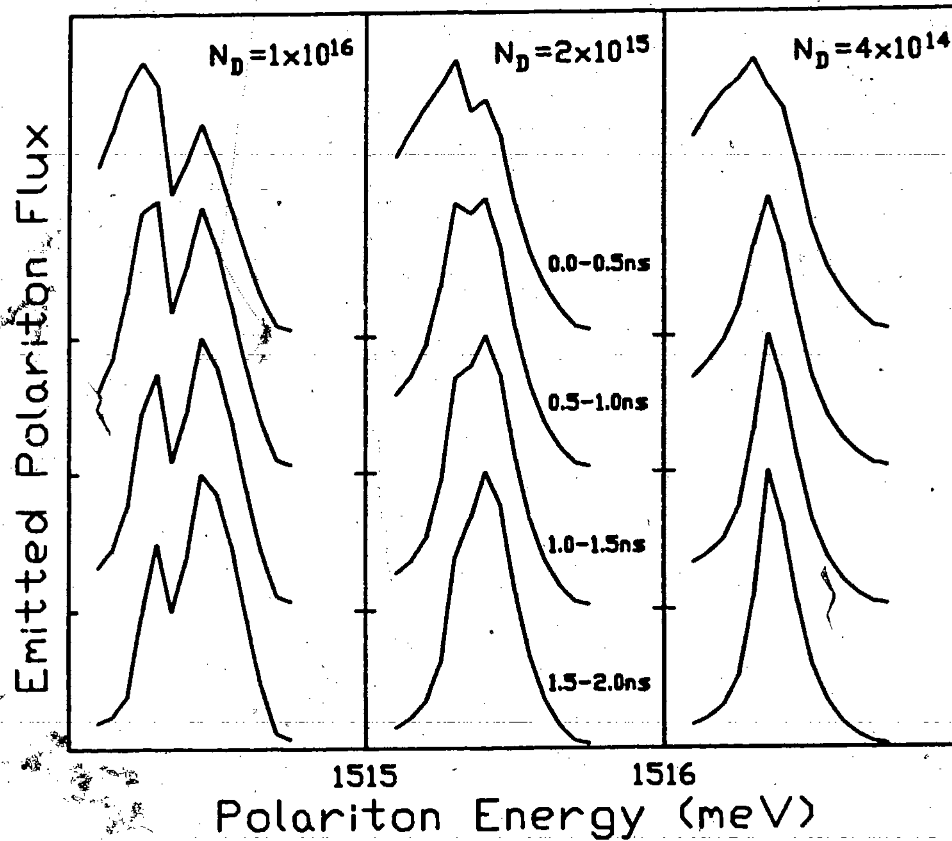

figure 7.7

A series of time-resolved spectra generated by the Boltzmann equation model using identical parameters except for the neutral donor concentration. A) $N_D=10^{16}/cm^3$ B) $N_D=2\times10^{15}/cm^3$ C) $N_D=4\times10^{14}/cm^3$.

APPENDIX 1: ACTIVE STABILIZATION OF THE MODELOCKER

As discussed in section 2.3, reliable modelocking requires that a good standing wave be established in the modelocking crystal. This means that the crystal should have an acoustic resonance at exactly one half of the laser repetition frequency. The acoustic resonance is a sensitive function of temperature and consequently the modelocking crystal is surrounded by a temperature controlled oven. Nevertheless, the subsequent application of RF drive at the acoustic resonance frequency at a power comparable to that of the oven heater causes additional heating of the crystal changing the resonance frequency. Optimally adjusting such a system to operate at the required frequency is a difficult task, requiring tedious tweaking of controls. The situation can be drastically improved by actively tracking the crystal acoustic resonance by controlling the RF drive level [A.1]. This method relies on the fact that the phase of the reflected RF wave changes by a factor of π upon going through the crystal resonance. Right at the resonance frequency the phase difference between the incident and reflected waves is $\pi/2$. Figure A1.1 is a block diagram of the stabilization circuit. The source of the RF is a highly stable frequency synthesized tunable oscillator. The output of this oscillator is amplified and then split into two parts. The RF level of one of these components is controlled by a DC level set either manually or by the feedback loop, then further amplified and sent to the modelocker head. The other component is compared in a balanced mixer with the reflected RF picked off by a uni-directional coupler.

The output of the balanced mixer, with two identical frequency signals as input, is a DC level whose sign and magnitude depend on the phase difference between the input signals. For a phase difference of $\pi/2$, corresponding to resonance, the DC signal is zero. The path lengths of the lines leading to the balanced mixer must be adjusted so that the phase difference at the mixer corresponds to the actual phase difference between the reflected and incident waves at the modelocker head. The output DC level of the mixer also depends on the intensity of the input waves. The intensity of the reflected wave goes through a minimum at the crystal resonance since most of the incident power is then absorbed. To remove this unwanted influence on the DC output of the mixer the output of the uni-directional coupler is amplified by an amplifier whose gain is saturated even for the lowest level of reflected power. The intensity of the reflected signal applied to the mixer is thus independent of the frequency and thus the output of the mixer depends only on the phase difference. This phase error signal can then be used to adjust the amount of RF drive to the modelocker head, thus controlling the crystal temperature and hence its resonance frequency. This system is now very easy to use. First one flicks the switch from lock to manual, disengaging the feedback loop. Then one tunes the RF oscillator to a crystal resonance which is easily recognized by a minimum in the reflected power and a rapid change in the phase error signal both of which are displayed on meters. Once a resonance close to the desired operating frequency of ~42 MHz is found, the switch is set to 'lock' and the RF drive level is now automatically adjusted so that the crystal resonance frequency is

locked to the drive frequency. The frequency of the RF source can now be adjusted until optimum modelocking occurs as determined by the autocorrelator (section 2.8) without fear of losing the acoustic resonance, provided the tuning is done gradually so as to allow for the time needed to heat the modelocking crystal. Practically, the frequency can be changed to the correct modelocking frequency during the span of a few seconds. The RF power level delivered to the crystal once the driving frequency has been set to the desired modelocking frequency can be increased (decreased) by decreasing (increasing) the power supplied to the heater.

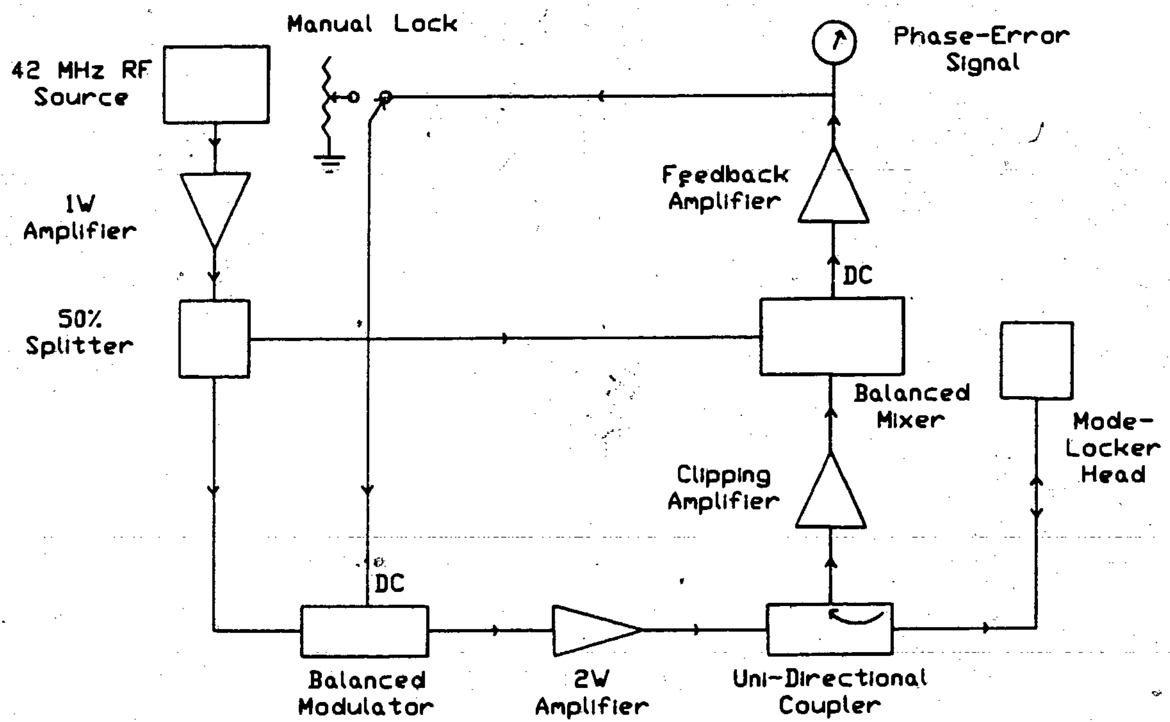

Figure A1.1

Block diagram of modelocker stabilization circuit

APPENDIX 2: TRAILING PULSE SUPPRESSOR

The typical trailing pulse suppression of 500:1 provided by an optimally adjusted cavity dumper can be improved by following the cavity dumper with a Pockels cell and a polarizer as discussed in section 2.5 to yield a further factor of 100 rejection. The Pockels cell used here (lasermetrics EOM 3078) requires about 300 volts for a $\pi/2$ rotation of the electric field vector of light in the visible region. The Pockels cell modulator has its output polarizer adjusted for maximum transmission with the full potential applied to the modulator. Since the transmission must be cut off before the first trailing pulse arrives at the modulator the electronics must discharge the charge on the capacitor formed by the plates of the modulator in less than 12 ns. The electronics must also be able to hold the potential at zero for approximately 30 ns to suppress the first three or four trailing pulses which were found to be considerably stronger than later ones. The Pockels cell plates can then be recharged through a resistor until full transmission is restored. This last process can proceed at a moderate rate since the maximum repetition rate of the cavity dumper is 4 MHz, thus allowing about 200 ns for recharging. The charging resistor must be small enough so that the charging process is essentially complete in less than 200 ns yet large enough to keep the power dissipation in the resistor and the current through the active device during the cutoff phase at a manageable level. A switching device capable of handling these requirements is the high-speed, high-voltage field effect transistor IVN6000CNU made by Intersil which

can switch 500V in less than 10 ns.

The schematic diagram for the trailing pulse suppressor circuit is presented in figure A2.1. While the input voltage to the trigger input is at a TTL zero level, the FET is off and the charging resistor R holds the Pockels cell at the half-wave potential provided at the high voltage terminal. A TTL 1 level of 40 ns duration generated by an external variable delay circuit connected to the cavity dumper synch output is buffered by the two halves of a 74S140 line diver followed by four halves of two National DS0026 high speed clock drivers connected in parallel. This high gate drive capability is needed to turn the FET on quickly enough in face of the large dV/dt at the drain. The circuit uses R = 1KΩ 50 W which corresponds to a power dissipation of 39 W at a repetition rate of 4 MHz with a high voltage supply of 300V at 130 mA.

The entire circuit is contained in a small aluminum box mounted directly on the Pockels cell with a thin intervening layer of thermal insulation. The terminals of the Pockels cell enter the box via a small hole and the drain and source leads of the FET are connected directly to them, with the FET heat sinked to the inside surface of the box. To prevent oscillation, it is necessary to keep all leads very short and shield the input circuitry from the FET. A small muffin tin fan mounted on the top cools the FET and the charging resistor. The electrical shielding provided by the box is such that a sensitive photon counting apparatus can be operated near the modulator with no interference. The operation of the circuit is demonstrated in figure A2.2, which shows the log of the transmission of a continuous laser

beam vs. time for a repetition rate of 4 MHz.

In normal operation, the modulator and polarizer are placed about 30 cm from the output of the cavity dumper, where the waist in the output beam guarantees easy passage through the ~2 mm modulator aperture. Two beamsplitters placed before and after the modulator are used to monitor the beam using fast photodiodes. The required half-wave voltage is applied and the circuit is allowed to run for about 5 minutes at the selected repetition rate so that the modulator can equilibrate. With the cavity dumper properly adjusted, the delay circuit is adjusted so that the FET is fired just before the main output pulse, and the Pockels cell angles and polarizer angle are then adjusted for minimum transmission through the modulator. Then by monitoring the photodiode before the modulator the cavity dumper delay setting is misadjusted to make the first trailing pulse stronger than the desired pulse. Monitoring the second photodiode, the Pockels cell delay is set to fire the transistor between the desired pulse and the first trailing pulse, maximizing the intensity of the first and minimizing the latter. Small adjustments in the Pockels cell angles may further reduce the intensity of the trailing pulse, completing the adjustment of the Pockels cell modulator. Finally, the cavity dumper is readjusted to its proper operating settings by monitoring the signal before the modulator.

The results as observed on a high speed photon counting system are shown in figure 2.1. The top curve represents the output of our cavity dumper when it is very well adjusted, but even at this rejection ratio of ~800 the trailing pulses are quite noticeable. In

the bottom curve the Pockels cell modulator has been added and the rejection ratio for the first two trailing pulses has been increased to $\sim 6 \times 10^4$, making them almost invisible in the dark-count noise. The suppression of the third trailing pulse is not as great since the Pockels cell has by this time started to recharge.

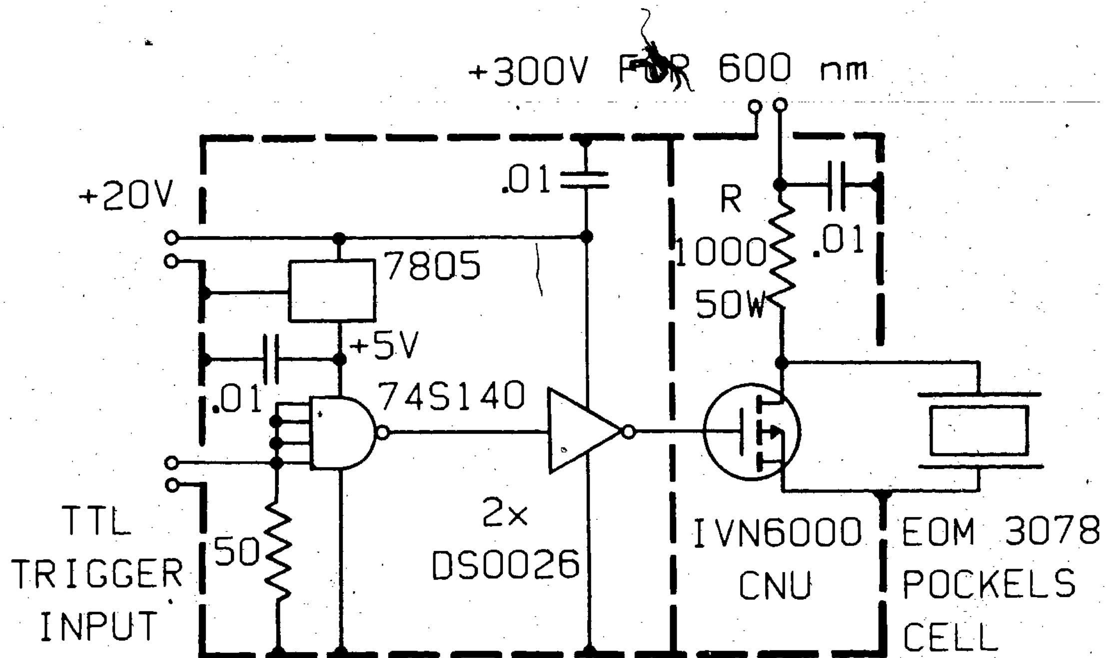

Figure A2.1

Pockels cell driver circuit diagram. The circuit is enclosed in a ventilated aluminum shielding box indicted by the dashed lines. The FET transistor is heat-sinked to this box. Capacitors are in microfarads and resistors in ohms.

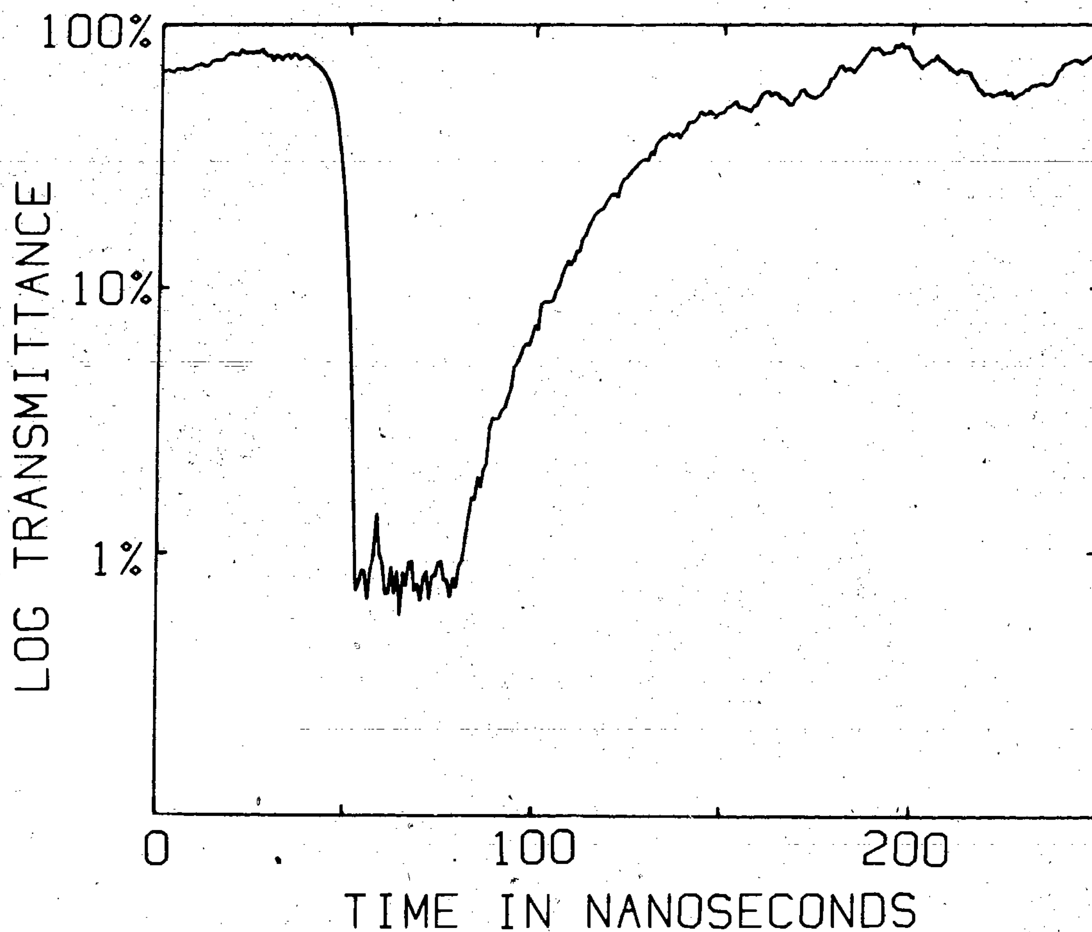

Figure A2.2

Log transmission of the modulator for a continuous 600 nm laser beam and a modulator repetition rate of 4 MHz, as determined by a fast photon-counting detection system.

APPENDIX 3: DECONVOLUTION USING THE SIMPLEX ALGORITHM

If the luminescence decay time is of the same order of magnitude as the response time of the detector, the observed decay corresponds to the true luminescence decay convoluted with the instrument response. In order to extract a meaningful lifetime in this circumstance it is necessary to deconvolute the measured decay with an instrument response measured at the same wavelength as the observed luminescence. In theory it is possible to deconvolute using Laplace transforms, but in practice this is very difficult with experimental data. The usual procedure is to guess a functional form of the solution, usually a sum of exponential components, estimate the parameters and then convolute this theoretical decay curve with the instrument response and compare with the observed data. By evaluating the sum squared error between the trial solution and the experimental data the suitability of the trial parameters is determined. In order to arrive at meaningful values for the parameters a non-linear fitting procedure must be used which adjusts the trial parameters until a good fit is obtained.

A powerful and simple algorithm for the minimization of an arbitrary function is the simplex algorithm [A.2,A.3]. The best deconvolution corresponds to minimizing the sum squared error function. This function can be pictured as a single valued N dimensional hypersurface where N is the dimension of the space corresponding to the number of adjustable parameters. The term 'simplex' refers to an N+1 dimensional geometric figure constructed

out of the trial solution and the additional N vertices formed from the trial solution by adding sequentially to each parameter an increment. The algorithm then proceeds to move and shrink the simplex towards the minimum of the hypersurface by always moving the worst vertex, i.e. the one with the largest summed squared error, according to a simple set of geometrical instructions. This simplex method does not require the calculation of any derivatives yet is almost as fast as the steepest decent method. It can handle an arbitrary number of adjustable parameters and never suffers from instabilities. An additional advantage of the simplex algorithm is its remarkable compactness compared to other minimization methods, allowing it to be readily programmed on any microcomputer. Since derivatives are not required the summed squared error surface need not be differentiable. Boundary conditions can thus easily be handled by just assigning very large summed squared error values for parameters in the forbidden region.

The program written to accomplish the deconvolution can handle 1-3 exponential decays with or without an exponential buildup term. Each exponential decay component is however limited to having the same buildup time constant as the others. A time-shift parameter is also included to take care of any time shift between the experimental data and the measured instrument response. Such a shift can easily be present since the data and instrument response are generally collected using different optical paths. A path length difference of only 3 mm corresponds to a time shift of 10 ps which is just barely significant given the available time resolution. Lifetimes down to a limit of 30

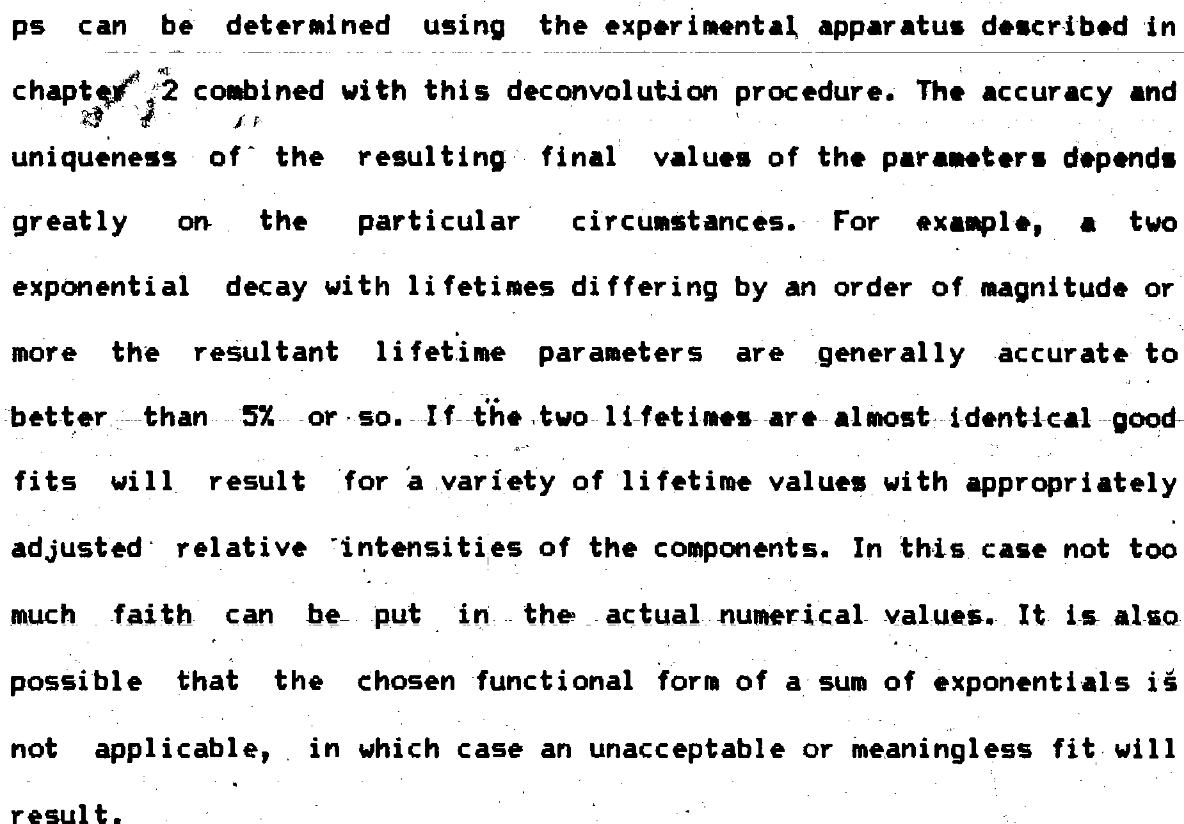

ps can be determined using the experimental apparatus described in chapter 2 combined with this deconvolution procedure. The accuracy and uniqueness of the resulting final values of the parameters depends greatly on the particular circumstances. For example, a two exponential decay with lifetimes differing by an order of magnitude or more the resultant lifetime parameters are generally accurate to better than 5% or so. If the two lifetimes are almost identical good fits will result for a variety of lifetime values with appropriately adjusted relative intensities of the components. In this case not too much faith can be put in the actual numerical values. It is also possible that the chosen functional form of a sum of exponentials is not applicable, in which case an unacceptable or meaningless fit will result.

REFERENCES

1.1 G.H. Wannier, Phys. Rev. 52, 191 (1937)

1.2 W.A Harrison, Solid State Theory (Dover, New York 1980) P.140

1.3 M.A. Lampert, Phys. Rev. Lett. 1, 450 (1958)

1.4 J.J. Hopfield in Proc. Intern. Conf. Phys. semicond., paris 1964 (Dunod, paris 1964) P.725

1.5 J.R. Haynes, Phys. Rev. Lett 4, 361 (1960)

1.6 P.J. Dean and D.C. Herbert in Excitons ed. by K. Cho (Springer, Berlin 1979)

1.7 E.I. Rashba and G.E. Gurgenishvili, Sov. Phys. Solid State 4, 759 (1962)

1.8 E.I. Rashba Sov. Phys. Semicond. 8, 807 (1975)

1.9 J.D. Jackson, Classical Electrodynamics (Wiley, New York 1975) P.284

1.10 L.I. Schiff, Quantum Mechanics (McGraw Hill, New York 1968) P.397

1.11 W. Demtröder, Laser Spectroscopy (Springer, Berlin 1982) P.13

1.12 D.L. Dexter in Solid State Physics vol.6 ed. by F. Seitz and D. Turnbull (Academic Press, New York 1858) P.359

1.13 C.H. Henry and K. Nassau, Phys. Rev. B4, 1628 (1970)

1.14 W. Demtröder, Laser Spectroscopy (Springer, Berlin 1982) P.33

1.15 P.M. Morse and H. Feshbach, Methods of Theoretical Physics (McGraw Hill, New York 1953) Sec.7.2

1.16 D.F Nelson, J.D. Cuthbert, P.J. Dean and D.G. Thomas, Phys. Rev. Lett. 17, 1262 (1966)

1.17 P.J. Dean, R.A. Faulkner, S. Kimura and M. Ilegems Phys. Rev. B4, 1926 (1971)

1.18 W. Schmid, Phys. Status Solidi B 84, 529 (1977)

1.19 G.C. Osbourn and D.L. Smith, Phys. Rev. B16, 5426 (1977)

1.20 F.A. Riddoch and M. Jaros, J. Phys. C 13, 6181 (1980)

1.21 M. Jaros, F.A. Riddoch and Lu Da Lian, J. Phys C 16, L733 (1983)

1.22 P.J. Dean, J.D. Cuthbert, D.G. Thomas and R.T. Lynch, Phys. Rev. Lett. 18, 122 (1967)

1.23 D.G. Thomas and J.J. Hopfield, Phys. Rev. 128, 2135 (1962)

1.24 J.J. Hopfield, Phys. Rev. 112, 1555 (1958)

1.25 Y. Toyozawa, Prog. Theor. Phys. Suppl. 12, 111 (1959)

1.26 U. Heim and P. Wiesner, Phys. Rev. Lett. 30, 1205 (1973)
P. Wiesner and U. Heim, Phys. Rev. B11, 3071 (1975)

1.27 F. Askary and P.Y. Yu, Phys. Rev. B31, 6643 (1985)

1.28 R.G. Ulbrich and G.W. Fehrenbach, Phys. Rev. Lett. 43, 963 (1979)

1.29 V.V. Travnikov and V.V. Krivolapchuk, Sov. Phys. JETP 58, 1210 (1983)

1.30 H.B. Bebb and E.W. Williams in Semiconductors and Semimetals vol.8 ed. by R.K. Willardson and A.C. Beer (Academic Press, New York 1972) P. 335

1.31 J.I. Pankove, Optical Processes in Semiconductors (Prentice-Hall, Englewood Cliffs, N.J. 1971) P.133

2.1 D. von der Linde in Ultrashort Light Pulses edited by S.L. Shapiro (Springer, Berlin 1977) P.204

2.2 C.H. Henry and K. Nassau, Phys. Rev. B4, 1628 (1970)

2.3 W. Demtröder, Laser Spectroscopy (Springer, Berlin 1982) P.557

2.4 O. Svelto, Principles of Lasers (Plenum, New York 1982) P.188

2.5 A. Yariv, Quantum Electronics (Wiley, New York 1975) P.262

2.6 W. Demtröder, Laser Spectroscopy (Springer, Berlin 1982) P.549

2.7 D.J. Bradley in Ultrashort Light Pulses edited by S.L. Shapiro (Springer, Berlin 1977) P.17

2.8 D. von der Linde, J. Kuhl and E. Rosengarten, J. Lumin. 24,25, (1981)

2.9 D. Rosen, A.G. Doukas, Y. Budansky, A. Katz and R.R. Alfano, Appl. Phys. Lett. 39, (1981)

2.10 M. Jorgensen and J.M. Hvam, Appl. Phys. Lett. 43, (1983)

2.11 D.J. Bradley in Ultrashort Light Pulses edited by S.L. Shapiro (Springer, Berlin 1977) P.25

2.12 M.C. Adams, W.Sibbett and D.J. Bradley, Opt. Commun. 26, (1978)

2.13 F. Heisel, J.A. Miehe and B. Sipp, Rev. Sci. Instrum. 52, (1981)

2.14 I. Yamazaki, N. Tamai, H. Kume, H. Tsuchiya and K. Oba, Rev. Sci. Instrum. 56, 1187 (1985)

2.15 Ultrashort Light Pulses edited by S.L. Shapiro (Springer, Berlin 1977)

2.16 Picosecond Phenomena 3, edited by K.B. Eisenthal, R.M. Hochstrasser, W. Kaiser and A. Laubereau (Springer, Berlin 1982)

2.17 A. Yariv, Quantum Electronics (Wiley, New York 1975) P.133

2.18 A. Yariv, Quantum Electronics (Wiley, New York 1975) P.256

2.19 O. Svelto, Principles of Lasers (Plenum, New York 1982) P.188

2.20 W. Demtröder, Laser Spectroscopy (Springer, Berlin 1982) P.549

2.21 D.J. Bradley in Ultrashort Light Pulses edited by S.L. Shapiro (Springer, Berlin 1977) P.57

2.22 C.P. Ausschnitt, R.K.Jain and J.P. Heritage, IEEE J. Quantum Electron. 15, (1979)

2.23 R.L. Fork, B.I. Greene and C.V. Shank, Appl. Phys. Lett. 38, (1981)

2.24 C.V. Shank, R.L. Fork and R.T. Yen, in Picosecond Phenomena 3, edited by K.B. Eisenthal, R.M. Hochstrasser, W. Kaiser and A. Laubereau (Springer, Berlin 1982)

2.25 A. Yariv, Quantum Electronics (Wiley, New York 1975) P.356

2.26 Spectra Physics model 344S Cavity Dumper manual

2.27 EG&G Ortek model 457 Time-to-Amplitude-converter data sheet

2.28 A. Hallam and R.E. Imhof, J. Phys. E 13, (1980)

2.29 G.R. Haugen, B.W. Wallin and F.E. Lytie, Rev. Sci. Instrum. 50, (1979)

2.30 E.P. Ippen and C.V. Shank in Ultrashort Light Pulses, edited by S.L. Shapiro (Springer, Berlin 1977) P.83

2.31 D.J. Bradley and G.H.C. New, IEEE Proceedings 62, 313 (1974)

2.32 A. Yariv, Quantum Electronics (Wiley, New York 1975) P.407

3.1 W. Schmid, Phys. Status Solidi B 84, 529 (1977)

3.2 G.C. Osbourn and D.L. Smith, Phys. Rev. B16, 5426 (1977)

3.3 S.A. Lyon, G.C. Osborne D.L. Smith and T.C. McGill, Solid State Comm. 23, 425 (1977)

3.4 M. Jaros, F.A. Riddoch and Lu Da Lian, J. Phys C 16, L733 (1983)

3.5 K.R. Elliot, D.L. Smith and T.C. McGill, Solid State Comm. 27, 317 (1978)

3.6 S.M. Sze and J.C. Irvin, Solid State Elect. 11, 599 (1968)

3.7 R.M. Feenstra and T.C. McGill, Solid State Comm. 36, 1039 (1980)

3.8 W.E. Boyce and R.C. DiPrima, Elementary Differential Equations and Boundary Value Problems (Wiley, New York 1977) P.305

3.9 A. Yariv, Quantum Electronics (Wiley, New York 1975) P.437

3.10 R. Danelyus, V. Kabelka, A. Piskarskas and V. Smil'gyavichyus, Sov. Tech. Phys. Lett. 4, 308 (1978)

3.11 D.H. Auston in Ultrashort Light Pulses, edited by S.L. Shapiro (Springer, Berlin 1977) P.125

4.1 D.C. Reynolds, C.W. Litton and T.C. Collins, Phys. Rev. 156, 881 (1967)

4.2 C.H. Henry, K. Nassau and J.W. Shiever, Phys. Rev. B4, 2453 (1971)

4.3 D.C. Reynolds, C.W. Litton and T.C. Collins, Phys. Rev. 177, 1161 (1969)

4.4 C.H. Henry, K. Nassau and J.W. Shiever, Phys. Rev. B5, 456 (1972)

4.5 V.A. Abramov, S.A. Permogorov, B.S. Razbirin and A.I. Ekimov, Phys. Status Solidi 42, 627 (1970)

4.6 D.G. Thomas and J.J. Hopfield, Phys. Rev. 128, 2135 (1962)

4.7 C.H. Henry and K. Nassau, Phys. Rev. B1, 1628 (1970)

4.8 P. Wiesner and U. Heim, Phys. REv. B11, 3071 (1975)

4.9 M. Jorgensen and J.M. Hvam, Appl. Phys. Lett. 43, 460 (1983)

4.10 E.F. Gross, S.A. Permogorov, V.V. Travnikov and A.V. Selkin, Sov. Phys. Solid State 14, 1331 (1972)

4.11 D.C. Reynolds, Wright-Patterson Air Force Base

4.12 F. Askary and P.Y. Yu, Solid State Comm. 47, 241 (1983)

4.13 Y. Toyozawa, Prog. Theor. Phys. Suppl. 12, 111 (1959)

4.14 C. Hermann and P.Y. Yu, Phys. Rev. B21, 3675 (1980)

4.15 E.F. Gross, S.A. Permogorov, V.V. Travnikov and A.V. Selkin, Solid State Comm. 10, 1071 (1972)

4.16 F. Minami and K. Era, Solid State Comm. 53, 187 (1985)

4.17 Y. Masumoto and S. Shionoya, Phys. Rev. B30, 1076 (1984)

4.18 P.J. Dean, J.D. Cuthbert, D.G. Thomas and R.T. Lynch, Phys. Rev. Lett. 18, 122 (1967)

4.19 H. Malm and R. Haering, Can. J. Phys. 49, 2432 (1971)

4.20 C.H. Henry and K. Nassau, Phys. Rev. B2, 997 (1970)

4.21 J. Puls, F. Henneberger and J. Voigt, Phys. Status Solidi 119, 291 (1983)

4.22 J. Puls and J. Voigt, Phys. Status Solidi 94, 199 (1979

4.23 J. Puls, H. Redlin and J. Voigt, Phys. Status Solidi 107, K71 (1981)

4.24 K. Nassau, C.H. Henry and J.W. Schiever, Proceedings of the 10th International Conference on the Physics of Semiconductors, Cambridge Mass. USA 1970 (US AEC Press, Washington DC 1970) P.629

4.25 R.G. Wheeler and J.O. Dimmock, Phys. Rev. 125, 1805 (1962)

4.26 J. Voigt, Phys. Status Solidi 91, 189 (1979)

5.1 C.H. Henry and K. Nassau, Phys. Rev. B1, 1628 (1970).

5.2 E.I. Rashba and G.E. Gurgenishvili: Sov. Phys. Solid State 4 , 759 (1962).

5.3 E.I. Rashba, Sov. Phys. Semiconductors 8, 807 (1975).

5.4 G.D. Sanders and Yig-Chung Chang, Phys. Rev B28, 5887 (1983).

5.5 F. Minami and K. Era, Solid State Comm. 53, 187 (1985).

5.6 R.N. Bhargava, J. of Crystal Growth 59, 15 (1982).

5.7 P.J. Dean, B.J. Fitzpatrick and R.N. Bhargava, Phys. Rev. B26, 2016 (1982).

5.8 P.J. Dean and D.C. Herbert in Topics in Current Physics Vol. 14, Excitons, Ed. K. Cho (Springer Verlag Berlin 1979) P. 165.

5.9 W. Schmid and P.J. Dean, Phys. Stat. Solidi (b) 110, 591 (1982).

5.10 Neuberger in II-VI Semiconducting Compounds Data Tables (Hughes Aircraft Company, Culver City California 1969) P. 128.

5.11 B. Segall and D.T.F. Marple in Physics and Chemistry of II-VI Compounds Ed. M. Aven and J.S. Prener (North Holland, Amsterdam, 1967) P. 337.

6.1 H. Künzel and K. Ploog, Appl. Phys. Lett. 37, 416 (1980)

6.2 H. Künzel, J. Knecht, H. Jung, K. Wünstel and K. Ploog, Appl. A 28, 167 (1982)

6.3 K. Akimoto, M. Dohsen, M. Arai and N. Watanabe, Appl. Phys. Lett. 45, 922 (1984)

6.4 J.P. Salerno, E.S. Koteles, J.V. Gormley, B.J. Sowell, E.M. Brody, J.Y. Chi and R.P. Holmstrom, J. Vac. Sci. Technol. B3, 618 (1985)

6.5 B.J. Skromme, S.S. Bose, B. Lee, T.S. Low, T.R. Lepkowski, R.Y. DeJule, G.E. Stillman and J.C.M. Hwang, Appl. Phys. Lett. (to be published)

6.6 L. Eaves and D.P. Halliday, J. Phys. C 17, L705 (1984)

6.7 E.I. Rashba and G.E. Gurgenishvili, Sov. Phys. Solid State 4, 759 (1962)

6.8 D.C. Reynolds, K.K. Bajaj, C.W. Litton, E.B. Smith, P.W. Yu, W.T. Masselink, F. Fisher, and H. Morkoc, Solid State Commun. 52, 685 (1984)

6.9 E.W. Williams and H.B. Bebb in Semiconductors and Semimetals vol.8 ed. by R.K. Willardson and A.C. Beer (Academic Press, New York 1972) P. 339

6.10 E.S. Koteles, J.P. Salerno, W. Bloss, and E.M. Brody, Proceedings of the 17th International Conference on the Physics of Semiconductors Ed. J.D. Chadi and W.A. Harrison (Springer Verlag, New York 1985) P.1247

6.11 D.P. Halliday, L. Eaves and P. Dawson, J. Electronic Materials 14a, 1005 (1985)

6.12 M.S. Skolnick, T.D. Harris, C.W. Tu, T.M. Brennan and M.D. Sturge, Appl. Phys. Lett. 46, 427 (1985)

6.13 M.S. Skolnick, C.W. Tu and T.D. Harris, to be published

6.14 A.C. Beye and G. Neu, J. Appl. Phys. 58, 3549 (1985)

6.15 J.P. Contour, G. Neu, M. Leroux, C. Chaix and B. Levesque, J. Vac. Sci. Technol. B 1, 811 (1983)

6.16 D.J. Ashen, P.J. Dean, D.T.J. Hurle, J.B. Mullin, A.M. White and P.D. Greene, J. Phys. Chem. Solids 36, 1041 (1975)

7.1 J.J. Hopfield, Phys. Rev. 112, 1555 (1958)

7.2 Y. Toyozawa, Prog. Theor. Phys. Suppl. 12, 111 (1959)

7.3 V.V. Travnikov and V.V. Krivolapchuk, Sov. Phys. JETP 58, 1210 (1983)

7.4 F. Askary and P.Y. Yu, Solid State Comm. 47, 241 (1983)

7.5 E. Gross, S. Permogorov, V. Travnikov and A. Selkin, Solid State Comm. 10, 1071 (1972)

7.6 D.D. Sell, S.E. Stokowski R. Dingle and J. V. DiLorenzo, Phys. Rev. B7, 4568 (1973)

7.7 K. Aoki, Phys. Lett. 72A, 63 (1979)

7.8 W.C. Tait and R.L. Weiher, Phys. Rev. 178, 1404 (1969)

7.9 C. Weisbuch and R.G. Ulbrich, Phys. Rev. Lett. 39, 654 (1977)

7.10 C. Weisbuch and R.G. Ulbrich, J. of Lumin. 18/19, 27 (1979)

7.11 V.V. Travnikov and V.V. Krivolapchuk, Sov. Phys. JETP Lett. 37, 419 (1983)

7.12 R.G. Ulbrich and C. Weisbuch, in Festkorperprobleme (advances

in Solid State Physics), Volume XVIII, ed. J. Treusch (Vieweg, Braunschweig 1978) P.217

7.13 E.S. Koteles, J.P. Salerno, W. Bloss, and E.M. Brody, Proceedings of the 17th International Conference on the Physics of Semiconductors Ed. J.D. Chadi and W.A. Harrison (Springer Verlag, New York 1985) P.1247

7.14 E.S. Koteles, J. Lee, J.P. Salerno and M.O. Vassell, Phys. Rev. Lett. 55, 867 (1985)
J. Lee, E.S. Koteles, M.O. Vassell and J.P. Salerno, J. of Lumin. 34, 63 (1985)

7.15 W.L. Bloss, E.S. Koteles, E.M. Brody, B.J. Sowell, J.P. Salerno and J.V. Gormley, Solid State Commun. 54, 103 (1985)

7.16 L. Schultheis and C.W. Tu, Phys. Rev. B32, 6978 (1985)

7.17 J.J. Hopfield, Phys. Rev. 182, 945 (1969)

7.18 H. Sumi, J. Phys. Soc. Jap. 41,526 (1976)

7.19 F. Askary and P.Y. Yu, Phys. Rev. B31, 6643 (1985)

7.20 for review see J.L. Birman Ch.2 and E.L. Ivchenko Ch.4 in Excitons edited by E.I. Rashba and M.D. Sturge (North Holland Amsterdam 1982)

7.21 S.I. Pekar, Sov. Phys. JETP 6,785 (1958) and JETP 7,813 (1958)

7.22 J.D. Jackson, Classical Electrodynamics (Wiley, New York 1975) P.242

7.23 B. Fisher and H.J. Stolz, Appl. Phys. Lett. 40, 56 (1982)

A.1 H. Klann, J. Kuhl and D. von der Linde, Optics Commun. 38, 390 (1981)

A.2 M.S. Caceci and W.P. Cacheris, Byte Vol.9 No. 5, 340 (1984)

A.3 J.A. Nedler and R. Mead, Computer Journal 7, 308 (1965)